X-ray and neutron CT of biomedical samples: from image acquisition to quantification

Peruzzi, Niccoló

2021

Citation for published version (APA):
Peruzzi, N. (2021). *X-ray and neutron µCT of biomedical samples: from image acquisition to quantification*. Media-Tryck, Lund University, Sweden.

X-ray and neutron µCT of biomedical samples: from image acquisition to quantification

NICCOLÒ PERUZZI

MEDICAL RADIATION PHYSICS | FACULTY OF SCIENCE | LUND UNIVERSITY

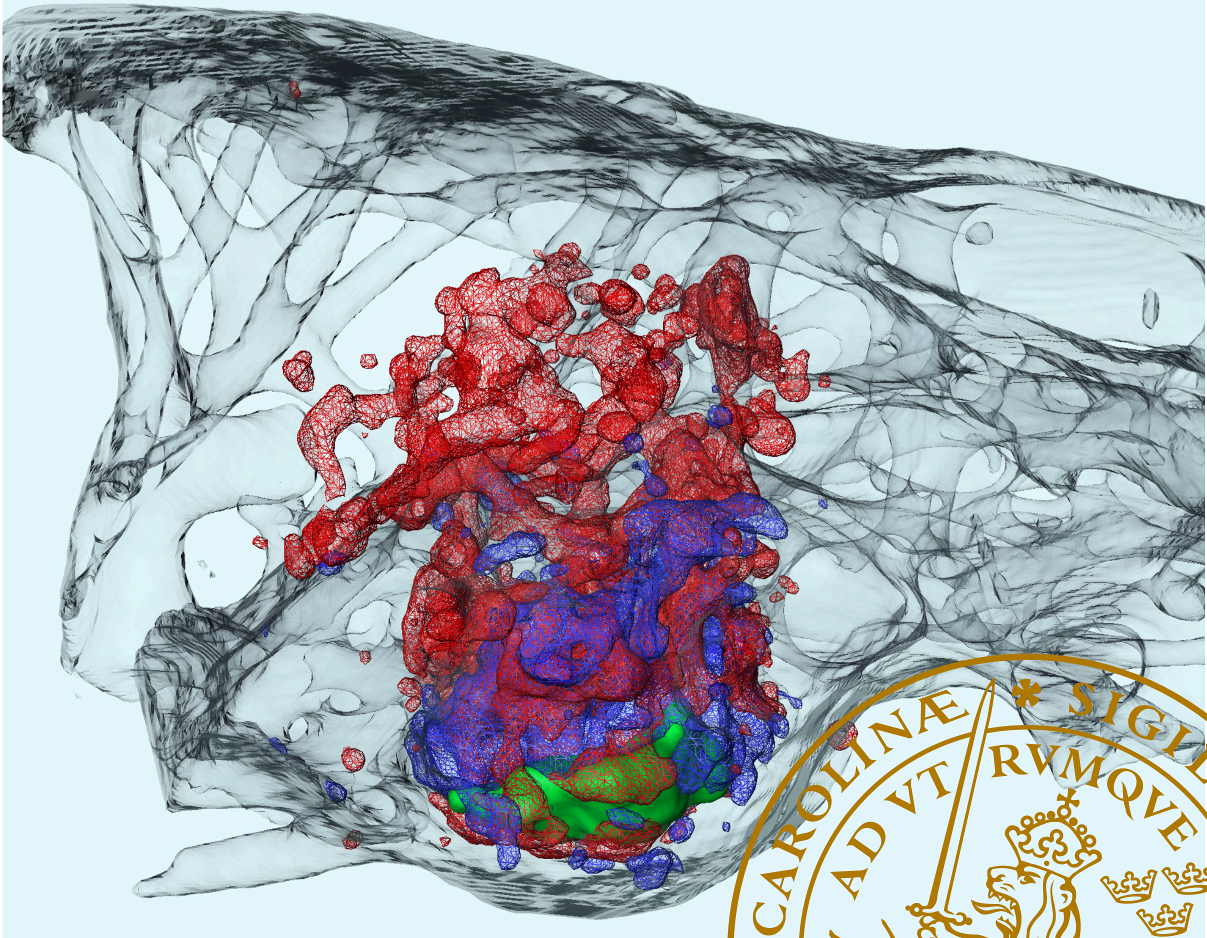

Printed by Media-Tryck, Lund 2021 NORDIC SWAN ECOLABEL 3041 0903

LUND UNIVERSITY

Faculty of Science
Clinical Sciences, Lund
Department of Medical Radiation Physics
ISBN 978-91-8039-092-7

9 789180 390927

X-ray and neutron μCT of biomedical samples: from image acquisition to quantification

X-ray and neutron µCT of biomedical samples: from image acquisition to quantification

Niccolò Peruzzi

DOCTORAL DISSERTATION

by due permission of the Faculty of Science, Lund University, Sweden.
To be defended at Föreläsningssalen, Plan 1, Alwallhuset, Barngatan 2, Skånes universitetssjukhus, Lund, Thursday the 16th of December 2021 at 9:00 am.

Faculty opponent
Prof. Dr. Bert Müller, Biomaterials Science Center (BMC), Department of Biomedical Engineering, University of Basel, Basel, Switzerland

Organization
LUND UNIVERSITY

Medical Radiation Physics Lund,
Department of Clinical Sciences

Author: Niccolò Peruzzi

Document name
DOCTORAL THESIS

Date of issue
2021-11-22

Sponsoring organization

Title and subtitle
X-ray and neutron µCT of biomedical samples: from image acquisition to quantification

Abstract

Even though the validity of x-ray computed tomography in the analysis of biomedical samples is nowadays undisputed, the more recent imaging techniques and more advanced instruments (such as synchrotrons) are still relatively unknown to many medical doctors that could benefit from them.

The doctoral work presented in this thesis joins a collective effort from the imaging community to demonstrate potential applications of advanced x-ray and neutron imaging methods to preclinical medical research, with the hope of contributing to reach a “critical mass” in the medical community and in the public opinion as well.

Two main lines of work are detailed, one focused on the *ex vivo* evaluation of corrosion processes of magnesium-based biodegradable implants for osteosynthesis, the other dedicated to the assessment of neuropathy in human gastroenteric dysmotility. The aimed endpoint was to develop pipelines, from image acquisition all the way to data quantification, that could be used by other research groups with similar questions and may inspire future interdisciplinary collaborations between medicine, natural science and engineering.

In the first line of work, we have attempted to employ synchrotron-radiation micro-computed tomography (µCT) coupled with *in situ* loading tests to assess the mechanical properties of the bone-implant interface (Paper I). We have revealed the crucial importance of the radiation dose deposited on the sample, and that the mechanical loading geometry should be accurately determined in the planning steps of the experiment. Moving away from the mechanical testing, we have also explored a novel three-dimensional analysis of the corrosion by-products of biodegradable implants by combining x-ray µCT, neutron µCT and x-ray fluorescence mapping (Papers IV and V).

The second line of work has assessed the potential of x-ray phase-contrast µCT and nano-resolution holotomography as ways to perform virtual histology of unstained peripheral and autonomic neural tissue. In full-thickness biopsies of the myenteric nervous system, qualitative and potentially quantitative differences have been shown between controls and patients affected by gastrointestinal dysmotility (Paper II). In unstained skin biopsies, the methods have failed to visualise peripheral nerves, but we could identify structural changes in the connective tissue of some patients when compared to controls and other patients (Paper III).

Key words: x-ray imaging, neutron imaging, µCT, synchrotron radiation, x-ray phase-contrast, nanoholotomography, x-ray elemental mapping, biomedical applications, virtual histology, biodegradable implants, Mg-alloys, enteric nervous system, peripheral neuropathy, gastroenteric dysmotility.

Classification system and/or index terms (if any)

Supplementary bibliographical information

Language: English

ISSN and key title

ISBN
978-91-8039-092-7 (print)
978-91-8039-091-0 (electronic)

Recipient’s notes

Number of pages
99

Price

Security classification

I, the undersigned, being the copyright owner of the abstract of the above-mentioned dissertation, hereby grant to all reference sources permission to publish and disseminate the abstract of the above-mentioned dissertation.

Signature Niccolò Peruzzi Date 2021-11-12

X-ray and neutron µCT of biomedical samples: from image acquisition to quantification

Niccolò Peruzzi

LUND
UNIVERSITY

A doctoral thesis at a university in Sweden takes either the form of a single, cohesive research study (monograph) or a summary of research papers (compilation thesis), which the doctoral student has written alone or together with one or several other author(s).

In the latter case, the thesis consists of two parts. An introductory text puts the research work into context and summarizes the main points of the papers. Then, the research publications themselves are reproduced, together with a description of the individual contributions of the authors. The research papers may either have been already published or are manuscripts at various stages of the publication process (in press, submitted, or in draft form).

Cover photo: different degradation by-products of a Mg-2Ag implant in bone identified with combined x-ray and neutron tomography (from Paper 5).

Faculty of Science
Department of Clinical Sciences Lund, Medical Radiation Physics

ISBN 978-91-8039-092-7 (print)
ISBN 978-91-8039-091-0 (electronic)

Printed in Sweden by Media-Tryck, Lund University
Lund 2021

Media-Tryck is a Nordic Swan Ecolabel certified provider of printed material. Read more about our environmental work at www.mediatryck.lu.se
MADE IN SWEDEN

To my parents,
who first taught me how to read and write

Table of Contents

Abstract

Even though the validity of x-ray computed tomography in the analysis of biomedical samples is nowadays undisputed, the more recent imaging techniques and more advanced instruments (such as synchrotrons) are still relatively unknown to many medical doctors that could benefit from them.

The doctoral work presented in this thesis joins a collective effort from the imaging community to demonstrate potential applications of advanced x-ray and neutron imaging methods to preclinical medical research, with the hope of contributing to reach a "critical mass" in the medical community and in the public opinion as well.

Two main lines of work are detailed, one focused on the *ex vivo* evaluation of corrosion processes of magnesium-based biodegradable implants for osteosynthesis, the other dedicated to the assessment of neuropathy in human gastroenteric dysmotility. The aimed endpoint was to develop pipelines, from image acquisition all the way to data quantification, that could be used by other research groups with similar questions and may inspire future interdisciplinary collaborations between medicine, natural science and engineering.

In the first line of work, we have attempted to employ synchrotron-radiation micro-computed tomography (μCT) coupled with *in situ* loading tests to assess the mechanical properties of the bone-implant interface (Paper I). We have revealed the crucial importance of the radiation dose deposited on the sample, and that the mechanical loading geometry should be accurately determined in the planning steps of the experiment. Moving away from the mechanical testing, we have also explored a novel three-dimensional analysis of the corrosion by-products of biodegradable implants by combining x-ray μCT, neutron μCT and x-ray elemental mapping (Papers IV and V).

The second line of work has assessed the potential of x-ray phase-contrast μCT and nano-resolution holotomography as ways to perform virtual histology of unstained peripheral and autonomic neural tissue. In full-thickness biopsies of the myenteric nervous system, qualitative and potentially quantitative differences have been shown between controls and patients affected by gastrointestinal dysmotility (Paper II). In unstained skin biopsies, the methods have failed to visualise peripheral nerves, but we could identify structural changes in the connective tissue of some patients when compared to controls and other patients (Paper III).

Popular science abstract

If you have ever had an injury, or problems with your teeth, your doctor has most probably asked to perform an x-ray radiographic scan on the interested area. This is an imaging technique which produces a picture of the internal structures of your body, by exploiting the ability of x-rays to penetrate through matter. If a radiography is not enough to reach a conclusion, maybe because the features are overlapping in the image, a more advanced x-ray imaging technique, called computed tomography (CT), can also be used. CT produces three-dimensional digital images of the inner structures of your body, which can then be checked from different angulations on a computer and used for a more accurate diagnosis by the doctors.

Aside from the use in the hospital, x-ray imaging is also employed in research, where new techniques are constantly being developed. Some of these methods are showing a lot of promise for biomedical research. For instance, x-ray microscopy techniques can allow to perform CT with very high magnification, which could help understanding the inner workings of organs or diseases down to the cellular level. X-ray elemental mapping can reveal the elemental composition of tissue, tracking for example metal contamination. Neutron CT is also being explored as an alternative to x-ray CT, since neutrons penetrate through matter in a different way compared to x-rays. Despite the potential, most of these techniques are still relatively unknown by medical doctors that could benefit from them, because they are seen as still too niche and complicated.

The work presented in this thesis joins a collective effort from the imaging community to demonstrate potential applications of advanced x-ray and neutron imaging methods to preclinical medical research, with the hope of contributing to reach a “critical mass” in the medical community and in the public opinion as well, after which the methods will be more broadly recognised and embraced.

Two main lines of work are here detailed. A first one has focused on the study of biodegradable metals for bone healing, that could potentially be used for repairing fractures or for dental applications. Biodegradable implants, which dissolve into biocompatible products over time, could avoid the need of second surgery for removal after the bone has healed. However, understanding the corrosion processes is important to regulate the degradation speed, so that the implant does not dissolve too early. In this doctoral work, advanced x-ray and neutron techniques have been used to improve

the current knowledge about some promising biodegradable materials, which could lead to the design of better ones in the future. A second line of work presented in this thesis has instead explored the potential of x-ray high-magnification microscopy in the study of gastrointestinal diseases. We have demonstrated that with these techniques we can observe differences in the enteric nervous system (the nervous system that regulates the functioning of the gastrointestinal tract) between healthy subjects and patients affected by gastrointestinal diseases. While this could be seen with optical microscopes as well, the advantage of x-ray techniques is that they can provide information in three-dimensions and in a faster way compared to traditional methods. In the future, this could open up the use of x-ray imaging for diagnostic purposes in severe cases of gastrointestinal disease.

Abstract divulgativo

Se avete mai avuto un infortunio o problemi ai denti, molto probabilmente il vostro medico avrà richiesto di eseguire una scansione radiografica a raggi X sull'area interessata. Questa è una tecnica cosiddetta di “imaging”, che produce un'immagine delle strutture interne del corpo sfruttando la capacità dei raggi X di penetrare attraverso i tessuti. Se una radiografia non è sufficiente per giungere ad una diagnosi accurata, magari perché i dettagli si sovrappongono nell'immagine, una tecnica di imaging a raggi X più avanzata, chiamata tomografia computerizzata (TC, o anche TAC), può aiutare a vederci più chiaro. La TC produce immagini digitali tridimensionali dell’anatomia interna, che possono essere controllate da diverse angolazioni tramite computer e utilizzate per una diagnosi più accurata dai medici.

Oltre all'uso in ospedale, l'imaging a raggi X viene impiegato anche nella ricerca, dove nuove tecniche vengono costantemente sviluppate. Alcuni di questi metodi si stanno dimostrando molto promettenti per la ricerca biomedica. Ad esempio, le tecniche di microscopia a raggi X possono consentire di eseguire TC con ingrandimenti molto elevati, che potrebbero aiutare a comprendere il funzionamento interno di organi o malattie al livello cellulare. La spettroscopia a raggi X può rivelare la composizione chimica dei tessuti, tracciando ad esempio metalli e contaminanti esterni. In alcuni casi, la tomografia a neutroni sta venendo anche esplorata come possibile alternativa alla TC a raggi X, poiché i neutroni penetrano attraverso la materia in modo diverso rispetto ai raggi X.

Nonostante il potenziale, molte di queste tecniche sono relativamente sconosciute ai ricercatori medici che potrebbero trarne beneficio, perché sono viste come ancora troppo di nicchia e complicate. Il lavoro presentato in questa tesi si inquadra in uno sforzo collettivo da parte della comunità di imaging per dimostrare potenziali applicazioni alla ricerca medica preclinica di metodi avanzati di imaging a raggi X e neutroni. La speranza sarebbe di contribuire a raggiungere una "massa critica" nella comunità medica e anche nell'opinione pubblica, in seguito alla quale i metodi qui presentati possano essere più ampiamente riconosciuti e abbracciati.

Due applicazioni in particolare vengono qui presentate. La prima si è incentrata sullo studio di metalli biodegradabili per l’osteosintesi, che potrebbero essere potenzialmente utilizzati per la riparazione di fratture o per applicazioni dentali. Impianti

biodegradabili, che si dissolvono nel tempo in prodotti biocompatibili, potrebbero evitare la necessità di un secondo intervento chirurgico a fini di rimozione dopo la guarigione dell'osso. Tuttavia, la comprensione dei processi di corrosione è fondamentale per regolarne la velocità, in modo che l'impianto non si dissolva troppo presto. In questo lavoro di dottorato sono state utilizzate tecniche avanzate di imaging a raggi X e neutroni per migliorare le attuali conoscenze riguardo alcuni promettenti materiali biodegradabili, il che potrebbe portare alla progettazione di materiali ancora migliori in futuro. Un secondo ambito di ricerca, presentato in questa tesi, ha invece esplorato le potenzialità della microscopia a raggi X ad alto ingrandimento nello studio delle malattie gastrointestinali. Abbiamo dimostrato che con queste tecniche è possibile osservare differenze nel sistema nervoso enterico (che regola il funzionamento del tratto gastrointestinale) tra soggetti sani e pazienti affetti da malattie gastrointestinali. Sebbene ciò possa essere stabilito anche con i microscopi ottici, il vantaggio delle tecniche a raggi X è che possono fornire informazioni in tre dimensioni e in modo più rapido rispetto ai metodi tradizionali. In futuro, questo potrebbe aprire l'uso dell'imaging a raggi X per scopi diagnostici nei casi di malattie gastrointestinali più gravi.

Original papers

This thesis is based on the following publications and manuscripts, referred in the text by their Roman numerals:

I. J. Moosmann, D.C.F. Wieland, B. Zeller-Plumhoff, S. Galli, D. Krüger, A. Ershov, S. Lautner, J. Sartori, M. Dean, S. Köhring, H. Burmester, T. Dose, **N. Peruzzi**, A. Wennerberg, R. Willumeit-Römer, F. Wilde, P. Heuser, J. Hammel, F. Beckmann, **A load frame for in situ tomography at PETRA III**, *SPIE2019*. (conference paper)

II. **N. Peruzzi**, B. Veress, L.B. Dahlin, T. Salditt, M. Andersson, M. Eckermann, J. Frohn, A.-L. Robisch, M. Bech, B. Ohlsson, **3D analysis of the myenteric plexus of the human bowel by X-ray phase-contrast tomography – a future method?**, *Scandinavian Journal of Gastroenterology* 55(10) (2020) 1261-1267. (original publication)

III. M. Eckermann, **N. Peruzzi**, J. Frohn, M. Bech, E. Englund, B. Veress, T. Salditt, L.B. Dahlin, B. Ohlsson, **3d phase-contrast nanotomography of unstained human skin biopsies may identify morphological differences in the dermis and epidermis between subjects**, *Skin Research and Technology* 27(3) (2021) 316-323. (original publication)

IV. **N. Peruzzi**, S. Galli, H. Helmholz, N. Kardjilov, D. Krüger, H. Markötter, J. Moosmann, D. Orlov, Z. Prgometh, R. Willumeit-Römer, A. Wennerberg, M. Bech. **Multimodal ex vivo methods reveal that Gd-rich corrosion byproducts remain at the implant site of biodegradable Mg-Gd screws**, *Acta Biomaterialia* (2021). In press. DOI: 10.1016/j.actbio.2021.09.047 (original publication)

V. **N. Peruzzi**, S. Galli, H. Helmholz, A. Tengattini, R. Woracek, A. Wennerberg, M. Bech. **Bimodal neutron and x-ray tomography provides new insights on degradation behavior of Mg-alloy implants**. *Manuscript.*

List of contributions

The following is a brief summary of my contributions to each presented paper and manuscript:

I. I participated in the acquisition of the reported tomographic scans of bone implants. I carried out the mechanical tests to assess radiation damage on murine bone, irradiating the samples, performing the three-point-bending test experiments and analysing the data to produce the final graphs. I assisted in simulating the dose delivered on the samples during synchrotron experiments. I contributed to writing the relevant parts of the paper.

II. I participated in the data acquisition experiments and in the tomographic image reconstruction. I helped the pathologist with the virtual histology of the acquired volumes. I segmented the structures of interest in the three-dimensional volumes and carried out the quantification analysis presented in the paper. I was the main author of the paper.

III. I participated in the data acquisition experiments and in the tomographic image reconstruction. I helped the pathologist with the virtual histology of the acquired volumes. I assisted in the writing of the paper.

IV. I was responsible for the design of the study. I participated in the acquisition of most of the data (except for the histological pictures and the x-ray fluorescence of organs). I performed most of the data analysis (with the exception of the x-ray fluorescence of organs) and developed the link between the different image modalities. I was the main author of the paper.

V. I was responsible for the design of the study. I acquired most of the data (except for the x-ray fluorescence maps). I performed all the data analysis. I was the main author of the manuscript.

Papers not included in this thesis

The author has contributed to the following publications, some of which are related to this Thesis but have not been included in it:

- D. Krüger, S. Galli, B. Zeller-Plumhoff, D.C.F. Wieland, **N. Peruzzi**, B. Wiese, P. Heuser, J. Moosmann, A. Wennerberg, R. Willumeit-Römer, **High-resolution *ex vivo* analysis of the degradation and osseointegration of Mg-xGd implant screws in 3D**, *Bioactive Materials*, in press (2021). (original publication)
- T. Dreier, **N. Peruzzi**, U. Lundström, M. Bech, **Improved resolution in x-ray tomography by super-resolution**, *Appl. Opt.* 60(20) (2021) 5783-5794. (original publication)
- C. Westöö, C. Norvik, **N. Peruzzi**, O.v.d. Have, G. Lovric, I. Jeremiasen, P.-K. Tran, R. Mokso, V.d.J. Perez, H. Brunnström, M. Bech, C. Galambos, K. Tran-Lundmark, **Distinct types of plexiform lesions identified by synchrotron-based phase-contrast micro-CT**, *American Journal of Physiology-Lung Cellular and Molecular Physiology* 321(1) (2021) L17-L28. (original publication)
- C. Norvik, C.K. Westöö, **N. Peruzzi**, G. Lovric, O.v.d. Have, R. Mokso, I. Jeremiasen, H. Brunnström, C. Galambos, M. Bech, K. Tran-Lundmark, **Synchrotron-based phase-contrast micro-CT as a tool for understanding pulmonary vascular pathobiology and the 3-D microanatomy of alveolar capillary dysplasia**, *American Journal of Physiology-Lung Cellular and Molecular Physiology* 318(1) (2020) L65-L75. (original publication)
- R. Willumeit-Römer, J. Moosmann, B. Zeller-Plumhoff, D.C.F. Wieland, D. Krüger, B. Wiese, A. Wennerberg, **N. Peruzzi**, S. Galli, F. Beckmann, J.U. Hammel, **Visualization of Implant Failure by Synchrotron Tomography**, Springer International Publishing, Cham, 2018, pp. 275-284. (conference paper)
- P. Johansson, S. Barkarmo, M. Hawthan, **N. Peruzzi**, P. Kjellin, A. Wennerberg, **Biomechanical, histological, and computed X-ray tomographic analyses of hydroxyapatite coated PEEK implants in an extended healing model in rabbit**, *Journal of Biomedical Materials Research Part A* 106(5) (2018) 1440-1447. (original publication)

- J. Moosmann, B. Zeller-Plumhoff, D.C.F. Wieland, S. Galli, D. Krüger, T. Dose, H. Burmester, F. Wilde, M. Bech, **N. Peruzzi**, B. Wiese, A. Hipp, F. Beckmann, J. Hammel, R. Willumeit-Römer, **Biodegradable magnesium-based implants in bone studied by synchrotron radiation microtomography**, *SPIE2017*. (conference paper)

Common abbreviations

2D	two-dimensional
3D	three-dimensional
CT	computed-tomography
µCT	micro-computed tomography
SRµCT	synchrotron-radiation-based micro-computed tomography
nHT	nano-holotomography
EDX	energy-dispersive x-ray spectroscopy
XRF	x-ray fluorescence
µXRF	micro-beam x-ray fluorescence
PEEK	polyetheretherketone
REE	rare-earth elements
ENS	enteric nervous system
IBS	irritable bowel syndrome

Abbreviations of significant chemical elements

Ag	Silver
C	Carbon
Ca	Calcium
Ce	Cerium
Fe	Iron

Gd	Gadolinium
H	Hydrogen
K	Potassium
Mg	Magnesium
Nd	Neodymium
P	Phosphorus
Pb	Lead
Y	Yttrium

Preface

Projects very rarely develop as linearly as planned, especially in Academia, and my doctoral experience has been no exception. This will inevitably be reflected in the structure of the doctoral thesis itself, which is invested with the onerous task of collecting quite disparate and scattered projects and finding a common structure under which to accommodate them all.

This preamble aims at briefly providing some context for the resulting structure of the thesis and clarifying the link between the different parts, which is very closely connected to the chronological development of my research.

When I first began my doctoral work, I was hired as part of the so-called SynchroLoad project, within the Röntgen-Ångström Cluster (a Swedish-German research collaboration). In its inception, the main scope of the project, which will be further detailed in Chapter 2, was to assess corrosion behaviour and mechanical properties of biodegradable bone-implants by means of synchrotron radiation micro-computed tomography and *in situ* mechanical testing. While the project was extremely valuable in immediately providing me with hands-on experience in the wide basics of x-ray tomography, essentially laying the foundations for what was to come later, a series of experimental setbacks in the beginning of the project prevented us from carrying out significant research for the first year/year and a half of my involvement. When we finally managed to acquire datasets on which I could perform further analyses, however, a crucial underestimation of the radiation damage induced on the samples came to light, compromising the validity of the mechanical testing. As detailed in Chapter 2, the radiation damage was found to be significant enough to put the mechanical testing side of the project on hold until lower dose scanning could be possible. The findings up to that point were grouped in Paper I of this thesis, and my involvement with the project was put on hiatus.

While I was waiting for experimental results from the SynchroLoad project, and obviously even more so after the developments leading to Paper I, I started getting involved in other projects related to the application of synchrotron radiation micro-computed tomography to biomedical samples. While several of these side-projects began as departmental duties, with the only aim of providing support to groups with a strictly medical background, my contribution was usually crucial to enable or speed up the data analysis and some of these partnerships developed into deeper collaborations. Chapter 3 introduces a selected project, focused on the analysis of neuropathy in human gastroenteric dysmotility, which has resulted in Paper II and Paper III. Other collaborations have targeted lung diseases, congenital heart diseases or the interaction between bone and several types of permanent implants; some of them have resulted in papers, which are listed among the ones not included in this thesis. A common characteristic of most of these studies was a focus on coupling high-resolution x-ray tomography with traditional histology, in an effort to promote the use of three-dimensional virtual histology as a powerful integration to the already very well affirmed two-dimensional histology and immunostaining techniques.

While virtual histology provides the obvious advantage of an additional spatial dimension, it cannot provide the functional separation between the different tissue components that can be achieved by tailored immunostaining. In some of these projects, we started exploring other types of imaging modalities that could obtain information outside the realm of histology; fluorescence-based imaging in particular, such as x-ray fluorescence, appeared promising to provide elemental composition of the tissue in exam. We also began looking at neutron tomography as a potential alternative to x-ray tomography when dealing with highly x-ray absorbing metal implants. My interest in multimodal methods deepened, and I wondered whether we could explore some of these techniques for the SynchroLoad samples as well.

The occasion presented itself when, during a neutron imaging course, I was asked to draft a mock-up beamtime proposal and I picked the SynchroLoad samples as my case of choice; after encouragement about feasibility by the course organizers, I submitted the proposal to a real facility and managed to obtain beamtime. In very practical and simple terms, x-rays are usually highly attenuated by metals and poorly attenuated by biological tissue; neutrons present an opposite behaviour, traversing metals with low effort (aside from a few exceptions, as will be shown) and being heavily attenuated by biological material. Intuitively, a combination of the two techniques would appear as a perfect tool to study biodegradable metals, such as the ones in the SynchroLoad project. Chapter 4 provides more details about this line of work, which has so far culminated in Paper IV and Paper V and appears very promising for the future.

Introduction

Imaging can be defined as the process of making a visual representation of an object by using a probing radiation and a detecting and capturing system. As a natural and immediate example, one could think about human vision, in which electromagnetic radiation in the visible spectrum is reflected or refracted by an object, passes through the lens of the eye and is detected by the retina, to be then processed and stored by the brain.

Historically, imaging has been limited to visible light for most of human history, with the progressive discovery of methods that could project images, such as the "camera obscura", optical systems that would push the boundaries of what could be observed, like telescopes and microscopes, and finally ways to create durable images, with the invention of photography.

A paradigm shift happened in November 1895, with Röntgen's first discovery of a "new" type of radiation, which he called x-rays (Röntgen, 1895, Röntgen, 1896). This mysterious radiation had the ability to pass through many materials that absorb visible light, as Röntgen himself demonstrated by taking an x-ray picture of his wife's hand on a photographic plate (Figure I-A).

Just a few months after the discovery, scientists and physicians started to explore the clinical potential of what is today known as radiography (Frost, 1896). The new technique allowed to assess skeletal trauma and identify foreign objects in the body in ways that had not previously been possible. As such, many initial applications of radiography were in military medicine: a particularly famous example that comes to mind is Marie Curie and her *petites Curies*, small radiography units employed on the battlefield during World War I (Figure I-B). Outside of the military, the mass production of x-ray tubes helped to spread the technique all over the world in a very short time. X-ray radiography was used, and still is today, in orthopaedics, surgery planning, detection of lung lesions (such as tuberculosis), oncology.

The main limit of radiography is that, since it is acquired by having x-rays pass through the object in exam, it cannot distinguish features which are overlapping in the projection plane. A basic solution to this issue is to perform radiographies while varying the angle of the object with respect to source and detector, in what is called focal plane tomography.

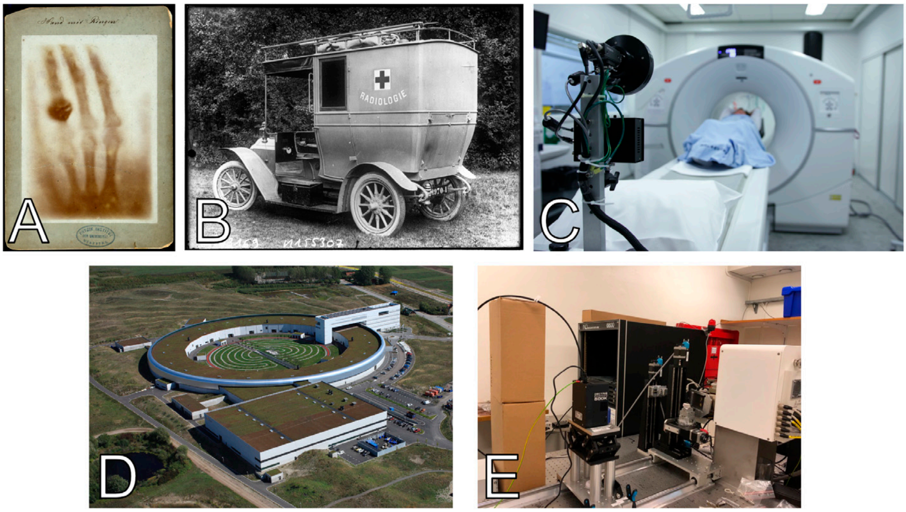

Figure I: Examples of evolution of x-ray imaging.
A – The bones of a hand with a ring on one finger, viewed through x-ray. Photoprint from radiograph by W.K. Röntgen, 1895. Wellcome Collection (CC BY-NC 4.0). **B –** Radiological car Massiot; mobile radiological unit, in service of the French Army and the Red Cross. November 1914. Bibliothèque nationale de France, département Estampes et photographie (Etalab open licence). **C –** Clinical CT scanner. Image by user Bokskapet from Pixabay (Pixabay licence). **D –** Aerial photo of the synchrotron MAX IV in Lund, Sweden. August 2018. Photo by Perry Nordeng. Lund University Image and Media bank. **E –** A laboratory setup for x-ray µCT. Photo courtesy of Till Dreier.

First examples of this tomographic concept are traced back to 1914 (Webb, 1990, Webb, 1995), and the technique was independently developed in the 1920s and 1930s by several scientists (Webb, 1990, Webb, 1995), affirming even more the use of x-rays in the medical field.

The fundamental next step in medical imaging came with the advent of digitization, following the invention of digital image sensors in the 1960s, which enabled the use of computers in order to easily perform complex mathematical operations on the acquired images. This is ultimately what has led to the introduction, by Hounsfield and Cormack in 1972, of x-ray computed tomography (CT) (Hounsfield, 1973), a technique which allows to obtain three-dimensional (3D) digital images of an object after acquiring digital radiographies at different angles. X-ray CT is nowadays one of the most used techniques in clinical diagnostic (Figure I-C) and is constantly being improved by advancements in hardware (new sources and detectors) and methods (helicoidal tomography and multi-slice CT come to mind). Aside from x-rays, other types of probing radiation have also been added to the roster of medical imaging, such as radio waves (in magnetic resonance imaging), gamma rays (in single-photon emission CT and positron emission tomography) or ultrasounds.

Beside the applications to the clinic, however, imaging has seen steady progress in scientific research as well, where the boundaries have been pushed even further, without the obvious constraints imposed by approval for clinical use. In the field of x-ray imaging, the introduction of synchrotron light sources from the 1970s onward has provided x-ray light with unparalleled brilliance (a parameter which describes both brightness and angular spread of the beam), coherence, and energy tunability. This has paved the way to constant improvements in x-ray microscopy (Kirz and Jacobsen, 2009), to the point that several imaging techniques available today are pushing the spatial resolution to the diffraction limit of a few nanometres (Pfeiffer, 2018). Different ways in which x-rays interact with matter have also been exploited, providing alternative contrast mechanisms to the traditional x-ray attenuation, such as in x-ray phase-contrast imaging (Paganin, 2006). While many of these techniques were originally limited to synchrotron facilities (Figure I-D), of relatively restricted access, the constant improvement of laboratory x-ray sources has also gradually introduced them to laboratory setups as well (Wilkins et al., 2014, Tuohimaa et al., 2007, Zanette et al., 2014) (Figure I-E).

Several of these advanced x-ray imaging techniques have shown great potential for biomedical research. For example, x-ray phase-contrast imaging has opened the use of x-rays to study soft tissues, commonly regarded as too weakly attenuating for the use of standard x-ray CT. Potential applications have been shown both in preclinical research (Thomlinson et al., 2005, Pfeiffer et al., 2013) and even in clinical diagnostic (Bravin et al., 2012), especially applied to mammography (Stampanoni et al., 2011, Zhao et al., 2012). Laboratory-based systems for micro-resolution computed tomography (µCT) have been used for the study of small animal models, for example in cancer research (Paulus et al., 2000) or in the evaluation of dental implants (Vandeweghe et al., 2013). When combined with phase-contrast, high-resolution x-ray imaging has the potential to evaluate the inner workings of organs or diseases down to the cellular level, in what could possibly rival or at least complement traditional histological analyses (Khimchenko et al., 2018, Töpperwien et al., 2018, Albers et al., 2018). Aside from x-ray imaging, other kinds of imaging, historically developed for material science, are also gaining increasing appeal for biomedical studies. X-ray elemental mapping for example can reveal the elemental composition of tissue, useful to study calcifications or the distribution of metals, either naturally occurring or coming from external contamination (Pushie et al., 2014, Scimeca et al., 2018). Neutron CT is also being explored as an alternative to x-ray CT, since neutrons penetrate through matter in a different way compared to x-rays, with possible applications to the study of metal implants in bone (Isaksson et al., 2017).

Despite their great potential for the study of biomedical samples, most of these techniques are however still relatively obscure to the medical community as a whole. The most significant limiting factor in this sense is that big facilities, and the data analysis required to deal with the datasets that they produce, are far outside the comfort zone of professionals who very seldomly are trained in radiation physics, advanced math and coding. Even though synchrotron facilities are starting to provide at the very least some data reconstruction, data analysis is typically left to the user. The same is true for experimental laboratory setups, which are normally not user friendly at all and require collaborations between the physicists who design, build and operate the instrument and the medical doctors who provide the samples. All of this limits the access to these instruments to only a restricted number of medical research groups who are already in collaborations with physics groups or have within them somebody already familiar and trained in tomographic techniques. Others, who could draw great benefit from advanced x-ray imaging techniques in their research, are usually unaware of the developments of x-ray tomography outside of clinical CT machines or, even if aware, will probably have a hard time to access it. In order to encourage a broader medical interest into these techniques, it is important to increase the number of potential applications, in the hope to reach a "critical mass" in the medical community and in the public opinion as well.

The main focus of the present doctoral work has been to try and bridge this gap between "instruments and methods developers" and "samples and questions providers" by joining collaborations with different medical groups in the Malmö and Lund area, in order to show them the potential of some of these methods for preclinical studies and aid them in the process. The aimed endpoint was to develop pipelines, from image acquisition all the way to data quantification, that could be used by every other research group with similar questions.

Aside from state-of-the-art x-ray imaging, which has been applied to the study of biodegradable implants for bone (Papers I, IV and V) and to the assessment of neuropathy in gastrointestinal dysmotility (Papers II and III), a significant part of this thesis work was also dedicated to exploring the potential of alternative imaging techniques, i.e. neutron micro-computed tomography and x-ray elemental mapping, as complementary methods to x-ray tomography (Papers IV and V).

The outline of the thesis is the following: Chapter 1 will provide a brief overview of the techniques encountered during this doctoral work, from image production to quantification; Chapters 2-4 will introduce the included papers (I to V), providing their medical background, which is integral to their novelty, and more specific technical details; Chapter 5 will add some concluding remarks and an outlook to future possible developments.

1 Theory

"Either this is madness or it is Hell."
"It is neither," calmly replied the voice of the Sphere, "it is Knowledge;
it is Three Dimensions: open your eye once again and try to look steadily."
— Edwin A. Abbott, Flatland: A Romance of Many Dimensions

This Chapter will quickly describe the techniques used in the present work, with no pretence of exhaustivity. A first part will be dedicated to the acquisition of x-ray and neutron CT images, a second one to CT image analysis. X-ray elemental mapping techniques, which have been used in Papers IV and V, differ in several ways from the other two methods and as such will be described in a separate section at the end of the Chapter.

1.1 Tomographic image acquisition

This part will go through all the steps that are necessary to produce an x-ray or neutron tomography image of an object.

1.1.1 X-ray and neutron production and detection

In order to acquire images with any kind of probe, the obvious first step is having the means of producing and detecting it.

X-ray generation is commonly achieved from high-energy electrons. A first method is to have the electrons impact on a material, which generates x-ray emission from both the electrons and the material itself. This is at the basis of the so-called electron-impact x-ray sources. A second method is to have the electrons accelerate in a magnetic field, which causes the electrons themselves to emit x-rays. This is what is done at synchrotron radiation facilities.

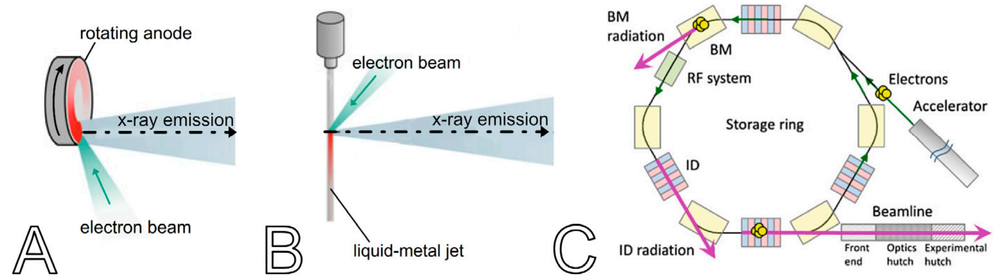

Figure 1-1: Examples of x-ray sources used in this work.
A – a rotating anode source, in which the anode is a solid metal disk that continuosly rotates for better heat dissipation. **B –** a liquid-metal jet source, in which the anode is continuosly regenerated and is already in a molten state, enabling the use of higher electron-beam power and reducing the x-ray spot size. **C –** a synchrotron light source; after being accelerated to relativistic speeds, electrons are kept in a circular closed orbit by bending magnets (BM), which deflect them, and radiofrequency systems (RF system) which restore their energy to keep it constant. Synchrotron radiation is produced when the electrons pass through the BM, or through special insertion devices (ID). The x-rays are then sent to a beamline, where they are shaped for the need of the experimental station by a series of optical systems. Figures A and B adapted from (Salditt and Töpperwien, 2020) (open access CC BY 4.0), Figure C reprinted from (Uruga, 2017) by permission from Springer Nature © 2017.

Electron-impact x-ray sources were historically the first x-ray sources to be developed (Röntgen’s cathode-ray tube was a simple example of an electron-impact source). In them, electrons produced by a heated cathode are accelerated by a high voltage until they hit an anode. The abrupt deceleration of the electrons will produce x-ray bremsstrahlung emission. Furthermore, some of the electrons will also ionize atoms in the anode, with emission of characteristic x-rays. Electron-impact sources have come a long way since Röntgen’s first experiments (Ammann and Kutschera, 1997), with a series of improvements mainly aimed at reducing the emission spot size (which today can be as low as a few microns) and increasing the power (Figure 1-1A and 1-1B). Most of them are small enough to fit on a tabletop, inside of medical devices or in special cases even in handheld instruments.

In synchrotron radiation facilities (Figure 1-1C), electrons are kept circulating at constant relativistic speed in a storage ring. In order to keep the electrons in a closed orbit, bending magnets are placed at certain places along the ring. When they pass in a bending magnet, electrons will be accelerated by the magnetic field and produce x-rays; since they are traveling at relativistic speeds, the emission will be mostly in the forward direction, tangential to the ring. Specialized insertion devices such as wigglers or undulators can also be placed in the straight sections of the storage ring. In these devices an alternating magnetic field forces the electrons to follow oscillating paths rather than moving in a straight line. The ending results is again emission of x-rays, with different properties when compared the ones emitted by a bending magnet. In correspondence to the bending magnets or the insertion devices, the produced x-ray radiation is “captured” by a beamline, a series of elements that will condition the x-ray beam and deliver it to an experimental end station, where it will be used for different scientific experiments. Compared to electron-impact sources, synchrotrons can deliver x-rays with much higher brilliance, coherence, tunable monochromaticity and tunable polarization. Synchrotron radiation sources are exhaustively described in many textbooks, see e.g. Willmott "An Introduction to Synchrotron Radiation: Techniques and Applications" (Willmott, 2011).

Neutron generation is significantly harder than x-ray generation. In this work, the only sources of neutrons that have been used were nuclear fission research reactors. They work in the same way as nuclear power plants, except for the fact that they are specialized in extracting neutrons from the chain reaction, rather than focusing on heat production. When a slow-moving neutron collides with the nucleus of a heavy element (such as uranium), the neutron is absorbed and the nucleus breaks apart. This splitting results in several fission products including, among others, neutrons, lighter atomic nuclei, radioactivity and heat. The latter is dissipated by cooling. A portion of the neutrons is needed to keep the chain reaction going. The remaining portion, however, is opportunely slowed and then guided through beamlines to the experimental stations.

X-rays and neutrons are both not trivial to detect. When performing imaging, the most common approach is to convert them to visible light by using scintillators and then detect the visible light with a camera, i.e. a detector with two-dimensional spatial resolution (Gruner et al., 2002, Martin and Koch, 2006). An ideal detector should have high resolution, high efficiency and low noise. Parameters like the field of view and the read-out time are also important for imaging. Especially in synchrotron and nuclear sources, typically an optical microscope is placed between scintillator and camera, with the dual purpose of protecting the camera from the direct radiation beam and providing geometric magnification of the image (Koch et al., 1998). In other cases, the scintillator is coupled to the camera by using micro-channel plates or is deposited directly on it. In the case of x-rays, direct detection is also possible using semiconductor cameras (Overdick et al., 2009).

Independently on how the detection has taken place, the acquired image is then converted into a digital file, that is stored in a computer. Each pixel of the image is given a value, called gray-level, which is proportional to the intensity registered by the corresponding pixel of the camera.

1.1.2 X-ray full-field imaging

The simplest setup for x-ray imaging consists in a source that illuminates the object homogeneously and a panel detector that registers the transmitted radiation behind the object.

By thinking in wave-theory terms, the x-ray wave that passes through the material will have its intensity attenuated by it (Figure 1.2). Another possible effect on the wave is a shift in its phase (Figure 1.2), determined by coherent scattering events. Both of these effects and the contrast that they produce can be exploited in x-ray imaging (Als-Nielsen and McMorrow, 2011).

Attenuation-contrast

The conventional way of performing x-ray imaging is based on attenuation variations. If a radiation with initial intensity I_0 passes through an object with thickness $T(x,y)$, Beer-Lambert's law gives the intensity I after the object as:

$$I(x,y) = I_0 e^{-\mu T(x,y)} \tag{1}$$

Where μ, the linear attenuation coefficient, represents the contribution of absorption and scattering processes in dampening the x-ray beam. μ depends on the material's atomic number and density, as well as on the energy of the incoming radiation. A material thickness of μ^{-1} will reduce the intensity of a factor e^{-1}. An object which is too thin will produce low variations in contrast, an object that is too thick will risk attenuating too much the signal.

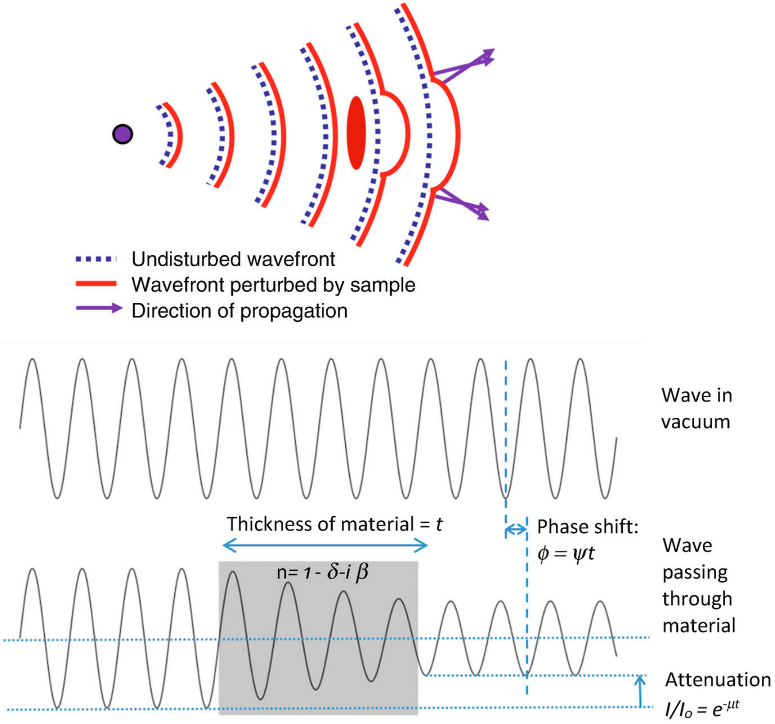

Figure 1-2: Effects of a sample on the x-ray beam.
Top – A spherical wave passing through a sample results in a distortion of the wavefront and a change in its direction of propagation, which can lead to interference (the size of the distortion is greatly exaggerated). **Bottom –** comparison between a wave in vacuum and a wave that passes through a medium of refracting index n, experiencing an attenuation in its intensity and a phase shift. Figure reprinted from (Mayo and Endrizzi, 2019) by permission from Springer Nature © 2019.

Beer Lambert’s law presented in the previous equation is valid for monochromatic x-rays and a homogeneous object. In case of a polychromatic source and an object composed of different materials or densities, Beer Lambert’s law needs to be extended to a path integral along the object’s thickness, as in:

$$I(x, y) = \int I_0(E) e^{-\int \mu(x,y,z,E) dz} dE \tag{2}$$

In the projections acquired on the 2-dimensional detector, contrast will be given by lateral variations (i.e. along x and y) of composition and density in the object.

Phase-contrast

As already mentioned, radiation interacting with a material will also have its phase shifted. For hard x-rays and low atomic number materials, like biological tissue, the differences in phase shift are reportedly larger than the differences in attenuation (Schulz et al., 2010). Using phase instead of attenuation provides then the possibility of significantly increasing the contrast (or alternatively decreasing the radiation dose while keeping a comparable contrast). The main issue however comes from the fact that x-ray detectors measure intensity, which is independent of phase. The phase variations introduced by the object need to be somehow converted to intensity variations in order to be extracted. Various techniques can be used for this purpose, all of which are based on the observation of interference patterns between diffracted and non-diffracted waves. Most of them can be classified in one of three categories: free-space propagation, interferometric based techniques or analyser systems.

In this work, only propagation-based imaging in the near-field (Salditt et al., 2017) has been used. It is the most straightforward approach to phase-contrast, since it does not involve any equipment other than source and detector. If the detector is really close to the sample (contact regime), an attenuation image is obtained. When the detector distance is increased, interference between the scattered and transmitted x-rays occurs (Figure 1-3). For small distances (direct contrast regime), interference fringes start to develop along the contour of the sample’s features, producing edge-enhanced images of the sample. As the distance increases, while still in the near-field, the diffraction patterns lose resemblance with the object and lead to holographic images (holographic regime). In the direct contrast regime, the fringes produce edge-enhancement of the sample, which is often already useful by itself for qualitative assessments. A more complete and quantitative evaluation requires to retrieve the phase from the diffraction patterns (Figure 1-4). A wide range of methods exist for this purpose, for example those based on the transport-of-intensity equation (Paganin et al., 2002, De Witte et al., 2009). Propagation-based phase-contrast in the direct contrast regime has been used in this doctoral work in Papers II and III, as well as in measurements which have led to other papers not presented in this thesis (Norvik et al., 2020, Westoo et al., 2021). In Papers II and III, a more complicated method known as holotomography (Cloetens et al., 1999), in which images recorded at several distances in the holographic regime are combined to quantitatively retrieve the phase shift, has also been employed. In general, every instrument in which phase-contrast imaging is routinely performed will have its own implementation of a phase-retrieval pipeline. Given the high requirements of spatial coherence, propagation-based phase-contrast imaging had initially been a prerogative of synchrotron radiation sources. Recent improvements to electron-impact x-ray sources and high-resolution detectors are leading to successful use of the technique also in laboratory setups (Larsson et al., 2013).

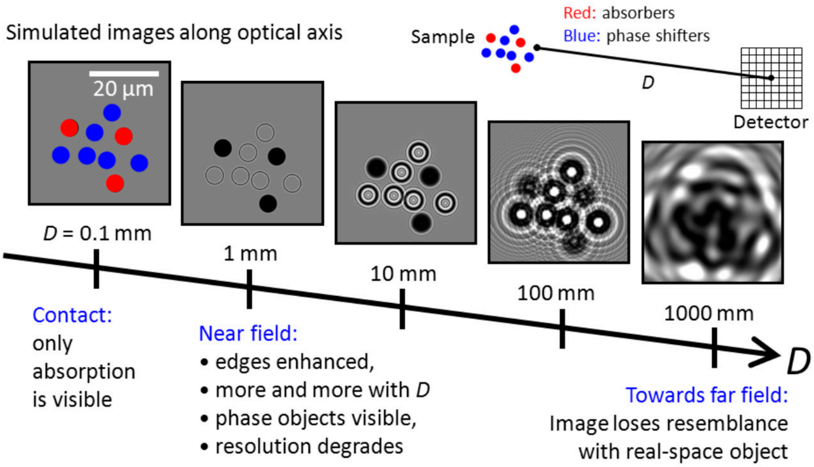

Figure 1-3: Propagation-based phase-contrast.
Image formation behind an object composed of absorbing structures (red) and non-absorbing phase shifters (blue), as a result of X-ray free space propagation. The simulation was performed with the XWFP propagation code (Weitkamp, 2004), using a Fresnel propagation kernel in paraxial approximation. Image: T. Weitkamp (CC BY 3.0 DE).

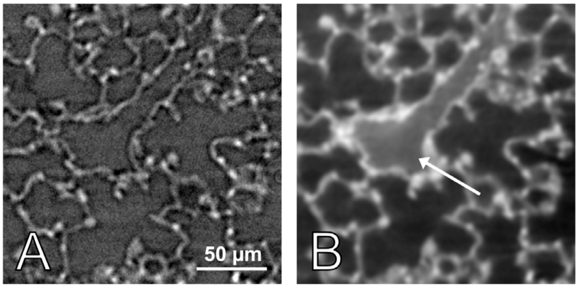

Figure 1-4: Importance of phase-retrieval.
Crop of tomographic scan of mouse lung tissue acquired in the near field regime. **A –** Without phase-retrieval, edge enhancement is noticeable on the alveolar walls, visible as small filaments. **B –** Phase-retrieval (Paganin et al., 2002) converts the edge effects into contrast information; the image appears blurrier, but contrast differences between alveolae (dark areas), alveolar walls (white filaments) and small capillaries filled with dye (arrow) are more apparent. Data unpublished.

1.1.3 Computed Tomography

What has been described so far allows to obtain radiographies of the object, i.e. two-dimensional (2D) projections of the unknown object 3D properties onto the detector's plane. The main limit of radiography is that it cannot distinguish superimposing features of the object. A work-around to this is given by computed tomography, which allows to obtain volumetric information about the object by acquiring 2D projections at different angles and then applying mathematical reconstruction methods. Similar to phase-retrieval, development of tomographic reconstruction algorithms is a very large field of research, which is also strictly connected to the continuous development of more powerful and faster computers to handle the more computationally expensive algorithms. A good introductory book is "Principles of computerized tomographic imaging" by A. Kak and M. Slaney (Kak and Slaney, 2011).

The mathematical foundation of computed tomography was laid down already in 1917 by J. Radon. It is based on the Fourier slice theorem, which establishes a relation between a one-dimensional projection and the corresponding two-dimensional axial section through an object. Per the theorem, the Fourier transform of a projection at an angle θ will coincide with the central slice through the 2D Fourier transform of the axial section at the same angle. The Fourier slice theorem is illustrated in Figure 1-5. By acquiring projections at different angles, the 2D Fourier transform of the section can be sampled.

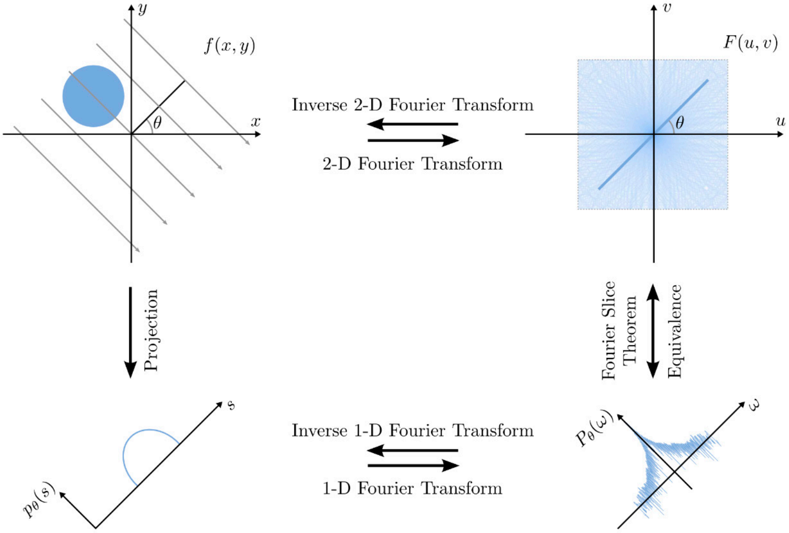

Figure 1-5: The Fourier slice theorem.
The theorem establishes an equivalence between the Fourier transform $P_\theta(\omega)$ of the projection $p_\theta(s)$ and a line in the Fourier transform F(u,v) of f(x,y) which runs through the origin and forms the angle θ with the u-axis. Figure reprinted from (Maier et al., 2018) (CC BY 4.0).

Once the object has been sampled, the most common reconstruction technique is the Filtered Back-Projection (FBP). It reconstructs the object in real space by performing an inverse transform from the sampling in Fourier space. If one looks at Figure 1-5, two considerations must be made about this method: the sampling in Fourier space is denser at lower frequencies and it is on a polar grid, rather than a Cartesian grid. Both of these things need to be addressed at some point of the process. Typically, the sampling density is corrected by applying filters in Fourier space (hence why the name “Filtered Back-Projection”). The polar grid is instead converted to a Cartesian grid with interpolation. Most commonly the interpolation is performed in the real domain because that introduces less noise, however methods have been developed to perform it in Fourier space, with a significant gain in computational speed at the cost of lower reconstruction quality (Marone and Stampanoni, 2012).

The Fourier slice theorem and the FBP algorithm are valid only for parallel beam geometries. However, extensions of the algorithm have been made for other types of imaging geometries. In particular, for cone-beam geometry (typical of electron-impact sources), a well-known one is the Feldkamp-David-Kress (FDK) algorithm (Feldkamp et al., 1984).

A different kind of algorithms is given by the iterative ones, which approach the correct solution using multiple forward projection iteration steps. They typically begin with an initial image guess, compute projections, compare the original projection data with the newly obtained ones and update the image based upon the difference between the calculated and the actual projections. Iterative algorithms can usually achieve better results than back-projection ones, but their main downside is that they are computationally very expensive.

Just like in phase-retrieval, instruments in which tomography is commonly performed will have their own implementations of reconstruction algorithms, tailored for the geometry and the specifics of their particular setup. In many cases, licensed reconstruction software can also be used. Lastly, if flexible tomographic reconstructions are needed, open source toolboxes are available, such as TomoPy (Gursoy et al., 2014), ODL (Adler et al., 2017), the ASTRA toolbox (van Aarle et al., 2015, van Aarle et al., 2016) and TIGRE (Biguri et al., 2016). They are usually based on Python or MATLAB and help to design custom reconstruction algorithms and geometries by providing staple “building block” functions. As an example, the reconstruction pipelines used in the µCT scans of Paper I, Paper II and Paper III are all based on the ASTRA toolbox for their tomographic reconstruction step.

1.1.4 Neutron imaging

Most of the techniques described so far for x-rays can be directly translated to neutron imaging, in particular attenuation-based tomography, which is the only neutron technique that has been used in this thesis work. A good introduction to neutron imaging methods is given, for example, in (Banhart, 2008).

The main difference between x-rays and neutrons lies in how they interact with matter (Figure 1-6). The interaction of x-rays takes place in the electron shell of the atoms (mainly through photoelectric effect and Compton scattering). Therefore, it is understandable that atoms with fewer electrons in their shell interact only weakly with x-rays when compared to heavy elements. Neutrons, in particular the thermal and cold ones commonly used for imaging purposes (with energies around 26 meV and 2 meV respectively), interact with the atomic nuclei, completely ignoring the electrons in the shell.

As a consequence, the attenuation coefficients are radically different between the two types of particle. While x-ray attenuation coefficients usually increase as a function of the atomic number Z of the material, neutron attenuation coefficients have no underlying systematic law. In particular, neutrons are highly attenuated by hydrogen (H), typically present in plastics and biological tissue, while they easily penetrate most metals, which would normally heavily attenuate x-rays. A further peculiarity of neutrons, related to their interaction with atomic nuclei, is that they are sensitive to isotopes, showing for example different attenuation for ^{1}H and ^{2}H. All of this can make neutron imaging better suited in many instances than x-ray imaging and the two techniques are normally considered as complementary one to the other (Figure 1-7).

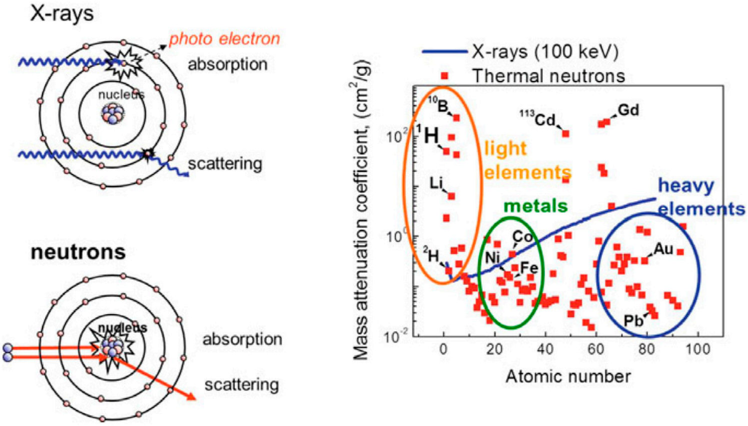

Figure 1-6: Comparison of x-ray and neutron attenuation.
While x-rays interact with atomic electrons, neutrons interact with atomic nuclei. As a result, neutron attenuation coefficients do not increase proportionally with the atomic number like x-ray attenuation coefficients. In particular, neutrons are very sensitive to some light elements (such as hydrogen), where x-rays do not provide good contrast. On the other hand, neutrons easily penetrate heavy elements that would normally attenuate x-rays a lot (Pb, Fe). Figure reprinted from (Kardjilov et al., 2017) by permission from Springer Nature © 2017.

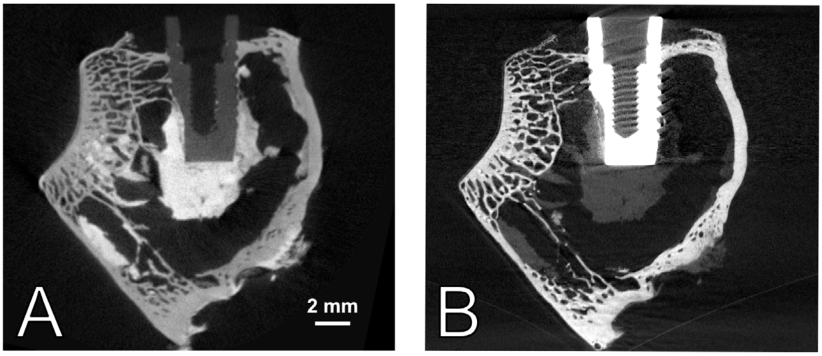

Figure 1-7: Complementarity of x-ray and neutron imaging.
Comparison between neutron µCT (**A**) and x-ray µCT (**B**) of a titanium screw implanted in rabbit bone (dried sample). While in B the metal screw is highly attenuating and introduces several beam-hardening artefacts, in A the implant is less attenuating than biological material. In particular, the soft bone marrow shows high contrast with neutrons. Scanning parameters were set in order to have approx. the same voxel size (13 µm). Total scan time for neutron µCT (CONRAD-2 beamline of BER-II reactor): 10 h; total scan time for the x-ray µCT (laboratory setup): 1 h. Data unpublished.

1.2 Tomographic image analysis

After acquiring the volumetric datasets, a series of operations has to be performed in order to extract useful information from them. The field of image analysis is extremely varied and complex. This section of the theory aims at giving a quick overview of just the different concepts and techniques that have been encountered in this work.

1.2.1 Visualization

The first fundamental step is obviously to visualize the data. Many image visualization programs are available for that purpose, both licensed (such as Amira, by Thermo Fisher Scientific) and free (like FIJI (Schneider et al., 2012, Schindelin et al., 2012), 3D Slicer (Kikinis et al., 2014), ITK-Snap (Yushkevich et al., 2006) or tomviz (Levin et al., 2018)). Most of them also offer image processing capabilities. Functions to visualize image data are even available in many programming languages and environments, like Python or MATLAB.

Since the acquired data are 3D volumes, typically they are visualized by slicing them and going through each slice (that is basically the idea behind the concept of computed tomography, after all). All the mentioned visualization programs allow to at least slice the volume in the three orthogonal directions, most of them also allow arbitrary slicing, which can be used to combine several planes to show specific connections (Figure 1-8).

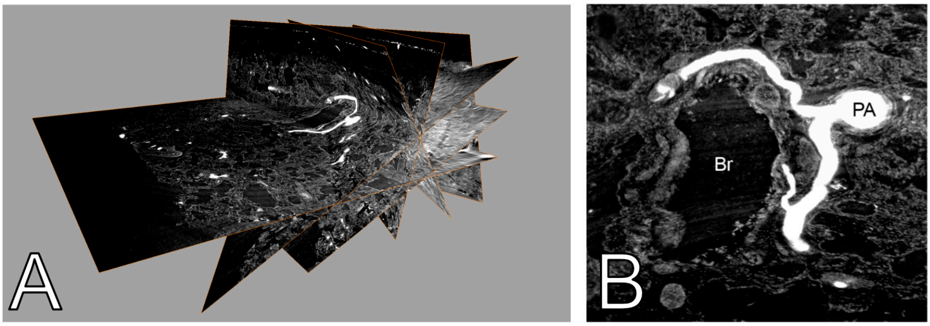

Figure 1-8: Virtual histology concept.
The 3D volume can be sliced along arbitrary planes (**A**), in order to trace connections which would be difficult to follow in just a single slice. A picture of the central part in A from a different point of view is shown in **B.** In this case, the highly attenuating contrast dye shows an anomalous connection between a pulmonary artery (PA) and the bronchial arteries surrounding an airway (Br), in human pulmonary hypertension. Standard histology by physical slicing of the sample would risk missing this important connection. SRμCT scans performed at the TOMCAT beamline at PSI; the PA cross-section in B is approximately 100 μm wide. Figures adapted from (Norvik et al., 2020).

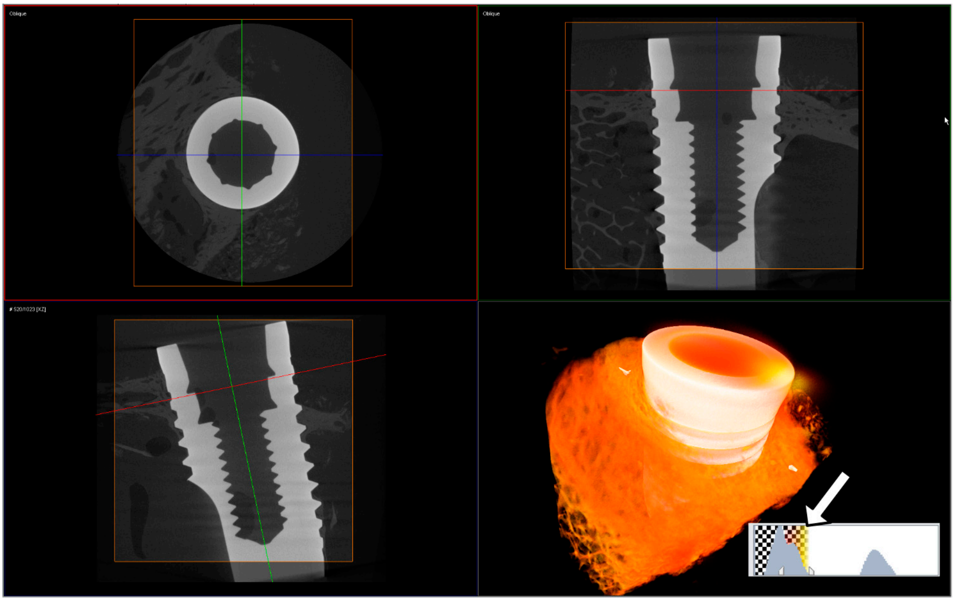

Figure 1-9: Volume rendering concept.
Example of volume rendering (using Amira) to visualise the 3D structure of a titanium implant in rabbit bone (embedded in synthetic resin), scanned with lab-based x-ray μCT (the screw diameter in the uppermost part is 4 mm). The software shows slices along the three orthogonal directions, for easier navigation, and a rendering with adjustable transfer function (bottom right). By properly setting the transfer function window (arrow), the bone can be visualised in 3D and separated in colour from the screw, without any need of additional data processing. Unpublished data.

A 3D representation of the volume can also be given using volume rendering (Figure 1-9), a displaying technique that associates to each voxel of the image a certain colour and opacity, connected to the voxel intensity by a defined transfer function. In some cases, the datasets present enough contrast that interesting features can be already visually separated from the rest by adjusting the transfer function. More often, a prior segmentation of the features of interest is necessary, as will be explained later. All of the visualization programs mentioned above allow to perform volume rendering of the datasets; many other specialized volume rendering programs also exist.

A visualization of the data will be obviously necessary at every step of the image analysis pipeline, to evaluate the effect of applied algorithms and identify noise or artefacts to remove. As such, visualization is not to be considered a separate step from the following ones, but rather an integral one to all of them.

That said, when it comes to imaging of biomedical samples, many times interesting qualitative results can be achieved just by simple visual inspection of the volumes. Since most medical doctors are accustomed to analysing samples with histology, the possibility to perform 3D virtual histology by arbitrarily slicing the volume is often enough for them to identify pathologies or features of interest in the data. In those cases, only minor pre-processing is sometimes necessary, usually to remove artefacts or noise and to enhance the contrast. This has been the case for several projects in the present doctoral work: in Papers II and III for example, an in-depth analysis of x-ray tomographic slices has been carried out by an expert pathologist.

For a more complete, and especially quantitative, analysis of the data, a series of other steps is necessary.

1.2.2 Pre-processing and enhancement

Most of the time, the images acquired with a tomographic scan are not immediately ready to be processed with image analysis algorithms. They will usually present at least artefacts and noise, which could disturb the evaluation of the properties of interest. Some analysis algorithms are also more effective on data that have specific characteristics, which might not be how the acquired data present themselves initially.

Pre-processing and enhancement algorithms aim to prepare images so that they can be used efficiently by other types of algorithms.

A first pre-processing step typically happens even before the tomographic reconstruction. Acquired projections are corrected for the uneven illumination and detector response by using flat field images (i.e. images without object) and dark images (i.e. images without source). A series of artefact correction algorithms are also applied before the reconstruction. Notable examples are algorithms for the removal of ring artefacts (which are typically caused by dust or defects on the detector) or for the correction of beam hardening effects (caused by the polychromaticity of the source).

Another artefact frequently encountered in this work was the one linked to local tomography, i.e. to the fact that during the scan parts of the object can remain outside of the field-of-view (very typical in the case of high-resolution zoom-in scans of selected portions in a histology block). Depending on the shape of the object, this can introduce intensity gradients in the axial slices of the tomogram that can negatively affect subsequent steps of the analysis. An easy work-around consists in fitting a plane in each slice (after blurring or masking out features that could disturb the fit) and normalising the slice for the fitted plane.

When it comes to noise removal or feature enhancement, a big class of image processing operators is the one of filters. They are based on the concept of replacing the value of pixels by a function of the values of neighbouring pixels (local filters) or of larger regions of the image (non-local filters). Most notable applications include image smoothing (Gaussian, median or non-local means filters, as shown in Figure 1-10), edge enhancement (Laplace and Sobel filters), feature enhancement or removal (morphological filters, such as minimum or maximum filter, tophat, skeletonization). A particular filter that is extensively used for enhancing vessel structures, encountered in this work, is the Frangi vesselness filter, which enhances vessel- or tube-like structures by using the eigenvectors of the image Hessian (Frangi et al., 1998).

Another important class is the one of affine transformations, such as scaling, rotations, translations and mirroring. Scaling in particular, coupled with cropping, is useful (often even necessary) to reduce the memory size of the images, in order to make them more manageable in successive steps of the analysis or just for a volume rendering.

Overall, there is a huge variety of processing algorithms, all tailored to different purposes and datasets. A good introductory book on the subject is Digital Image Processing by Rafael C. Gonzalez and Richard E. Woods (Gonzalez and Woods, 2008).

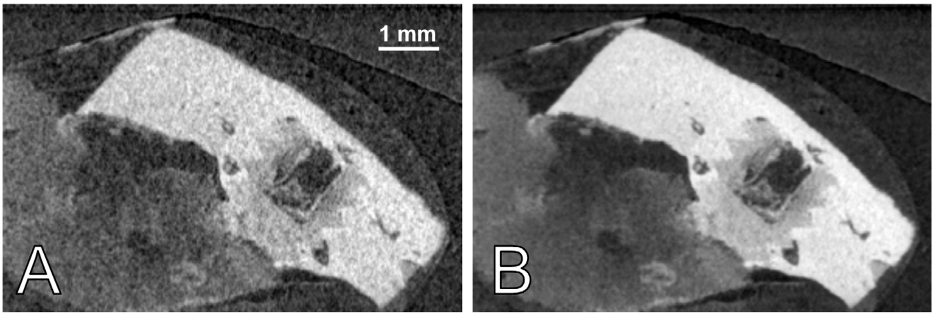

Figure 1-10: Example of smooting filter applied to neutron µCT scans of biodegradable implants in bone. A non-local means filtering algorithm (Buades et al., 2005), implemented in Amira, was used to reduce the salt-and-pepper noise, caused by the low neutron flux at high-resolution imaging experiments. Compared to the non-filtered image (**A**), the filtered image (**B**) shows better signal-to-noise ratio, and improved visibility of the features. Data acquired as part of Paper V.

As mentioned, many programs already listed in the image visualization section also allow to perform image processing with various degrees of complexity. One which was extensively used during this work is FIJI (Schindelin et al., 2012), as it provides a huge variety of plugins developed by users that allow to rapidly test different methods with minimal effort. To have more freedom in developing new algorithms, toolboxes for image processing are also available in the more open-ended coding environments, such as MATLAB or Python (notable example in the case of Python is the Scikit-image library (van der Walt et al., 2014)).

1.2.3 Segmentation

A necessary step to perform quantitative analysis is to identify the interesting features in the image and assign to them labels, which will allow to select them separately from the rest of the volume. The attribution of different labels to different regions of the image is called segmentation and is one of the most difficult tasks of image analysis.

One simple way to achieve segmentation is to do it manually, by drawing on the images the regions to be labelled. While that typically guarantees good results, it is also very time-consuming. A single volume measured at a synchrotron radiation facility is usually formed by one or two thousand slices, each around 2000 x 2000 pixels in size. Multiple features can be present in a single volume, and multiple volumes are typically measured during a beamtime (at the TOMCAT beamline at PSI or in the parallel configuration of the GINIX end-station at DESY, where parts of the present work were done, a volume of that size is produced in just 3 minutes of scanning time). Despite the existence of ways to speed up the manual segmentation (such as label interpolation across different slices), the only reasonable way to analyse all the data produced by a big facility is to develop methods for fully-automatic or semi-automatic segmentation.

Like in the case of pre-processing algorithms, segmentation algorithms are extremely varied and numerous. In most of the cases, they are specifically tailored to each individual set of data (which is often a problem when one tries to apply published methods to different datasets). Once again, a good introductory textbook is Digital Image Processing by Rafael C. Gonzalez and Richard E. Woods (Gonzalez and Woods, 2008).

Image segmentation algorithms are typically based on one of two basic properties of intensity values: discontinuity and similarity. In the first category, the approach is based on identifying sharp changes in intensity; a notable example is edge detection (Gonzalez and Woods, 2008), which is helped by edge enhancement filtering. The main approach of the second category is identifying regions of the image that are similar according to certain pre-defined criteria. The simplest example of this is given by thresholding (Gonzalez and Woods, 2008), where the labels are assigned depending on a partitioning of the grey-level histogram. Thresholding is a staple of image segmentation because of its simplicity and very fast processing speed. However, it is very easily hindered by inhomogeneous illumination (as shown in Figure 1-11), noise, artefacts or in general poor contrast in the images. Nevertheless, thresholding segmentation has been successfully employed in several projects encountered during this doctoral work, either by exploiting natural high-contrast of features, such as for bone and metal implants in Paper IV, or by using contrast agents that greatly increased the intensity of structures of interest, as in (Norvik et al., 2020) and (Westoo et al., 2021).

A higher step in complexity is given by region-based methods, such as region growing (Gonzalez and Woods, 2008), in which from a starting "seed" point a region is grown by appending neighbouring voxels that satisfy a certain similarity condition (for example based on grey level thresholding). A problem of these methods is however to define a proper stopping condition for the region growing, which again will be disturbed by artefacts and poor image contrast. Region growing is at the basis of the "Magic wand" semi-automatic segmentation tool in Amira, which has been successfully employed for segmentation in Paper II.

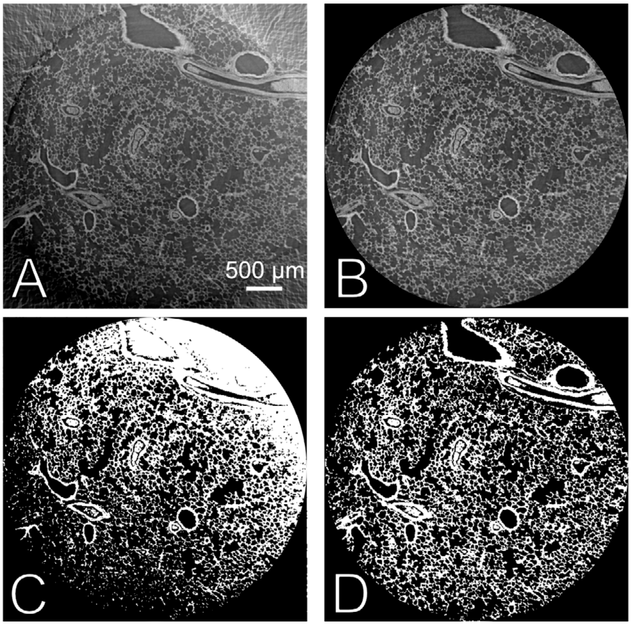

Figure 1-11: Importance of pre-processing on the subsequent automatic segmentation.
A – A SRµCT scan of lung tissue (acquired at the TOMCAT beamline) presents an intensity gradient between bottom right and top left corner, caused by local tomography and the irregular shape of the sample (the corners of the image, which are normally unusable, are being shown for an easier visibility of the effect). **B –** The artefact can be removed by normalisation with a fitted plane, as in (Lovric et al., 2017). **C –** Segmentation by automatic thresholding of the non-corrected image A is greatly affected by the intensity gradient. **D –** Automatic thresholding performs much more convincingly in the corrected image B. Unpublished data.

More advanced methods combine discontinuity and similarity for more robust segmentation results. A notable example is given by morphological watershed

(Gonzalez and Woods, 2008). The main concept (in 2D) can be understood by interpreting the image as a 3D "topographic" map, with two spatial coordinates and a height given by the image grey-levels (a schematic overview in one dimension is also provided in Figure 1-12). Supposing that the entire map is flooded with water from below at a constant rate, different basins will start to fill. As soon as two basins would merge together, a dam is built to prevent the merging. At a certain point, only the dams will remain visible; these dam boundaries correspond to the watershed lines returned by the algorithm. A segmentation with this method is very successful to label blob-like objects from the background. In order to create sharper "height maps", it is usually combined with edge-enhancement filtering beforehand. While this method has not yet been used for published work in this thesis, its implementation in the "Carving workflow" of the ilastik software (Berg et al., 2019) has allowed a relatively easy segmentation of data similar to the ones presented in Paper II, for a follow-up paper to it which is currently in preparation.

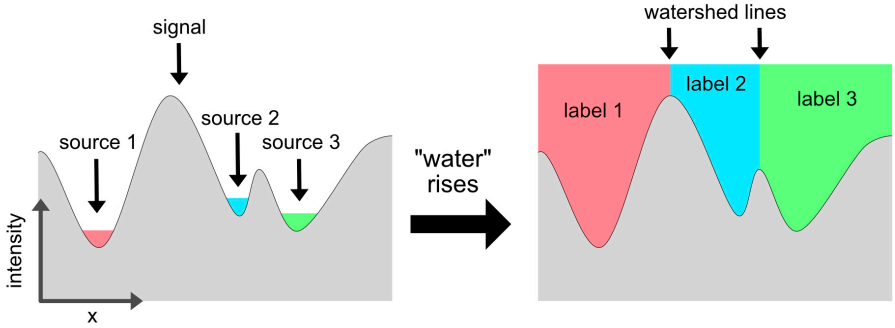

Figure 1-12: Schematic overview of the watershed segmentation in one dimension.
The input image can be considered as a topographic map, with height proportional to greyscale intensity. A water source is placed in each regional minimum. Next, the entire relief is flooded from the sources and dams are placed where the different water sources meet. The water basins become the segmentation labels; the dams are called watershed lines, and can be also used for other applications of image analysis.

Even more advanced morphology segmentation methods are active contours (Yushkevich et al., 2006), which as the name implies find contours of the image by using energy minimising deformable splines (also called snakes). An image "energy" is defined as a function of features of the image (grey scale, gradient, curvature, etc); starting from a seed point, a curve is then iteratively modified in order to minimize said energy. Active contours are typically successful in following complex structures, and in this thesis work have been implemented with mixed success (unpublished) on vessel segmentation, but their implementation on 3D datasets (as surfaces rather than curves) tends to be computationally intensive.

Finally, a class of segmentation methods which appears to be future of image analysis is based on machine learning. Machine learning algorithms typically build an energy-cost model based on sample data, known as "training data", from which the computer is able to make predictions or decisions without being explicitly programmed to perform the task. Even though some of these methods might have been useful for the studies performed in this thesis, and some of them have been explored (by more knowledgeable colleagues) in Paper I, autonomous attempts at their implementation during this doctoral work have not produced significantly worthwhile results. More time and knowledge would have been necessary to really assess their potential, which has nevertheless been shown in several recent publications, for example (Kuan et al., 2020).

All the aforementioned programs and toolboxes for image processing offer implementations of at least basic algorithms for data segmentation. More advanced and niche methods can be found in other specialised programs or can be coded using toolboxes. A notable example of a software package is the already mentioned ilastik (Berg et al., 2019), which aside from the watershed implementation detailed above also incorporates several supervised machine learning workflows, which have shown promise in recent applications of x-ray virtual histology (Eckermann et al., 2020, Frohn et al., 2020).

1.2.4 Quantification

Once a dataset has been labelled, quantification of the label properties can be performed. Probably even more than anything else in the image analysis field, quantification methods are obviously dependent on the scientific question behind the measurement and as such can vary a lot. The most straightforward quantification is to measure the volume of an object, which can be achieved by simply counting the number of voxels in the corresponding label. Other kinds of quantification can involve the shape of the object, or its intensity value (which, depending on the contrast method, is linked to density of a physical quantity). Different objects in an image can be classified according to different properties, in order to perform statistical analysis on the distributions and trends.

In the case of medical samples, the quantification aspects should always be discussed with the medical doctors, since they are usually the ones bringing forward the scientific questions. In many cases, they are already used to measure parameters in 2D histology; the trick is then to extend the quantification method from 2D to 3D. Other times, the 3D aspect can give unique insights.

Different tools can be used for image quantification, often in combination. As an example, in Paper II the evaluation of the thickness of filament structures has been achieved by combining a distance map transform and a skeletonization algorithm. The former associates to each voxel in a binary label a value which corresponds to the shortest distance from it to the boundary of the label itself. The latter "shrinks" down the label to a skeleton, formed by the points that are equidistant from its boundaries. If one evaluates the distance map only on the skeleton voxels, the result is a point-by-point estimation of the label maximum radius along its main axis of propagation.

1.3 X-ray elemental mapping techniques

While x-ray radiography is based on detecting how the probing radiation is affected by its interaction with the object, x-ray elemental mapping techniques are based on inducing and measuring characteristic x-ray emission (also known as x-ray fluorescence emission) by the object itself.

To induce x-ray emission, the specimen is irradiated with ionising radiation, i.e. radiation with enough energy to remove atomic electrons. Different types of excitation sources are possible, corresponding to differently named techniques. In this thesis work, two separate excitation sources were employed: electrons, in what is commonly named energy dispersive x-ray spectroscopy (EDX), and x-rays, in what is known as x-ray fluorescence (XRF).

Independently on the type of excitation, when its energy is high enough to eject an electron from one of the innermost atomic levels, a vacancy is left behind, resulting in an unstable configuration of the atom. To restore equilibrium, an electron from a higher energy outer orbital quickly fills the vacancy, and the excess energy may be emitted in form of characteristic x-rays (Figure 1-13A). The energy of these emitted x-rays corresponds to the energy difference between the two atomic shells involved in the transition; as such, because every element has unique atomic configuration and shell energies, a spectroscopic analysis of characteristic x-rays emission can provide insights on the elemental composition of the material in exam.

Since fluorescence emission is isotropic, the easiest way to obtain spatial resolution, and hence an image, is to focus the excitation source in a small beam, and then either move the beam (easily done in the case of electrons) or gradually shift the position of the sample (preferred way in the case of x-rays) in order to progressively illuminate a grid of points centred on an area of interest, in a raster scan pattern (Figure 1-13B). On each point, the source is usually allowed to rest for a certain dwell time, and the resulting fluorescence is measured by a spectrometer, which discriminates the photon energy. The ending result are images with two spatial dimensions, which correspond to the position of the points in the grid (with a spatial resolution corresponding to the spacing between each point), and a spectral dimension, which corresponds to a fluorescence energy range sampled with a certain energy resolution, dependent on the fluorescence detector. Methods for performing fluorescence imaging in broad beam geometry also exist, but they have not been used in this thesis work and as such will not be addressed here.

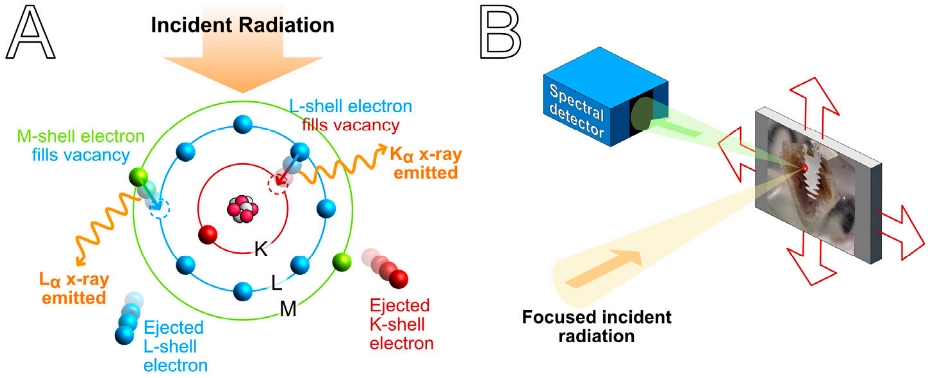

Figure 1-13: Concepts of x-ray elemental mapping.
A – Schematic drawing of characteristic x-ray emission process. Incident radiation (for example x-rays or electrons) can eject electrons from the innermost atomic shells; when this happens, vacancies are left behind, which are quickly filled by more energetic electrons from the outer orbitals. During these transitions, the excess energy, which corresponds to the difference in binding energy between the two orbitals, may be released as characteristic x-rays.
B – Elemental mapping by raster scanning. In order to obtain spatial information, the incident radiation is focused in a small beam, which is then moved across the sample (either by moving the beam or by shifting the sample) in a raster pattern. On every acquisition point, part of the emitted fluorescence is collected by a spectral detector.

On account of requiring the incoming radiation to interact with the sample, and at the same time the emitted fluorescence to exit the sample and reach the detector, elemental mapping analysis is usually considered a surface technique, and the samples need to be physically sectioned in order to access the interface of interest. Electrons in particular have a very shallow penetration range and are able to probe only the first few micrometres of material. X-rays can penetrate more, but they will induce fluorescence from everything along their path; in case of thick samples, this means that the measured signal will not be coming from just the immediately visible surface but will be an average fluorescence along the sample depth.

EDX mapping can be performed by adding a fluorescence detector to a scanning electron microscope; a setup of this sort has been used in Paper IV of this thesis.

XRF mapping is commonly carried out at synchrotron facilities, however compact machines based on x-ray tubes can also achieve micro-beam resolutions. Measures acquired in a commercial µXRF machine have been used for Papers IV and V.

Once a fluorescence dataset has been acquired, the analysis is based on using fitting methods to extract the spectral contribution of the individual elements, based on their characteristic x-ray energies. When this is done on a point-by-point basis, element maps can be extracted (Figure 1-14); the relative peak intensity can also be associated to the relative concentration of the various elements. In most commercial machines, such as the ones employed in this thesis, the analysis is usually conducted using the software provided by the manufacturer. Free software for multispectral analysis also exists, however; a few notable examples, used during this doctoral work (unpublished), are PyMCA (Solé et al., 2007) and the Hyperspy toolbox (Peña et al., 2021), both Python-based.

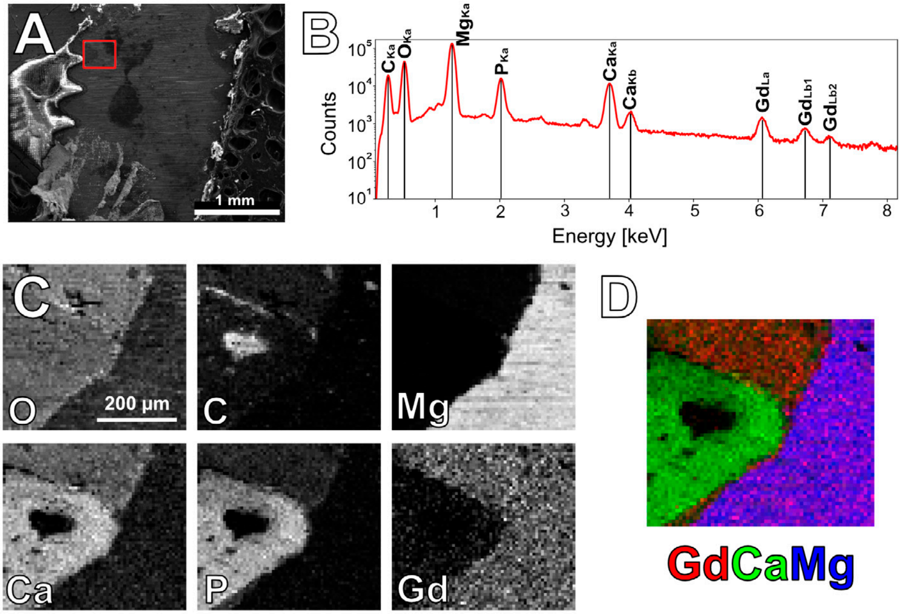

Figure 1-14: Example of x-ray elemental mapping.

A – Using a scanning electron microscope picture for navigation, a small area (in red) is selected to perform EDX analysis. A grid of 256 x 232 acquisitions is performed on the area by raster scanning the electron beam; each acquisition point on the grid has its own fluorescence signal. **B –** The cumulative spectrum of the area, obtained by integrating all the individual acquisitions, can be used to have an idea of the average chemical composition. Six main elements are identified: carbon (C), Oxygen (O), Magnesium (Mg), Phosphorus (P), Calcium (Ca) and Gadolinium (Gd). **C –** By analysing the spectra for each individual acquisition point, the distribution of each element can be mapped. **D –** The maps can be overlapped in false colour images, to highlight correlation between the elements. Data acquired as part of Paper IV.

2 Synchrotron-radiation µCT of biodegradable magnesium-alloy implants: the SynchroLoad project

> *If at first you don't succeed,*
> *try two more times so that your failure is statistically significant.*
> — Anonymous

This Chapter will expand upon the first line of research of this thesis, the study of corrosion behaviour and mechanical properties of biodegradable magnesium implants for osteosynthesis (i.e. bone healing). A first part will describe the main motivations behind the study and provide some necessary background. The experimental and technical aspects will then be detailed, building upon the concepts already introduced in the Theory chapter. Lastly, a final part will aim at presenting Paper I, with particular focus on the radiation damage measurements reported in it.

2.1 Motivation and medical background

2.1.1 Osseointegrated implants

The most common treatment for traumas and degenerative disorders of the skeleton involves the use of osseointegrated implants. These can be built out of different materials and with different shapes and surface coatings, and constant research is made to improve and innovate each one of these design parameters.

Traditionally, implant materials were selected to be as less biologically and chemically reactive as possible, in order to avoid disturbances to the natural healing process of the tissue (Williams, 2012). This is the case for example of titanium and stainless steel, widely used in orthopedy and dentistry, and of several polymer-based implants such as those made from polyetheretherketone (PEEK). Inert, permanent implants can however bring a series of complications, which range from inflammatory effects (Schwarz et al., 2018), to implant loosening and dislocation (Sundfeldt et al., 2006), to even release over time of particles or ions which may prove toxic or cause allergic reactions (Basko-Plluska et al., 2011, Lyu and Untereker, 2009, Vasconcelos et al., 2016). Furthermore, implants very rarely perfectly match the mechanical properties of bone, and as such they inevitably alter the mechanical environment at the implantation site. Bone is known to react to this alteration in unwanted ways: for example, lack of mechanical stimulation of the bone has been linked to bone resorption, which is a known problem in many orthopedic applications (Sumner, 2015). For these reasons, permanent implants for osteosynthesis are removed whenever possible after bone healing, with potential risks to the patients stemming from the second surgery. Implant removal is also especially necessary in the case of young patients, whose growth would definitely be affected by the presence of permanent implants.

Recent developments in implant design have seen a progressive shift from bioinert materials towards bioactive materials, which, as the name implies, are supposed to deliberately interact with the tissue (Huang et al., 2020). Rather than using substances that should simply be tolerated by the body, the aim is to tailor materials that could actively boost the desired outcome, providing for example osteoinductive effects or inhibiting inflammatory responses. An extremely attractive property of bioactive materials is biodegradability, i.e. the potential to dissolve into biocompatible products after having performed their planned function. In the case of osseointegrated implants, an ideal biodegradable material could have its degradation rate and mechanical properties tailored in order to support the bone during the healing process, and then be resorbed after full healing, completely bypassing the need of second surgery (Virtanen, 2011).

Several materials are being investigated and designed as possible candidates for the design of biodegradable implants. The work presented in this thesis has focused on magnesium, and in particular some of its alloys, as element of choice.

2.1.2 Magnesium and its alloys

Magnesium is one of the alkaline earth metals (group 2), it has atomic number 12 and symbol Mg. It is the fourth most common element on Earth, with a high prevalence both in the Earth's crust and also among elements dissolved in seawater (Jahnen-Dechent and Ketteler, 2012).

Given its high reactivity, it occurs naturally only in combination with other elements, but can be extracted in its pure metallic form with artificial methods. Mg and its compounds are used for a wide variety of purposes, which exploit its properties such as high flammability (ex. explosive and pyrotechnic devices) or low density yet high specific strength, which can be further boosted by alloying (ex. Mg-based alloys have found extensive use in the aerospace and automotive industry as lighter alternatives to aluminium).

From a biological perspective, Mg is essential to life, being involved in every biochemical process in cells. Mg deficiency has been shown to have detrimental effects on neurological, cardiovascular, muscular and skeletal systems (Rude, 1998). For the latter in particular, low Mg intake has been linked to higher insurgence of osteoporosis (Castiglioni et al., 2013), as well as to negative impact on the status of articular cartilage (Richette et al., 2007). Even in individuals with normal Mg values, Mg supplementation has been proven to improve bone mineral density and reduce risk of fractures in osteoporotic women (Sojka and Weaver, 1995), as well as produce positive effects in most of the aforementioned other systems.

2.1.3 Magnesium-based biodegradable materials

The potential of Mg as a biodegradable material started being investigated as soon as the commercial production of elemental Mg picked up in the second half of the XIX century (Witte, 2015). The first reported application in this sense dates back to 1878, when Mg wires were employed as ligatures for bone vessels by physician Edward C. Huse. The use of Mg implants for osteosynthetic purposes was explored with experiments on animals and humans in the early XX century by several physicians, who were intrigued by the fact that Mg could corrode in the body with seemingly no toxic effects. Despite the enthusiasm of these early pioneers, the results were often mixed, and the use of Mg as biomaterial declined quickly. A major setback was given by the fact that the implants would often corrode too fast to support bone healing; the fast degradation was also accompanied by quick release of hydrogen gas in the proximity of the implants, which produced swelling and pain. The main limitation at the time was the low purity of the available Mg: impurities introduced during the processing can in fact activate galvanic corrosion in uncontrolled ways, resulting in faster and unpredictable corrosion rate.

Thanks to modern advances in Mg production, today it is possible to obtain ultra-high pure Mg and to design Mg alloys with controlled mechanical and degradation properties; as such, interest in Mg-based biomaterials has seen a big resurgence in recent years, with extensive studies being conducted to develop new Mg alloys with superior mechanical and corrosion performance.

There is an immense variety of Mg-alloy families being currently investigated, as reported in several review articles (Chen et al., 2014, Zhang et al., 2013). The main considerations for element selection are toxicity, strengthening ability and influence on the corrosion behaviour. All these parameters, and others, can be assessed *in vitro* or *ex vivo*, with a wide assortment of techniques. A significant issue, however, is the lack of standardisation (Kirkland, 2012): even the same nominal alloy can present widely different behaviour depending on shape and on the manufacturing process (as already mentioned, impurities greatly affect the degradation process). *In vitro* results can also differ greatly depending on the corrosion medium of choice, and they are never directly comparable to *ex vivo* measurements of the same quantities (Zhang et al., 2013, Sanchez et al., 2015). Lastly, the most common *ex vivo* methods consist in cutting the samples and then performing 2D techniques such as histology, scanning-electron microscopy, fluorescence analysis, or metallographic examination; by virtue of requiring cutting, several of these techniques risk to depend heavily on the cutting plane and miss out on volumetric effects. In some cases, laboratory-based x-ray µCT has been employed to obtain 3D information (both *ex vivo* or even *in vivo* (Dziuba et al., 2013)); however, the usually poor spatial resolution and low density contrast caused by the source polychromaticity have thus far limited these approach to only assess the volume reduction of the implants over time at best, with no insights on the small scale corrosion processes.

In order to finally assert the legitimacy of Mg-based implants as end products in a wide market of possible alternatives, it is crucial to standardise implant manufacturing and characterisation (Kirkland, 2012).

2.2 The SynchroLoad project

2.2.1 Background and goals

The SynchroLoad project, a Swedish-German research collaboration within the Röntgen-Ångström Cluster, was started in 2016 with the aim of exploring two different alloys of Mg and gadolinium (Gd), Mg-5Gd and Mg-10Gd (where 5 and 10 indicate the nominal Gd weight percentage).

Alloying Mg with Gd had already been shown, in previous *in vitro* and *ex vivo* studies (Galli et al., 2016, Galli, 2016), to provide mechanical and corrosion properties comparable or even superior to other candidate alloys. Aside from determining which Gd weight percentage would be preferable and whether it would be possible to establish a direct link between alloy properties and Gd content, a main goal of the SynchroLoad project was to fully characterise the materials with multiple techniques and well documented standards.

As a response to the main points and pitfalls of Mg-alloy characterisation, detailed in the previous section, the list of aims in this sense was to:

1. Provide full detail of the alloying and implant manufacturing process, in order to ensure reproducibility.
2. Compare Mg-5Gd and Mg-10Gd with the most commonly used permanent implant materials, Ti and PEEK.
3. Perform both *in vitro* and *ex vivo* (in Sprague-Dawley rats) corrosion analyses on implants with the same shape and from the same batch, to remove as many manufacturing parameters that could hinder comparability as possible.
4. Use multiple analysis techniques, both already well established and new, to ensure cross-validation and provide a comprehensive picture of the implant corrosion dynamics; in particular, central importance was given to synchrotron-radiation micro-computed tomography (SRμCT) as a tool to discriminate the corrosion behaviour in 3D with high spatial resolution and density contrast, both of *in vivo* and *ex vivo* samples.
5. Lastly, as the name of the project itself implied, measure the mechanical properties of *ex vivo* samples by means of SRμCT coupled with *in situ* mechanical loading tests, in order to provide a 3D high-resolution visualisation of the failure mechanisms of the implant-bone interface.

Paper I presented in this dissertation has stemmed from the mechanical testing side of the SynchroLoad project, which will thus be the further described in the rest of this Chapter. The *in vitro* measurements, which provided a microstructure characterisation of the alloys and an estimation of their *in vitro* corrosion behaviour, have been collected, together with full details about the alloy production procedures, in a very recent publication (Krüger et al., 2021b) and will not be discussed further. Similarly, *ex vivo* analyses of the corrosion behaviour by means of SRμCT, which however do not include any mechanical failure analysis, are the topic of a manuscript currently in press (Krüger et al., 2021a) that has not been included in this thesis.

2.2.2 Samples

Mechanical testing of the implant-bone interface clearly had to be performed on *ex vivo* samples. The Mg-Gd implants were 4 mm long, 2 mm diameter slotted grub screws, with an M2 thread (Figure 2-1A). As reference material, titanium (commercially pure, grade 4) and PEEK screws, purchased from Promimic AB (Mölndal, Sweden), were also used.

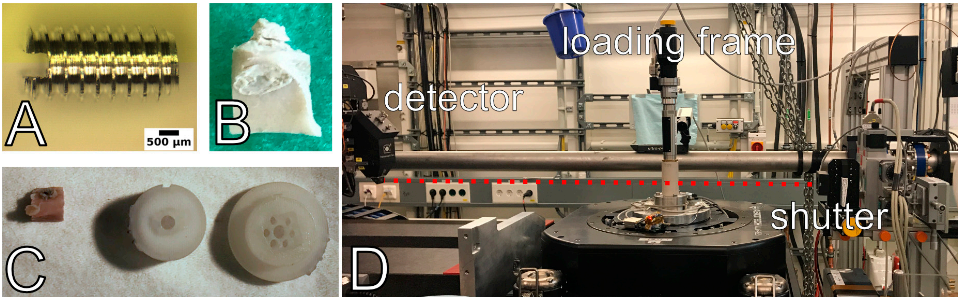

Figure 2-1: Details of SynchroLoad experiments.
A – Mg-Gd implant, in the form of 4 mm long, 2 mm diameter slotted grub screw. **B –** Critical point dried bone-implant explant. **C –** Wet bone-implant explant (on the left) next to 3D-printed sample holders for mechanical testing. **D –** Setup for SRµCT coupled with in situ mechanical loading. The red dotted line indicates the x-ray beam path from the shutter (on the right) to the detecting system (on the left). Photos courtesy by Silvia Galli.

After sterilisation, the screws were implanted in the hind legs of Sprague-Dawley rats (comprehensive details about the animal experiments have already been provided in other publications, ex. (Zeller-Plumhoff et al., 2020), and are also briefly summarised in Paper IV of this thesis). Each rat received either 2 Mg-Gd implants (one of each kind), or 2 control ones (one of each kind). After 4, 8 or 12 weeks of healing the rats were euthanized by a lethal dose of anaesthetic and the legs were dissected to extract the tibiae containing the implants. Cylindrical or box-shaped explants (Figure 2-1B), with a diameter/width of 5 mm, were then cut in order to fit within the field-of-view of the tomographic scans and inside the loading device for mechanical testing.

While the samples that had to be used for *ex vivo* corrosion analyses were dehydrated for easier preservation and storage, 72 explants (6 for each of the 4 material at each of the 3 time points) were kept frozen for the mechanical loading tests (Figure 2-1C), as dehydration would have clearly modified the mechanical properties of the interface.

2.2.3 Synchro+Load methods

The German counterpart within the SynchroLoad project is the Helmholtz-Zentrum Hereon in Hamburg, which among other things operates the imaging beamline (IBL) P05 (Wilde et al., 2016) at the PETRA III storage ring of the Deutsches Elektronen-Synchrotron (DESY), in Hamburg, Germany. As such, most of the SRµCT measurements were performed there.

The beamline consists of a front-end, which contains undulator, slits and filters, an optics hutch equipped with a double crystal monochromator and a double multilayer monochromator, and two experimental hutches, a first one dedicated to nano-tomography (not used in this work) and a second one, more downstream, for micro-tomographic use.

While the µCT end-station is capable of performing phase-contrast imaging (Wilde et al., 2016), and the method had been initially explored for the SynchroLoad samples (Moosmann et al., 2017), it was ultimately decided to only employ attenuation-contrast tomography for the mechanical load tests. The imaging setup was thus very simple conceptually, consisting only of source (the undulator), sample rotating stage and flat panel detector (Figure 2-1D).

The measurements were performed during several beamtimes and with various settings due to technical problems with the monochromators and cameras. Initially, a photon energy of 34 keV was mainly used (out of an available 5-50 keV energy range); however, as mentioned in the next section and in Paper I, the photon energy was set to 45 keV towards the end of the project. The detecting system comprised a cadmium tungstate (CdWO4) scintillator screen, then a set of optical microscope optics (set to 5X magnification for all the scans) coupled to a solid-state camera. Two cameras were used in different moments: one with a CCD (charge-coupled device) sensor (KAF-09000) with 3056 x 3056 pixels, a 16-bit dynamic range and a pixel size of 12.0 µm (effective pixel size of 2.4 µm when considering magnification), and another with a CMOS (Complementary metal–oxide–semiconductor) sensor (CMOSIS CMV 20000) with 5120 x 3840 pixels, a 12-bit dynamic range and a pixel size of 6.4 µm (effectively 1.2 µm with 5X magnification). The number of projections and the scanning time had to vary depending on the employed camera and on the selected energy (which influences the scintillator efficiency). Typically, 1200 projections of 50 ms each were acquired for the CCD camera, however the long detector read-out time meant scan times in the order of 1-1.5 hours per tomogram. A higher number of projections (between 2400 and 3000) had to be used for the CMOS camera, because of its higher noise and lower dynamics; however, the faster read-out meant overall faster scan times when compared to the CCD. Data pre-processing and tomographic reconstruction were implemented in MATLAB environment, using the tomographic reconstruction pipeline at IBL (Moosmann, 2021).

In order to perform *in situ* mechanical testing during the SRµCT scans, a loading frame was developed and fully integrated into the beamline control system. The load frame design is the main topic of Paper I, but was not the focus of this thesis work and as such only a few more important details will be described here. In brief, the frame is modular in its shape and allows different mechanical testing configurations. It requires to pre-scan the samples (with lab-based µCT) in order to design 3D-printable sample holders (Figure 2-1C), which will fit inside the frame and ensure perfect match between the sample and the loading device. While in principle the frame can apply and monitor force in real time, the slow scanning time of the imaging system required to perform the loading tests in a static way, with progressively increasing force steps.

The protocol of choice was the following:

1. A first tomographic scan is acquired with no loading.
2. The force is then increased by small steps (initial tests were carried out with 2.5 N steps), which have to be adjusted after initial estimations of mechanical failure in order to reach the breaking point in around 10 total steps, to provide enough acquisition points of the loading curve.
3. In-between each force step, to account for relaxation processes, the system is kept in static loading conditions for a fixed amount of time (initial tests waited for 20 minutes), during which the applied force is constantly measured and radiographic pictures are acquired. After relaxation, a full tomographic scan is then acquired for each force step.
4. Once mechanical failure is reached, a last tomographic scan is acquired.

The acquisition of tomographic images at different loading steps would have allowed to assess volumetric displacements and strain within the samples during loading, by means of an analysis technique known as digital volume correlation. The method is already well established for the study of bone mechanical properties (Roberts et al., 2014, Grassi and Isaksson, 2015), and can be implemented with several algorithms. An early attempt at performing digital volume correlation on one of the SynchroLoad samples, using the Tomowarp2 code (Tudisco et al., 2017), is presented in Figure 2-2. In Paper I, a different approach using optical flow (Horn and Schunck, 1981) was implemented by a co-worker.

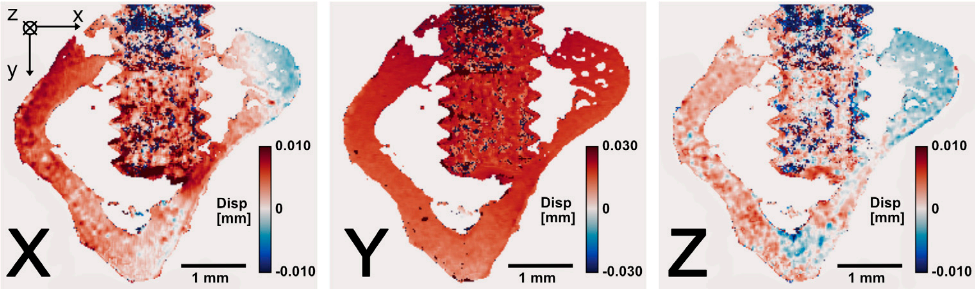

Figure 2-2: Digital Volume Correlation of a SynchroLoad sample.
Digital volume correlation performed by using the Tomowarp2 code (Tudisco et al., 2017). The method allows to evaluate minute displacements over repeated scans, which in the case of loading tests can be directly linked to mechanical strains and stresses, and highlight the formation of cracks. The analysis in figure was performed with a load between 0 and 2.5 N, after which cracks already started forming in the sample. The displacements along the x, y and z directions (a legend of which is provided in the top left corner, with the z axis entering the picture) are displayed in false colour maps. The Y-displacements map shows that the sample was almost homogeneously moving downward; differences in deformation direction in the X and Z displacements maps (blue vs red) point to the development of the crack, which was localised where the screw touched the bone in the bottom part (see also Figure 2b of Paper I). NOTE: the displacements measured inside the screw are to be considered noise, as the material was too homogeneous for a correct use of the technique.

2.3 Radiation damage issues and other problems

When initial *in situ* loading tests were performed, the critical failure force values were found to be quite lower than expected, even for the controls (around 30 N at most; typical values for Ti-bone interface, while dependent on healing time, were expected to be at least two or three times as much for comparable times (Castellani et al., 2011)). No significant difference was observed between controls and Mg-Gd alloys; furthermore, when analysing the post-failure SRµCT images, the fractures appeared to be mostly localised in the bone, rather than in the implants or at the interface. While it would have been excellent to conclude that both Mg-Gd alloys had mechanical properties on par with Ti, the sad truth was that an important effect of ionising radiation had been overlooked: radiation damage.

2.3.1 Radiation damage effects on bone

When dealing with ionising radiation, such as x-ray photons, an important point of concern is the one of radiation damage. By transferring their energy to the atomic electrons of the target, ionising particles intimately affect the biochemistry of the affected tissue, causing several damaging effects.

A bibliographic search revealed pre-existing work on the topic of radiation damage to *ex vivo* bone by Barth et al. (Barth et al., 2010, Barth et al., 2011), who reported a deterioration of the mechanical properties of human cadaveric bone, resulting in reduced strength, ductility and toughness, after high-dose exposure to synchrotron radiation. In those studies, several typical radiation doses were evaluated, ranging from 25-35-70 kGy (common doses during gamma sterilisation of bone grafts to be used in surgery) all the way to 210 and 630 kGy (evaluated as typical doses received during one or three SRµCT scans, respectively). A suppression of plastic deformation was observed already at 70 kGy, due to the reduction of strain carried by the collagen fibrils, which are normally the major responsible of tensile strength in the bone.

While Barth's results suggested a critical threshold of 35 kGy to avoid radiation damage, it was decided to perform a mechanical test, similar to the one reported by Barth et al., on leftover rat bone samples from the animal experiments, to have a more direct comparison with our case. The procedure closely followed the methods in (Barth et al., 2010). In brief, leftover femoral rat bones (three per dose point) were cut in rectangular prism shapes and then irradiated to 0 kGy, 5 kGy, 20 kGy, 35 kGy, and 75 kGy. The dose was estimated analytically, as in (Barth et al., 2010), by considering mass and attenuation coefficient of cortical bone and assuming a reasonably uniform x-ray absorption within the sample; it was then administered to the samples by placing them in the beam at the synchrotron end-station and performing mock-up SRμCT acquisitions of variable duration. During exposure, the samples were continuously rotating in order to maintain exposure homogeneity. They were also immersed in HBSS (Hank's balanced salt solution) to avoid dehydration.

Following exposure, three-point bend tests were performed on three samples per irradiation level, using a support span of 12 mm, an applied force diameter of 2 mm and a displacement rate of 10 μm/s. The end results, presented in Paper I, revealed a deterioration in the mechanical properties starting at 35 kGy, in fairly good agreement with the observations by Bart et al. on human cortical bone.

An estimation of the dose deposited on the SynchroLoad samples during SRμCT, also reported in Paper I, revealed that, at the initially used energy range of 34 keV, one single tomogram would in the absolute best conditions (without even accounting for exposure during scan setup) irradiate the sample for over 4.25 kGy. Considering the need for a first tomographic scan with no loading, and then around 10 additional scans in order to accurately sample the loading curve, the total dose would have been above the critical threshold. The simulation also showed that the exposure could be possibly reduced by performing scans at a 50 keV energy (the maximum available at IBL). Because of poor behaviour of the monochromators at the extreme available range, a slightly lower energy, 45 keV, was adopted for the subsequent experiments.

2.3.2 Other issues and hiatus

Despite the efforts to lower the dose, several issues with the cameras and with the shutters meant that the calculations presented in Paper I were rarely representative of the effective dose on the sample.

Further problems also came to light: a first one, already partly tackled in Paper I, had to deal with the loading geometry of the samples (Figure 2-3). While typical mechanical testing of osseointegrated implants is performed by removing the screw by "pulling it out" or unscrewing it (depending on the test being performed), these methods are not applicable to biodegradable implants as it is highly probable that the head of the screw will have changed its shape during corrosion, preventing the use of standard pull-out devices. When the tests were originally planned, it was thus decided to adopt a "push-in" configuration, in which a loading pin would displace the screw towards the inside of the bone. This method relied on the assumption that the implants would be in contact only with one part of the cortical bone, remaining free to move in the bone marrow inside. However, when the first tomographic scans were performed, it appeared clear that most of the screws were accidentally "bi-cortical", i.e. implanted so deep that the screw had penetrated through the bone and perforated (partly or fully) the other side of cortical bone. A possible solution, proposed in Paper I, was to assess the situation in the pre-scans using lab-based µCT, eventually surgically remove the bottom cortical bone and mount the samples upside down in the loading frame, essentially "pushing out" the screw. This approach however introduced several challenges in sample preparation, and the effects of the cortical bone removal on the elasticity of the remaining bone were questionable at best.

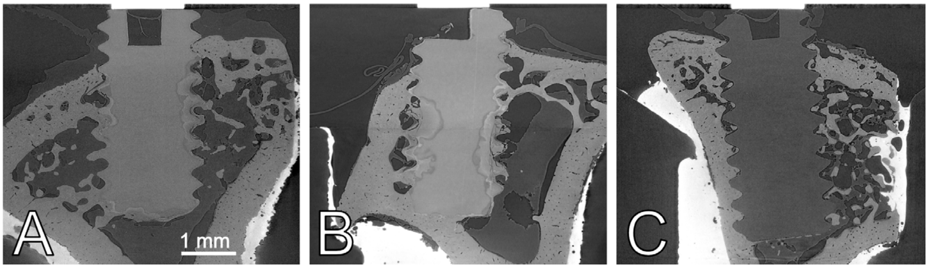

Figure 2-3: Examples of good and poor loading geometry.
A – Good loading geometry; even though some trabecular bone has formed in the bottom part of the implant, there is still enough room to assess the strength of the bone-implant interface correctly. **B –** Poor loading geometry; the screw is bi-cortical, penetrating in the dense bone also on the bottom side; the result of loading tests by pushing from the top is questionable, but the situation might be improved by surgically removing the bottom bone and mounting the sample "bottom up" in the loading frame, as proposed in Paper I. **C –** Very poor loading geometry; the screw (made out of PEEK, hence the low attenuation) is completely in contact with the cortical bone on the side, probably impossible to salvage for loading tests.

A second significant issue was the overall duration of the loading tests (at least several hours), which would clash with the necessity of keeping the explants hydrated. Attempts were made at wrapping the samples in soaked tissue, however movement artefacts would be introduced by the drying process. The most desirable solution, an improvement of the scanning speed, was unfortunately delayed by several technical issues with the experimental setup.

In conclusion, the research presented in Paper I and summarised in this Chapter determined an interruption of the mechanical testing part of the SynchroLoad project, until improvements of the experimental setup would become available. The critical dose threshold of 35 kGy which had been established for human bone by previous studies (Barth et al., 2010, Barth et al., 2011, Currey et al., 1997), was confirmed to be realistic for rat bone as well. At the time of the first scans and first issues, not much attention had been dedicated in literature to the issue of radiation damage caused by SRµCT scans of *ex vivo* bone samples (with the exception of the exemplary work by Barth et al. (Barth et al., 2010, Barth et al., 2011), and an even older study, focused on gamma sterilisation of human bone grafts, by Currey et al. (Currey et al., 1997)). In very recent years, the topic has garnered more attention, and an extensive evaluation of the effects of SRµCT analyses on the mechanical integrity of bovine trabecular bone has been performed with in situ testing by Peña Fernández et al. (Peña Fernández et al., 2018), once again finding a critical threshold around 35 kGy.

While mechanical testing was no longer carried out during this thesis, a different line of work was initiated within the SynchroLoad project, as will be detailed in Chapter 4.

3 X-ray high-resolution CT for the evaluation of neuropathy in gastrointestinal dysmotility

Everything is better when it rotates.
— O.v.d.H., M.D.

This Chapter presents an application of high-resolution x-ray CT to the study of neuropathy associated to gastrointestinal dysmotility. A first part will describe the necessary background and provide a motivation for the study. The employed methods will then be briefly discussed. Lastly, an overview of the main results and conclusions of Paper II and Paper III will be provided.

3.1 Motivation

3.1.1 Medical background

The gastrointestinal tract extends from the mouth to the anus and has its own nervous system, the enteric nervous system (ENS), which rather independently regulates bowel functions (Furness et al., 2014). The ENS has submucosal ganglia (clusters of neurons), that can be reached through endoscopy, and deeper less accessible myenteric ganglia between the two muscle layers, which demand full-thickness biopsy through surgery (Keller et al., 2018). Due to its location, diseases in ENS are seldom studied, and often overlooked (Keller et al., 2018, Gatopoulou et al., 2012).

When abdominal pain and altered bowel habits are not accompanied by any objective structural changes in routine clinical examinations, the patient is diagnosed with functional bowel disorders (Lacy et al., 2016). The most common of these is irritable bowel syndrome (IBS), with a worldwide prevalence of 4%-10% in the population (Sperber et al., 2021). Since the patients get no explanations to their symptoms, they continue to search for help at different instances, with significant costs for society.

When clear structural changes are apparent, the diagnosis of enteric neuropathy is set, and the patient gains improved access to health care and economic support; different treatment strategies also become available. An appropriate diagnosis is thus essential for the patients, but the difficulty in reaching and examining the ENS means that often the exact diagnosis depends exclusively on the degree of examination.

Previous histopathological analyses of full-thickness biopsies have shown changes in the myenteric ganglia of individuals diagnosed with IBS (Ohlsson et al., 2018), suggesting neuropathy as a possible cause for some IBS symptoms. Extraction of full-thickness biopsies is however a very invasive procedure, which may lead to perforation of the bowel wall, hence why these biopsies are only performed in severe cases of disease, with aggravating symptoms.

In recent years, methods to obtain submucosal biopsies have been developed, with less risk of perforation (Rajan et al., 2016, Walther et al., 2016). This raises the opportunity to study submucosal plexa, which register visceral sensitivity/pain; if neuropathy could be assessed in the submucosal plexus in association with IBS, an easier way to perform a diagnosis may become available. Several studies have also documented biochemical and structural alterations in peripheral nerves in diabetes (Thomsen et al., 2009, Løseth et al., 2016, Ekman et al., 2020), which are related to abdominal complaints; establishing a connection between alterations in the peripheral nerves and neuropathy of the ENS could enable the use of far less intrusive skin biopsies as a way to diagnose certain types of enteric neuropathy. Skin biopsies are already used in the assessment of several diseases of the autonomic nervous system (of which the ENS is a part) (Wang and Gibbons, 2013), so the connection, recently observed (Ohlsson et al., 2020) but still unconfirmed when the study described in this Chapter was initiated, appeared as quite plausible.

3.1.2 X-ray high-resolution CT as virtual histology

The most commonly used techniques in the evaluation of ENS or skin biopsies are histopathological and immunochemical examinations by means of light microscopy and confocal fluorescence microscopy. While these methods provide high magnification and specificity, they present several downsides: they require slicing of the sample in 3-5 µm thick sections, are time-consuming and only provide structural information in 2D planes. Volumetric results have been obtained by serial sectioning, either physical (Vanderwinden et al., 2000, Toma et al., 1999, Grover et al., 2012) or optical (with confocal fluorescence microscopy) (Cobine et al., 2011), at the cost of an even longer time to perform the analyses; the depth resolution of sectioning approaches is also fairly limited, which makes it difficult to determine the connections between the different components of the ENS. Very recently, a different method has been introduced for 3D confocal microscopic examination of human intestine without embedding and sectioning (Graham et al., 2020); the technique however requires several time-consuming preparation steps, including tissue cleaning and immunohistochemical staining.

High-resolution x-ray CT has the potential to provide 3D information about the ENS structure with minimal sample preparation, no need of physical sectioning, and with isotropic resolution. The volumetric datasets could then be digitally sectioned along any arbitrary direction, to perform so-called virtual histology. The concept of virtual histology has gained a lot of attention in recent years, as one of the most significant advantages of state-of-the-art high-resolution CT methods over traditional histology (Khimchenko et al., 2016, Albers et al., 2018). Lab-based µCT, both with standard absorption contrast (Khimchenko et al., 2016) and with phase contrast (Töpperwien et al., 2018), has been proven to provide enough contrast and resolution to visualize individual cells in human cerebellum. Synchrotron-based techniques, such as hard x-ray nano-holotomography (nHT) (Cloetens et al., 1999), have also been successfully employed in the study of the human cerebellum at nanometre resolution (Töpperwien et al., 2018, Khimchenko et al., 2018), even beyond the optical resolution limit. The use of these techniques appeared thus quite promising to assess ENS and peripheral nervous system.

3.1.3 Goals of the project

A collaboration was initiated with Bodil Ohlsson's research group at the Department of Clinical Sciences in Malmö (Lund University), with the plan to employ lab-based x-ray phase-contrast µCT and synchrotron-based nHT for a threefold purpose:

1. Evaluate morphological changes of the myenteric plexus in health and disease.
2. Determine if structural alterations can be observed in submucosal plexus in certain types of enteric neuropathy and, if so, whether they can be linked to alterations of the myenteric plexus.
3. Compare alterations between enteric nerves and peripheral nerve fibres in skin biopsies.

3.2 A multi-scale analysis

The study was performed on full-thickness biopsies and matching skin biopsies from sick and healthy individuals. After excision, the biopsies had all been fixed in formalin, dried and embedded in paraffin blocks. To match the requirements of the µCT and nHT setups, the sample size had to be reduced. For this purpose, in the full-thickness biopsies representative areas of the ENS with presence of myenteric ganglia or submucosal plexus were identified in haematoxylin and eosin-stained sections. By a 1-mm punch, a biopsy centred on the interesting areas was then extracted from each paraffin block and put into a polyimide tube. The skin biopsies were handled in a similar way, extracting a 1-mm punch with a dissection microscope.

X-ray phase-contrast imaging was performed on tomography instruments designed and implemented by Tim Salditt's group at the Institute for X-Ray Physics, University of Göttingen (Töpperwien et al., 2018, Salditt and Töpperwien, 2020): two laboratory µCT setups (one equipped with a liquid jet anode source, Figure 3-1A, another with a rotating anode, Figure 3-1B), located in Göttingen, and a dedicated nHT end-station (Salditt et al., 2015) (GINIX) installed at the P10/PETRAIII beamline, in Hamburg (Figure 3-1C).

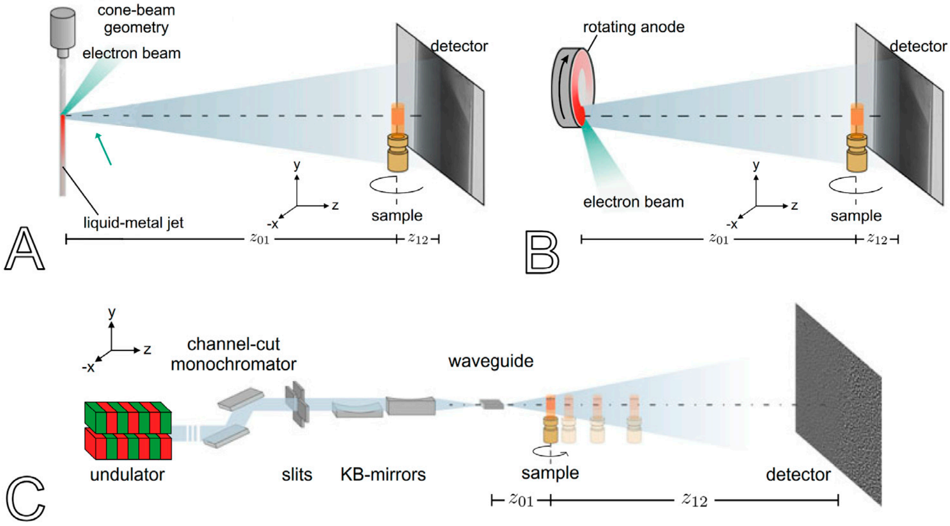

Figure 3-1: Schematics of the experimental setups used in Paper II and Paper III.
A – Laboratory setup with liquid-metal jet anode source, based on propagation-based phase-contrast in the direct contrast regime. **B –** Laboratory setup with rotating anode source, based on propagation-based phase-contrast in the direct contrast regime. **C –** Synchrotron end-station (GINIX), which employs nano-holotomography by acquiring different projections at different positions in the holographic regime. In Paper III, the end-station was also used in parallel-beam configuration, by forgoing the waveguide and illuminating the sample directly with the parallel radiation coming from the undulator. Figures adapted from (Salditt and Töpperwien, 2020) (open access CC BY 4.0).

The laboratory setups, which work with propagation-based phase-contrast, allowed to image the whole 1 mm wide samples with a ~1 µm effective voxel size (~ 8 h scan time per sample). Selected regions of interest were then scanned in the synchrotron based endstation, which through nHT allowed to image regions of 320x320x320 µm^3 with an effective voxel size of 176 nm (~ 3.5 h scan time). In a second beamtime (performed after the measurements presented in Paper II), the synchrotron endstation was also equipped with a parallel-beam configuration (Frohn et al., 2020), which enabled to measure the full samples with a 0.65 µm effective voxel size and a very fast scan time (around 1.5 minutes for a full scan). Phase retrieval, ring removal and tomographic reconstruction for all the setups were performed with reconstruction pipelines developed by Salditt's group (Lohse et al., 2020).

3.3 Summary of results

3.3.1 Myenteric plexus

The first results of the myenteric plexus analysis are presented in Paper II. In brief, the µCT measurements allowed to visualise the 3D network of ganglia and interconnecting nerve bundles, while the nHT scans presented sufficient contrast to follow and analyse the various cellular components of the myenteric ganglia, i.e. neurons and glial cells, the periganglional space and the smooth muscle cells.

A qualitative comparison between healthy and sick samples was performed with virtual histology by a pathologist, who could identify significant differences both in the overall structure of the network and in the cellular components of the myenteric ganglia (Figure 3-2A and 3-2B). Compared with state-of-the-art immunohistochemistry, however, x-ray virtual histology could not differentiate between cell types with similar shape but different function (Veress and Ohlsson, 2020) (Figure 3-2C). The necessity of extracting a 1-mm biopsy punch, coupled with the long scan time of the laboratory setups, was also seen as a further disadvantage of the method.

In the µCT scans, the neural tissue network could be segmented, enabling a quantitative evaluation of the neural tissue volume over total biopsy volume ratio, as well as an estimation of neural tissue thickness (Figure 3-2D and 3-2E).

A segmentation of the individual cells in the nHT scans was instead complicated by the low contrast of the very thin cell membranes. Promising results could be obtained with texture-based machine learning segmentation (using the free software ilastik (Berg et al., 2019)), but were ultimately not included in the paper as still not satisfactory (Figure 3-3).

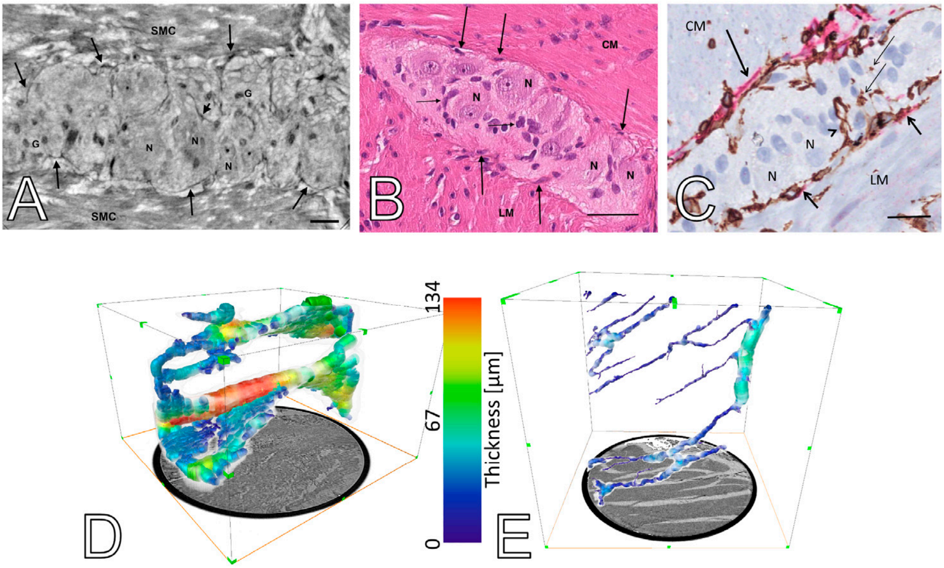

Figure 3-2: Comparison of x-ray virtual histology with state-of-the-art histology and immunohistostaining.
X-ray virtual histology acquired with nHT (**A**) is comparable to standard histology with haematoxylin and eosin staining (**B**) in the assessment of the cellular components of the myenteric ganglia. Aside from neurons and glial cells in the main “body” of the ganglion, small spindle-shaped cells are also visible along the contour of the ganglia (long arrows, in both A and B). Double immunohistochemical staining (**C**) can however differentiate the spindle-shaped cells between telocytes (stained in brown) and interstitial cells of Cajal (stained in red), which serve separate purposes. Even though x-ray virtual histology cannot provide this functional specificity, its advantage is providing three-dimensional information. This is especially visible when the neural tissue is segmented in the µCT scans, highlighting structural differences between healthy (**D**) and sick (**E**) individual which would require time-consuming serial sectioning to be assessed with standard histology. Scale bars in A, B, C: 25 µm; in D and E, the circular cross-section of the sample, shown at the bottom, has a diameter of 1 mm. Figures A, B, D and E adapted from Paper II; Figure C adapted from (Veress and Ohlsson, 2020) (CC BY 4.0).

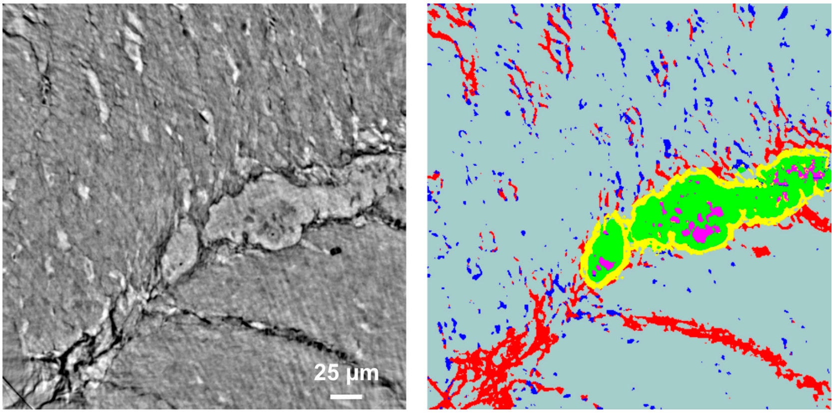

Figure 3-3: Segmentation attempts of the high-resolution nHT datasets.
The segmentation, achieved with texture-based interactive segmentation in ilastik, showed promise in distinguishing the darker features around the ganglia, as well as some of the cells inside them. However, it was not considered satisfactory enough, and has been for the moment abandoned.

Following Paper II, which was based on the comparison of just two individuals, a second beamtime was performed in order to include more samples. A paper about the new results is currently in preparation. Recent exploratory µCT scans of full-size biopsy blocks at the TOMCAT beamline of the Swiss Light Source (SLS), in Villigen, Switzerland, have also shown enough contrast to discriminate myenteric ganglia, which could enable the study of the 3D network in a much larger volume and a fraction of the time (Figure 3-4A).

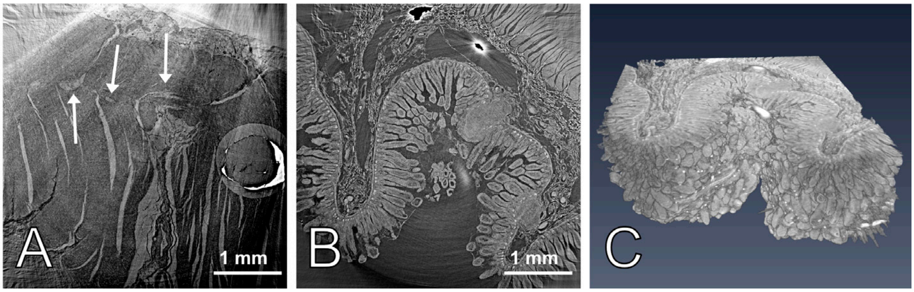

Figure 3-4: SRµCT of full-size biopsy blocks as future line of work.
A – Despite the strong artefacts due to the air-sample interface, the enteric neural tissue (arrows) shows enough contrast to be distinguished from the neighbouring muscles. This could potentially enable a segmentation of the neural tissue network in a much larger area when compared to Figures 3-2D and 3-2E. For direct size comparison, the hole left by a 1-mm wide biopsy punch taken on the sample is clearly visible on the right side of the image. **B –** Full-size SRµCT may also enable a better assessment of the submucosal plexus, potentially aiding in finding elusive submucosal ganglia, or as a way to assess the three-dimensional aspect of villi and crypts. **C –** Volume rendering of the sample shown in B; the villi are readily visible, and highly attenuating cells are visible on the surface.

3.3.2 Submucosal plexus

No ganglia could be distinguished by the pathologist in any of the scans of the submucosal plexus. It was impossible to determine whether this was due to a limitation in the density contrast offered by the techniques, or to a real absence of the ganglia in the biopsy punch. The submucosal ganglia have smaller size and a more irregular distribution when compared to the ones in the myenteric plexus, hence the chance that the punch might have missed them is very high. The same is valid for the thin submucosal nerves. Other structures of the small intestinal mucosa, such as villi and crypts with their different types of cells, could be easily identified in the µCT and nHT scans, but a qualitative comparison of their structure highlighted no difference between patients and controls. For these reasons, an analysis of the submucosal nervous system by means of x-ray tomography has been for the moment abandoned. Scanning the full-size biopsies may help in identifying the elusive submucosal ganglia, or in assessing the 3D structure of villi and crypts (Figures 3-4B and 3-4C).

3.3.3 Skin biopsies

The main results of the skin biopsy analysis are presented in Paper III. The lab-based µCT scans clearly showed the different layers of the epidermis, and could separate glands, hair follicles, and blood vessels from the connective tissue fibres of the dermis. In the parallel-beam measurements of the synchrotron setup, differences in the architecture of the dermal fibres were observed in some patients with gastrointestinal dysmotility compared with controls and other patients with dysmotility; however, it was impossible to differentiate between fibres, cellular elements and nerves. The same was unfortunately true for the nHT scans as well, although a suspect epidermal nerve fibre could be identified in one patient.

In conclusion, while well-suited for the evaluation of connective tissue, x-ray µCT and nHT were found still inferior to immunohistochemistry and electron microscopy in separating various cell types and identifying skin nerves. Possible improvements in this sense could be given by staining with contrast agent, as successfully demonstrated in a recently published nHT study of osmium-stained peripheral nerves (Dahlin et al., 2020).

4 Multimodal imaging of Mg-based biodegradable implants in bone

Du gust is megl che uan.
— Italian wise man

In this chapter we return to the topic of characterisation of biodegradable Mg-based implants for osseointegration, already introduced in Chapter 2, but with a shifted attention towards the elemental composition of the degradation by-products, which in this thesis work has been examined by using a combination of different techniques. A first part of the chapter will explain the medical motivation behind this interest, and the limits of current state-of-the-art techniques to investigate this topic. Subsequently, the novel methods employed in this thesis work will be detailed, using concepts already laid out in the Theory chapter. Lastly, the chapter will introduce Paper IV and Paper V, providing brief specific background for each of them and summarising their main results and conclusions.

4.1 Background

4.1.1 The toxicity problem and the importance of elemental distribution

As extensively described in Chapter 2, biodegradable Mg-based alloys are attracting a lot of interest as materials of choice for osseointegration devices, because of their potential to support the bone during healing and then dissolve into biocompatible by-products after full recovery (Virtanen, 2011).

It has also been already mentioned that several possible alloying elements are being investigated in search of the optimal Mg-alloy. When selecting a candidate alloying element, the main considerations are its strengthening ability, its influence on the corrosion behaviour and its toxicity. The SynchroLoad project detailed in Chapter 2 had the clear purpose of evaluating strengthening ability and influence on corrosion behaviour of Gd as an alloying element, but the potential toxicity aspect had been substantially neglected.

The toxicity of Gd, as well as that of other rare earth elements (REE), has been investigated in the past but remains controversial (Weng et al., 2021). While chelated Gd has been used in the medical field as contrast agent for magnetic resonance imaging for several decades already (Weinmann et al., 1984), multiple reports about its toxicity have emerged over the years (Broome et al., 2007, Ramalho et al., 2017). The most concerning issue linked with the use of Gd for osseintegrated devices could be the release over time of free Gd^{3+} ions, which have been shown to act as very efficient Ca^{2+} antagonists (Biagi and Enyeart, 1990), with especially negative effects on bone quality. While *in vitro* toxicity tests have shown a lower toxicity of Gd compared to other REE (Feyerabend et al., 2010), it is still unclear whether this would be reflected in the *in vivo* case as well (Weng et al., 2021).

The overall toxicity is most certainly affected by the behaviour of the alloying elements during implant degradation, which is however still poorly understood *in vivo*. A common expectation is that the excess material should be excreted from the body via normal bodily functions. In that case, eventual Gd^{3+} release would be a time-limited problem, if a problem at all. However, a recent study has evidenced accumulation of Gd in the main excretory organs (spleen, lungs, liver and kidneys) of rats after implantation of Mg-Gd pins for 12 weeks (Myrissa et al., 2017). Since Gd^{3+} is so similar to Ca^{2+}, one could expect an even higher accumulation of Gd into the bone surrounding the implant; in fact, Gd presence has been already revealed in the bone of human patients injected with Gd-based magnetic resonance contrast agents (Darrah et al., 2009). On the other hand, small-angle x-ray scattering, performed on some of the SynchroLoad samples themselves, has suggested instead a possible permanence of Gd at the implant site (Zeller-Plumhoff et al., 2020) even after 12 weeks of implantation. In this case, an eventual slow release of Gd^{3+} ions over time would clearly be concerning, as the Gd bulk would remain in place for a long time.

Given these disparate findings, the importance of techniques capable of providing information regarding the elemental composition of the corrosion by-products cannot be understated.

4.1.2 Available techniques and their limits

Some of the most common techniques used for direct elemental analysis are XRF and EDX, which, as briefly introduced in Chapter 1, are both based on inducing characteristic x-ray emission (i.e. fluorescence) from the sample. These techniques have already been extensively employed in the characterisation of biodegradable Mg-based implants in bone (Esmaily et al., 2017), for example to track Mg accumulation in the proximity of implants (Grunewald et al., 2016), or the migration of yttrium used as alloying material (Turyanskaya et al., 2016). Both of them have also shown capability of revealing Gd accumulation in mice (Delfino et al., 2019) and humans (Sanyal et al., 2011) following injection of Gd-based contrast agents. Nevertheless, a problem with these methods is that they are limited by the depth of penetration of the selected probe (as well as by the self-absorption of the emitted x-ray photons inside the medium); as such, they are normally regarded as surface techniques, and require sectioning of the sample in order to access the interface of interest. The degradation of Mg-based implants however is not homogeneous (Zeller-Plumhoff et al., 2018), hence the results of these 2D techniques will depend on the slicing plane and could end up missing the full picture. Moreover, since *ex vivo* samples are far more difficult and costlier to obtain compared to *in vitro* ones, it would be preferable to extract full information from them rather than studying only a few selected slices. While 3D fluorescence imaging is an existing technique, its use is still limited to a relatively small number of synchrotron facilities worldwide. Furthermore, it is typically used for smaller and softer samples; bone explants with metal implants would most probably prove to be too absorbing to be imaged successfully.

As already described in Chapter 2, the most common way to extend the analysis of Mg-based implants to 3D is x-ray µCT. The method however does not provide elemental decomposition: despite the fact that x-ray attenuation depends on the material's atomic number, this information alone is not enough to discriminate between the different elements, since density variations and element mixtures will influence the result. For that reason, even though SRµCT has shown enough density resolution to be able to appreciate attenuation variations within the corrosion layers (Galli et al., 2016), the method has only been used thus far to observe the degradation morphology in 3D and to estimate degradation rate by means of implant volume reduction over time, without any attempt at linking attenuation to composition (Zeller-Plumhoff et al., 2021b, Zeller-Plumhoff et al., 2018, Zeller-Plumhoff et al., 2021a, Krüger et al., 2021b, Krüger et al., 2021a). A few studies have explored k-edge subtraction SRµCT as a way to evaluate the distribution of REEs (Witte et al., 2006, Davenport et al., 2007) in Mg-RE-based implants, however the technique has not been extensively picked up for this sort of application yet, probably because of its relatively poor signal-to-noise ratio and the necessity to select the element to investigate *a priori*.

4.1.3 Overcoming the limitations

One possible solution to these limitations would be to combine SRµCT with 2D fluorescence techniques, in order to correlate patterns in x-ray attenuation with directly measured elemental compositions. While this requires some way of registering 2D datasets to 3D ones, which can be quite challenging depending on contrast differences and on mechanical deformations introduced when slicing the sample, the strong advantages are that both the techniques are already well established in the field and that the fluorescence map is a direct measurement of elemental composition, which is hence known exactly at least for one slice of the volume. This method has been explored in Paper IV, as will be detailed later when the two papers are presented.

A different approach to obtain elemental discrimination in 3D would be an indirect one, based on combining 3D datasets acquired with different contrast mechanisms, not necessarily directly representative of elemental composition, but functions of it. If the chosen contrast mechanisms have different response functions to the combination of elements contained in the material, comparing the response between the two sets could provide insights about the elemental composition. In this thesis work, an attempt at this approach was made by combining neutron and x-ray µCT. This method is the main highlight of Paper IV and Paper V, and as such will be further described in the next section.

4.2 Combining neutron and x-ray tomography

4.2.1 Overview

As anticipated in Chapter 1, neutrons interact with matter according to different mechanisms when compared to x-rays. Since they interact with atomic nuclei rather than atomic electrons, the interaction cross-section depends on the nuclear structure rather than the electronic structure of the material. As such, the contrast provided by neutron tomography is much different than the one associated to x-ray tomography, and the two techniques are often considered as complementary one to the other.

From a biological perspective, an interesting "feature" of using neutrons is the high attenuation provided by hydrogen, which, being part of water molecules, is obviously highly present in every living organism. While this could be crucial for biological applications of neutron imaging, and has been successfully exploited in experiments that tracked water uptake in plants (Tötzke et al., 2021), in practice the high water content in any kind of biological tissue has to date proven to be more problematic than helpful for the study of "wet" tissue, restricting the use of neutron tomography to mostly inorganic materials.

As far as inorganic materials are concerned, neutrons are widely used for their high penetration of metals when compared to x-rays, which is incredibly valuable in engineering applications and in quality control for the industry. Given their high sensitivity to light elements, such as the aforementioned hydrogen but also carbon and nitrogen, neutrons are also uniquely capable of providing high contrast for light materials, such as plastics, inside metallic casings, or to visualise the movement of fluids like oil or water in large metal objects.

The complementarity of neutron and x-ray tomography has been known since the first neutron imaging experiments, but the combination of the two methods has seen an increase in viability only in the last two decades, following constant improvements in the spatial resolution provided by neutron tomography setups (Kaestner et al., 2017, Lehmann et al., 2021). Successful bimodal neutron and x-ray tomography has been beneficial in the study of fuel cells (Ziesche et al., 2020), plant roots (Kaestner et al., 2017, Tötzke et al., 2021), porous construction materials (Stavropoulou et al., 2020) and archaeological samples (Mannes et al., 2015, Jacot-Guillarmod et al., 2019). A few very recent studies have also investigated the potential of combined x-ray and neutron imaging to avoid metal artefacts in the proximity of permanent stainless steel (Isaksson et al., 2017) and titanium (Törnquist et al., 2021) implants in bone.

4.2.2 Method

After acquiring tomographic scans of the same object with both neutrons and x-rays, a series of steps is necessary in order to facilitate the subsequent analysis.

The first crucial one is digital registration: since the two datasets are typically acquired with different experimental geometries and detectors with different pixel counts, they will need to be subjected to a series of digital transformations in order to be projected onto the same coordinate system. The optimal way to achieve this purpose, which is usually a combination of affine transformations (translations, rotations, scaling and sheer), can be determined with a wide variety of methods. In Paper IV and Paper V, a commercial software was used to this end (Amira, Thermo Fisher Scientific), however open-source toolkits tailored to bimodal x-ray and neutron imaging are also existing (Stamati et al., 2020).

Once the volumes have been projected onto a common coordinate system and resampled on the same grid, each voxel will be associated to an intensity value in the neutron domain and one in the x-ray domain. How to present the results then depends on the type of insights that are provided by the bimodal imaging. For some qualitative studies, as in Paper IV, it could be sufficient just to present the same slice in the two modalities, either side-by-side or overlapping the two with false colour maps or with checkerboard views. In other cases, more advanced analysis can be performed.

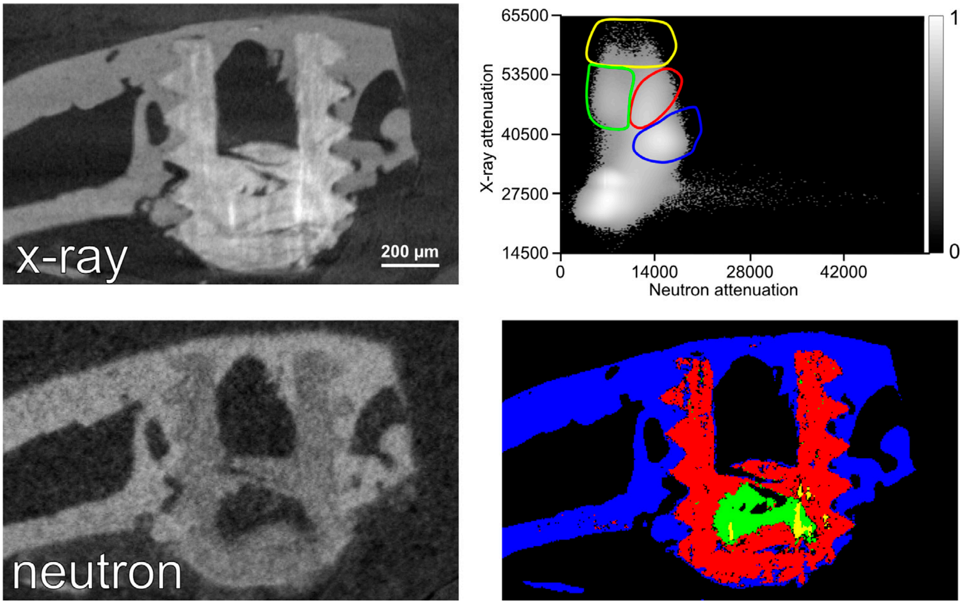

Figure 4-1: Bimodal analysis of x-ray µCT and neutron µCT by using the bivariate histogram.
After the volumes have been registered one onto the other, the same transversal section can be visualised in both the imaging modalities. In this case of a Mg-4Y-3RE implant, presented in Paper V, the section is quite different in the x-ray domain and the neutron domain. In particular, a “hole” appears in the central part of the screw in the neutron µCT, while the same area appear as homogeneous in the x-ray µCT scan. A bivariate histogram (top left) can be created by plotting x-ray attenuation vs neutron attenuation, and binning the axes in order to obtain density information in the form of intensity (represented by the false-colour map). Regions of interest can be manually selected in the bivariate histogram, and used to label the different phases, obtaining a segmentation (bottom right). In Paper V, an automatic clustering method has been explored, to eliminate the user bias that might be introduced by the manual selection.

An important step of the bimodal analysis is the bivariate histogram plot of the intensities (Figure 4-1). If one was to scatter plot all the voxels in a neutron intensity vs x-ray intensity graph, the cloud of points of the full 3D volume would usually be too dense to be interpreted. By discretising the intensity values into bins, and inserting each voxel into the bin it pertains to, the information is much easier to parse and density distributions, which correspond to the features contained within the images, are highlighted.

From a bivariate histogram, segmentation using the bimodal intensity values can be performed in a variety of methods, which are usually based on isolating the clusters of interest and associating different labels to the voxels pertaining to different clusters. The easiest method to achieve this purpose is manual selection of contours that contain the clusters of interest; this approach is fast, allows a quick visual check of which features correspond to which clusters and can be sufficient if a limited number of samples is being investigated. On the other hand, manual selection has limited reproducibility, so semi-automatic or fully automatic clustering methods could be preferable, especially with the prospect of imaging several samples that need to be compared among themselves. Since the topic of cluster analysis is crucial in several fields of science, ranging from computer vision to economy and marketing, a wide variety of clustering algorithms is already available and several toolboxes can be found which offer a relatively painless implementation, for example the Python-based Scikit-learn (Pedregosa et al., 2011). In the topic of bimodal neutron and x-ray imaging, Gaussian mixture methods have been proven a valid alternative for automatic clustering (Törnquist et al., 2021, Roubin et al., 2019). In Paper V, a segmentation approach based on the HDBSCAN clustering method (McInnes et al., 2017) has been attempted, with a reasonably good degree of success.

4.3 Multimodal imaging of Mg-based implants

The methods described in this Chapter have been used to investigate the elemental composition of corrosion by-products of biodegradable Mg-based implants in bone. First experiments were carried out on Mg-Gd samples from the SynchroLoad project, which have resulted in Paper IV. Follow-up studies have been performed on different Mg-based alloys (Mg-10Gd, Mg-4Y-3RE and Mg-2Ag) at a much longer healing time, and have been collected in Paper V.

4.3.1 Biodegradable Mg-Gd screws with 12 weeks healing time

As explained in the opening of this Chapter, the distribution of Gd following Mg-Gd implant corrosion is a matter of concern, since the toxicity of Gd is still controversial. For that reason, it was decided to investigate a few samples from the SynchroLoad project with techniques capable of showing elemental composition of the corrosion layer. Neutron tomography was particularly appealing for these samples, as Gd presents an extremely high attenuation coefficient for neutrons (Rauch and Waschkowski, 2003, Sears, 2006); as such, we believed that any migration of Gd into the bone surrounding the implant would be clearly visible in the neutron tomograms.

The samples were part of the *ex vivo* group which had been critical point dried following surgery (i.e. not the ones supposed to be used for the mechanical testing). After SRμCT, the dried samples were embedded in plastic resin and then cut in halves; one half had been used for histological sectioning, but the other half was available for other studies. EDX analysis was performed on 3 samples for each alloy (Mg-5Gd and Mg-10Gd), as well as on 3 samples with Ti screws for control; only the longest healing time point (12 weeks) was investigated, as the main goal of the analysis was to observe long-term behaviour of Gd.

Two dehydrated samples, one of each Mg-Gd alloy, were kept intact and not embedded in resin, in order to be scanned with neutron tomography. By using dehydrated samples (and avoiding the plastic resin, which is clearly rich in hydrogen and carbon), issues stemming from high hydrogen content in water could be avoided. Two non-implanted screws, one of each type, were also scanned as controls. The neutron experiments were carried out at the CONRAD-2 beamline of the (now decommissioned) BER-II research reactor in Berlin, Germany, with a 13 µm effective voxel size and around 13.5 h scanning time for a full tomography.

As part of the analysis, the EDX maps and the matching histological sections were identified in the corresponding SRµCT volumes using semi-automatic digital registration in Amira (Thermo Fisher Scientific). Similarly, the neutron µCT datasets were registered to their SRµCT counterparts.

All the results pointed to the conclusion that, at the investigated time point, the corrosion had interested only the Mg component of the alloys, while the Gd still remained at the implant site. This was observed directly in the 2D EDX maps and was extended to 3D with SRµCT and neutron µCT. XRF analysis of excretory organs that had presented Gd accumulation in previous similar studies (Myrissa et al., 2017) showed no Gd presence in our case, further reinforcing our conclusion.

X-ray attenuation patterns observed in the corrosion layer of the implants could be linked to the formation of sub-layers with different Ca and P elemental concentrations, revealed by EDX mapping. This was consistent with what is known about Mg corrosion *in vitro*, where Mg is progressively substituted by Ca and P (Ahmad Agha et al., 2016, Marco et al., 2017).

The neutron µCT scans, while crucial to assess the Gd distribution in 3D, did not provide much information on any of the other elements, since their attenuation was overpowered by the one of Gd. For that reason, in Paper IV the only comparison between x-ray and neutron tomograms was a qualitative one, showing the implant's appearance in the two contrast methods. While from a neutron point-of-view the screws looked perfectly intact, owing to the Gd permanence, SRµCT revealed corrosion layers similar to the ones observed in the samples compared with EDX. In particular, what was supposedly the non-corroded bulk of the implant, which EDX showed to be still rich in Mg, could be segmented in 3D from the SRµCT scans, revealing a much different aspect compared to the original shape of the screw.

4.3.2 Biodegradable Mg-based alloys with 9 months healing time

Since the study reported in Paper IV had shown that Gd was still at the implant site after 12 weeks, the question of potential toxicity was still open, as it was unclear whether Gd would remain there indefinitely, or if it would eventually disintegrate. The obvious follow up study was to explore longer healing times. Unfortunately, we would not have enough time to set up a completely new and dedicated study, as the time required for obtaining ethical permissions and performing animal experiments would be too long. However, leftover *ex vivo* samples were found from an older project, which had been the precursor of SynchroLoad. In this previous study, three different Mg-based alloys had been investigated with up to 9 months healing times in rabbits: an alloy based on Gd, Mg-10Gd, an alloy based on yttrium (Y) and a mixture of REE, Mg-4Y-3RE, and an alloy based on silver (Ag), Mg-2Ag. The purpose of that study had been to assess degradation performance of the alloys and evaluate the tissue response, but there had been no focus on the elemental composition of the degradation by-products.

For our study, we once again prioritised the longest healing point available (in this case, 9 months). We managed to scan 2 samples each of the Mg-4Y-3RE and Mg-2Ag alloys, and 1 sample of Mg-10Gd. All the samples were critical point dried, in the same way as in Paper IV. Non-implanted screws of the new alloys were also imaged, for reference.

All the scans were carried out at the NeXT-Grenoble beamline (Tengattini et al., 2020) of the ILL research reactor, in Grenoble, France. The beamline is equipped with an x-ray tomography setup inside of the hutch, so that bimodal tomography could be performed without having to move the sample, for an easier image registration (Figure 4-2).

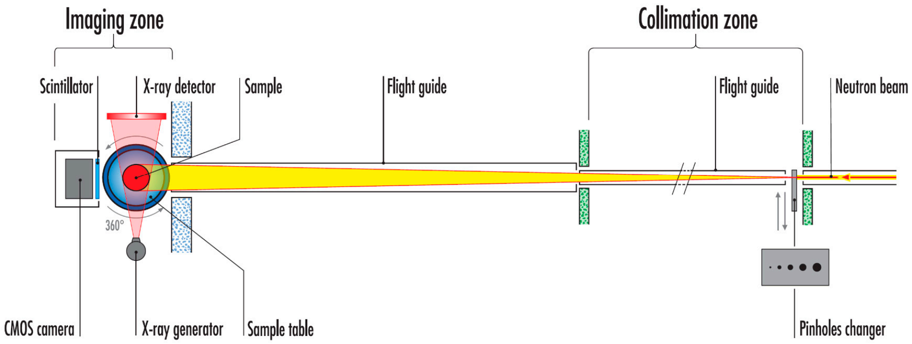

Figure 4-2: Schematic description of the imaging setup at NeXT-Grenoble.
The beamline employs a pinhole geometry (common in neutron imaging facilities), where the cold neutron beam is collimated by the combination of a small aperture (pinhole), with diameter D, and a long distance L (=10m) from the aperture to the sample position. In this way, the image quality depends on the ratio L/D, and several pinhole sizes can be used based on the chosen compromise between flux and spatial resolution, as detailed in (Tengattini et al., 2020). Once the beam gets to the imaging zone, the experimental geometry is the one of standard tomography, with a rotating sample stage and a scintillator-based detecting system. The beamline is also equipped with an x-ray µCT setup (in red), which enables bimodal imaging without having to move the sample between the two modalities. Figure reprinted from (Tengattini et al., 2020) (CC BY-NC-ND 4.0).

As a first result of Paper V, the Mg-10Gd sample revealed a behaviour very much similar to what observed in Paper IV. The implant looked still mostly intact, even after 9 months of healing time (albeit in rabbits, rather than in rats like in Paper IV). The longevity of this alloy came as a surprise, especially considering the high fragmentation observed in previous studies for what was nominally the same alloy after just 12 weeks in rats (Myrissa et al., 2017). As mentioned in Chapter 2, however, impurities play a significant role in corrosion behaviour, so a possible explanation for the discrepancy is that the older study had a lower alloy purity than the more recent experiments. Nevertheless, our study showed that Gd was still mostly present in the implant site even after 9 months, with possible implications on the long-term effects of the implant.

The most interesting findings of Paper V, however, involve the other two alloys. The absence of Gd allowed in this case to appreciate differences in neutron attenuation within the corrosion layers, and to compare them with the ones observed with x-ray tomography. By segmenting the images with clustering methods, evaluating the x-ray and neutron attenuation coefficients of the different phases, and comparing the results with XRF elemental maps acquired on samples from the same batch, it was possible to conclude that:

- For both Mg-4Y-3RE and Mg-2Ag, combining neutron and x-ray µCT allowed to discriminate in a volumetric way which parts of the implant are still not corroded from the ones that have interacted with the hydrogen in the body. X-ray µCT alone is not capable of discriminating this difference, which could have significant consequences in the correct estimation of corrosion rates of biodegradable implants by means of sole x-ray µCT, and might explain in part the discrepancy between corrosion rates measured *in vitro* (with direct methods) and the ones measured *ex vivo* (typically assessed with x-ray µCT) (Sanchez et al., 2015).
- In the case of Mg-2Ag, neutron and x-ray µCT, combined with XRF to guide the assessment, could also separate between different corrosion layers and corrosion by-products, potentially extending to 3D the surface results of XRF.

These findings support the validity of bimodal x-ray and neutron tomography as a uniquely promising technique for the evaluation of biodegradable implant corrosion, and further studies will surely be conducted in the future to investigate the potential of this method.

5 Conclusions and future directions

> *Alone we can do so little, together we can do so much.*
> — Helen Keller

This thesis, the first in the X-ray Phase Contrast Group of the Department, has aimed at exploring potential applications of state-of-the-art x-ray and neutron imaging techniques for the study of biomedical samples, with the hope of providing examples that could promote the techniques within the medical community and encourage future collaborations between medicine, natural science and engineering.

Two main lines of work have been detailed, one focused on the evaluation of corrosion processes of Mg-based biodegradable implants for osteosynthesis, the other dedicated to assessment of neuropathy in human gastroenteric dysmotility.

For the first line of work, the main conclusions have been:

- SRµCT can in principle be employed to assess the mechanical properties of the bone-implant interface, but particular attention needs to be paid to the radiation dose deposited on the sample, and the mechanical loading geometry should be accurately considered in the planning step of the experiments (Paper I).
- In the case of biodegradable implants based on Mg-Gd alloys, a combination of x-ray µCT, neutron µCT and fluorescence mapping methods has revealed Gd permanence at the implant site after 12 weeks (Paper IV) and even after 9 months of healing time (Paper V). This could have serious implications on the long-term effects of this type of implants, and further evaluations on the behaviour of Gd over time will be necessary.
- When Mg-based biodegradable implants without Gd were considered, combining x-ray and neutron µCT, with the support of µXRF, has enabled to discriminate different corrosion by-products in a way which was not possible with x-ray µCT alone (Paper V). This could potentially shed light on the discrepancy reported in literature between *in vitro* and *in vivo* degradation rates (Sanchez et al., 2015), as the latter are commonly assessed in a volumetric way by means of x-ray µCT.

The second line of work has led to the following conclusions:

- Virtual histology with x-ray phase-contrast µCT could assess the 3D structure of the unstained myenteric nervous system, showing qualitative and potentially quantitative differences between controls and patients affected by gastrointestinal dysmotility. High-resolution nHT also presented sufficient contrast to follow and analyse the various cellular components of the myenteric ganglia, revealing once again variation in health and sickness (Paper II). The method however couldn't distinguish between cells of similar shape but different function, resulting in this inferior to state-of-the-art immunohistochemistry.
- X-ray phase-contrast µCT and nHT struggled to visualise peripheral nerves in unstained skin biopsies; the method cannot hence be used yet as an alternative to full-thickness biopsies in the assessment of neuropathy of the ENS. Nevertheless, synchrotron-based techniques could identify structural changes in the connective tissue of some patients when compared to controls and other patients.

While this exploratory work has been reasonably successful and encouraging, future improvements can be envisioned in all the different topics.

In the mechanical loading tests of biodegradable implants, based on the assessments presented in Paper I, measurements with lower dose and "push-out" geometry of all the remaining samples have been recently performed, and data analysis is currently being carried out by the group in Hamburg. The "dose problem" is however still significant and limits the number of sampling points for the loading curve without compromising too much the image quality, which is reportedly very important for digital volume correlation techniques (Grassi and Isaksson, 2015, Dall'Ara et al., 2017). Future developments in detector technology and in reconstruction techniques may help reducing the dose even further; other possible ways worth exploring could also be the use of higher energies, or phase-contrast methods. For the application of the technique to biodegradable implants, however, particular attention will always need to be paid to the geometry of the mechanical testing, as highlighted in our experience.

Regarding the topic of x-ray virtual histology, the method has proven its worth in Papers II and III, and also in several of the other papers produced during this doctoral work but not included in this thesis. The response of every medical doctor involved has been one of enthusiasm and fascination, which will hopefully be contagious in the community. Even though synchrotron access is quite limited and requires time and planning, characteristics that poorly match the needs of clinical applications, promising results could be achieved with state-of-the-art laboratory setups as well. Future improvements in compact sources and detecting systems, and possibly the development of commercial systems of easier use, could enable the use of x-ray virtual histology for diagnostic purposes, as hinted in Papers II and III for the determination of enteric neuropathy or changes in the connective tissue structure. To further establish the value of the technique over traditional histology, other aspects of future investigation could be the use of contrast agents specifically tailored for x-ray imaging, a topic which has been relatively ignored until recently, but is showing great promise (Busse et al., 2018, Müller et al., 2018), and the use of more advanced segmentation methods. This last point in particular has been one of the main bottlenecks for several of the collaborations in this work: the constant improvement of imaging techniques will enable access to data of increasing complexity; as such, it will be crucial to involve in the collaborations experts in image analysis as well.

Finally, the topic of bimodal x-ray and neutron imaging is still in its infancy, especially applied to biomedical samples. As we illustrated in Papers IV and V, the technique would appear to be a perfect match for the study of biodegradable implants, but further exploration is still necessary. Future directions in this sense could be the extension of our measurements to more time-points, in order to obtain corrosion rates to compare to standard *in vitro* and *ex vivo* ones. Other types of biodegradable metal alloys, not necessarily based on Mg, could also be well suited to this technique. As far as method improvements are concerned, it would certainly be interesting to explore monochromatic x-ray and neutron imaging, and possibly neutron Bragg edge imaging, a technique which has already shown significant potential in discriminating between different phases in building materials or archaeological artefacts (Woracek et al., 2018).

In conclusion, the doctoral work presented in this thesis has hopefully laid some early steps that will lead to a broader use of advanced x-ray and neutron imaging techniques for biomedical applications in the Lund and Malmö area. This region is set to become a centre of advanced physics in the near future: after a relatively slow start, MAX IV is starting to gain steam and a medical imaging beamline will hopefully gather funding soon; the European Spallation Source (ESS) is also currently scheduled to open for user activity in 2023, with a neutron imaging beamline, equipped with x-ray µCT as well, already planned. A personal hope is that this thesis will inspire future doctoral students in the fields of medical radiation physics and medicine to use and explore these fantastic instruments and techniques.

6 Acknowledgements

So long, and thanks for all the fish.
- The dolphins (The Hitchhiker's Guide to the Galaxy series, by Douglas Adams)

Throughout this five-year-long journey and the writing of this dissertation I have received a great deal of support and assistance by numerous people. In particular, I would like to express my deepest gratitude to:

My main supervisor, Martin, for always being at my side and reassuring me in all the moments of self-doubt. Thank you for involving me in so many interesting and stimulating project, and always giving me the freedom to pursuit what I found most intriguing. You have contributed to making me the researcher I am today, helping me to navigate in the confusing world of academia and research.

My co-supervisors, Ann and Rajmund, for providing valuable support and guidance whenever I needed it. Special thanks to Rajmund for hosting me at MAX IV when I was temporarily "orphaned" during Martin's parental leave, and for constantly trying to organise hackathons for image analysis problems.

All the unofficial co-supervisors who have guided me in the medical aspects of the various sub-projects. In alphabetical order, thank you Béla, Bodil, Karin and Silvia. Your immense knowledge and enthusiasm in your respective fields have been incredibly inspiring, none of this would have been possible without your help and guidance.

All my co-authors, working with you has been a blast and I look forward to doing it again in the future. Special thanks to all the ones who have shared with me the bliss and pain of "beamtime funtime": Christian N, Christian W, Ida and Oscar at TOMCAT; Jasper, Mariam and Marina at GINIX; Berit, Diana, Florian and Julian at IBL. Completely forgoing sleep has been much more enjoyable in your company.

My colleagues in the X-ray Phase Contrast Group, Nathaly and Till; the group would (literally) not exist without you. Thank you for the company and the laughs at lunchtime, and for the interesting discussions during our group meetings. Special thanks to Till for the help at several beamtimes, and for the constant supply of (non-agar-based) cakes.

All the other colleagues in the Medical Radiation Physics department. Special mention to the fellow PhD students who shared with me supervision duties of the laboratory course in ionising radiations, both the “old ones” (Filip and Anneli) and those who still have to “pay their due” (Philip and Lovisa). My deepest thanks also to Ronnie, for the infinite patience and kindness in explaining and reminding me all the administrative procedures of the department; you have been the best Director of Postgraduate Studies that I could have possibly hoped for.

All the friends in Malmö and Lund, who have supported me each in their own way. Thank you Hanna, Maïté and Marie for the dinners, coffees and board game sessions; I hope to see you even more often now that the pandemic is relenting a bit.

Infine un grazie speciale, e in italiano, a tutti gli amici e parenti che nonostante la distanza fisica mi sono sempre rimasti vicini e mi hanno scaldato il cuore in questi anni di freddo svedese:

Grazie agli amici storici, Luca e Sergio; anche se non ci sentiamo spesso, ogni volta è come se il tempo non fosse passato per niente. Grazie per gli incoraggiamenti ed i pensieri continui.

Grazie agli amici dell’Università, i vostri messaggi semi-seri su Whatsapp e le chiamate di gruppo durante la pandemia mi hanno veramente aiutato a tirare avanti. Un ringraziamento speciale ai soliti noti, Cosimo, Gabriele e Paolo: le serate passate ad ammazzare orde di alieni a cavallo di sidecar esplosivi hanno contribuito a tenermi ancorato per terra nonostante il delirio quotidiano.

Un ringraziamento a tutta la famiglia; ritornare in patria per le feste è sempre stata occasione di grande gioia e un ottimo modo di “ricaricarmi” di energia in vostra compagnia.

Un grazie speciale ovviamente alla mamma, il babbo e a Fede, per il vostro continuo supporto e amore incondizionato; in questi ultimi tempi, bloccato qui dalla pandemia, mi siete veramente mancati un sacco.

Infine, il più grande ringraziamento di tutti va alla mia Justine. Ritrovarti in casa al ritorno dall’ufficio è stata la migliore parte delle mie giornate negli ultimi tre anni. Grazie per il tuo supporto e il tuo amore, e per esserti presa cura di me soprattutto in queste ultime settimane di delirio più completo. Ti amo tanto.

7 References

ADLER, J., KOHR, H. & ÖKTEM, O. 2017. Operator Discretization Library (ODL).

AHMAD AGHA, N., WILLUMEIT-ROMER, R., LAIPPLE, D., LUTHRINGER, B. & FEYERABEND, F. 2016. The Degradation Interface of Magnesium Based Alloys in Direct Contact with Human Primary Osteoblast Cells. *PLoS One,* 11**,** e0157874.

ALBERS, J., PACILÉ, S., MARKUS, M. A., WIART, M., VANDE VELDE, G., TROMBA, G. & DULLIN, C. 2018. X-ray-Based 3D Virtual Histology—Adding the Next Dimension to Histological Analysis. *Molecular Imaging and Biology,* 20**,** 732-741.

ALS-NIELSEN, J. & MCMORROW, D. 2011. Elements of Modern X-ray Physics: Second Edition. *Elements of Modern X-ray Physics: Second Edition.*

AMMANN, E. & KUTSCHERA, W. 1997. X-ray tubes - Continuous innovative technology. *British Journal of Radiology.* The British Institute of Radiology.

BANHART, J. 2008. *Advanced tomographic methods in materials research and engineering*, Oxford University Press.

BARTH, H. D., LAUNEY, M. E., MACDOWELL, A. A., AGER, J. W. & RITCHIE, R. O. 2010. On the effect of X-ray irradiation on the deformation and fracture behavior of human cortical bone. *Bone,* 46**,** 1475-1485.

BARTH, H. D., ZIMMERMANN, E. A., SCHAIBLE, E., TANG, S. Y., ALLISTON, T. & RITCHIE, R. O. 2011. Characterization of the effects of x-ray irradiation on the hierarchical structure and mechanical properties of human cortical bone. *Biomaterials,* 32**,** 8892-8904.

BASKO-PLLUSKA, J. L., THYSSEN, J. P. & SCHALOCK, P. C. 2011. Cutaneous and systemic hypersensitivity reactions to metallic implants. *Dermatitis,* 22**,** 65-79.

BERG, S., KUTRA, D., KROEGER, T., STRAEHLE, C. N., KAUSLER, B. X., HAUBOLD, C., SCHIEGG, M., ALES, J., BEIER, T., RUDY, M., EREN, K., CERVANTES, J. I., XU, B., BEUTTENMUELLER, F., WOLNY, A., ZHANG, C., KOETHE, U., HAMPRECHT, F. A. & KRESHUK, A. 2019. ilastik: interactive machine learning for (bio)image analysis. *Nature Methods,* 16**,** 1226-1232.

BIAGI, B. A. & ENYEART, J. J. 1990. Gadolinium blocks low- and high-threshold calcium currents in pituitary cells. *Am J Physiol,* 259**,** C515-20.

BIGURI, A., DOSANJH, M., HANCOCK, S. & SOLEIMANI, M. 2016. TIGRE: a MATLAB-GPU toolbox for CBCT image reconstruction. *Biomedical Physics & Engineering Express,* 2**,** 055010.

BRAVIN, A., COAN, P. & SUORTTI, P. 2012. X-ray phase-contrast imaging: from pre-clinical applications towards clinics. *Physics in Medicine & Biology,* 58**,** R1.

BROOME, D. R., GIRGUIS, M. S., BARON, P. W., COTTRELL, A. C., KJELLIN, I. & KIRK, G. A. 2007. Gadodiamide-associated nephrogenic systemic fibrosis: why radiologists should be concerned. *AJR Am J Roentgenol,* 188**,** 586-92.

BUADES, A., COLL, B. & MOREL, J. A non-local algorithm for image denoising. 2005 IEEE Computer Society Conference on Computer Vision and Pattern Recognition (CVPR'05), 20-25 June 2005 2005. 60-65 vol. 2.

BUSSE, M., MÜLLER, M., KIMM, M. A., FERSTL, S., ALLNER, S., ACHTERHOLD, K., HERZEN, J. & PFEIFFER, F. 2018. Three-dimensional virtual histology enabled through cytoplasm-specific X-ray stain for microscopic and nanoscopic computed tomography. *Proceedings of the National Academy of Sciences,* 115**,** 2293-2298.

CASTELLANI, C., LINDTNER, R. A., HAUSBRANDT, P., TSCHEGG, E., STANZL-TSCHEGG, S. E., ZANONI, G., BECK, S. & WEINBERG, A.-M. 2011. Bone–implant interface strength and osseointegration: Biodegradable magnesium alloy versus standard titanium control. *Acta Biomaterialia,* 7**,** 432-440.

CASTIGLIONI, S., CAZZANIGA, A., ALBISETTI, W. & MAIER, J. 2013. Magnesium and Osteoporosis: Current State of Knowledge and Future Research Directions. *Nutrients,* 5**,** 3022-3033.

CHEN, Y., XU, Z., SMITH, C. & SANKAR, J. 2014. Recent advances on the development of magnesium alloys for biodegradable implants. *Acta Biomaterialia,* 10**,** 4561-4573.

CLOETENS, P., LUDWIG, W., BARUCHEL, J., VAN DYCK, D., VAN LANDUYT, J., GUIGAY, J. P. & SCHLENKER, M. 1999. Holotomography: Quantitative phase tomography with micrometer resolution using hard synchrotron radiation x rays. *Applied Physics Letters,* 75**,** 2912-2914.

COBINE, C. A., HENNIG, G. W., KURAHASHI, M., SANDERS, K. M., WARD, S. M. & KEEF, K. D. 2011. Relationship between interstitial cells of Cajal, fibroblast-like cells and inhibitory motor nerves in the internal anal sphincter. *Cell Tissue Res,* 344**,** 17-30.

CURREY, J. D., FOREMAN, J., LAKETI, I., MITCHELL, J., PEGG, D. E. & REILLY, G. C. 1997. Effects of ionizing radiation on the mechanical properties of human bone. *Journal of Orthopaedic Research,* 15**,** 111-117.

DAHLIN, L. B., RIX, K. R., DAHL, V. A., DAHL, A. B., JENSEN, J. N., CLOETENS, P., PACUREANU, A., MOHSENI, S., THOMSEN, N. O. B. & BECH, M. 2020. Three-dimensional architecture of human diabetic peripheral nerves revealed by X-ray phase contrast holographic nanotomography. *Scientific Reports,* 10.

DALL'ARA, E., PEÑA-FERNÁNDEZ, M., PALANCA, M., GIORGI, M., CRISTOFOLINI, L. & TOZZI, G. 2017. Precision of Digital Volume Correlation Approaches for Strain Analysis in Bone Imaged with Micro-Computed Tomography at Different Dimensional Levels. *Frontiers in Materials,* 4.

DARRAH, T. H., PRUTSMAN-PFEIFFER, J. J., POREDA, R. J., ELLEN CAMPBELL, M., HAUSCHKA, P. V. & HANNIGAN, R. E. 2009. Incorporation of excess gadolinium into human bone from medical contrast agents. *Metallomics,* 1**,** 479-88.

DAVENPORT, A. J., PADOVANI, C., CONNOLLY, B. J., STEVENS, N. P. C., BEALE, T. A. W., GROSO, A. & STAMPANONI, M. 2007. Synchrotron X-Ray Microtomography Study of the Role of Y in Corrosion of Magnesium Alloy WE43. *Electrochemical and Solid-State Letters,* 10**,** C5.

DE WITTE, Y., BOONE, M., VLASSENBROECK, J., DIERICK, M. & VAN HOOREBEKE, L. 2009. Bronnikov-aided correction for x-ray computed tomography. *J Opt Soc Am A Opt Image Sci Vis,* 26**,** 890-4.

DELFINO, R., BIASOTTO, M., CANDIDO, R., ALTISSIMO, M., STEBEL, M., SALOME, M., VAN ELTEREN, J. T., VOGEL MIKUS, K., ZENNARO, C., SALA, M., ADDOBBATI, R., TROMBA, G. & PASCOLO, L. 2019. Gadolinium tissue deposition in the periodontal ligament of mice with reduced renal function exposed to Gd-based contrast agents. *Toxicol Lett,* 301**,** 157-167.

DZIUBA, D., MEYER-LINDENBERG, A., SEITZ, J. M., WAIZY, H., ANGRISANI, N. & REIFENRATH, J. 2013. Long-term in vivo degradation behaviour and biocompatibility of the magnesium alloy ZEK100 for use as a biodegradable bone implant. *Acta Biomaterialia,* 9**,** 8548-8560.

ECKERMANN, M., FROHN, J., REICHARDT, M., OSTERHOFF, M., SPRUNG, M., WESTERMEIER, F., TZANKOV, A., WERLEIN, C., KÜHNEL, M., JONIGK, D. & SALDITT, T. 2020. 3D virtual pathohistology of lung tissue from Covid-19 patients based on phase contrast X-ray tomography. *eLife,* 9.

EKMAN, L., THRAINSDOTTIR, S., ENGLUND, E., THOMSEN, N., ROSÉN, I., HAZER ROSBERG, D. B., PETERSSON, J., ERIKSSON, K. F. & DAHLIN, L. B. 2020. Evaluation of small nerve fiber dysfunction in type 2 diabetes. *Acta Neurol Scand,* 141**,** 38-46.

ESMAILY, M., SVENSSON, J. E., FAJARDO, S., BIRBILIS, N., FRANKEL, G. S., VIRTANEN, S., ARRABAL, R., THOMAS, S. & JOHANSSON, L. G. 2017. Fundamentals and advances in magnesium alloy corrosion. *Progress in Materials Science,* 89**,** 92-193.

FELDKAMP, L. A., DAVIS, L. C. & KRESS, J. W. 1984. Practical cone-beam algorithm. *Journal of the Optical Society of America A,* 1**,** 612.

FEYERABEND, F., FISCHER, J., HOLTZ, J., WITTE, F., WILLUMEIT, R., DRÜCKER, H., VOGT, C. & HORT, N. 2010. Evaluation of short-term effects of rare earth and other elements used in magnesium alloys on primary cells and cell lines☆. *Acta Biomaterialia,* 6**,** 1834-1842.

FRANGI, A. F., NIESSEN, W. J., VINCKEN, K. L. & VIERGEVER, M. A. 1998. Multiscale vessel enhancement filtering. Springer, Berlin, Heidelberg.

FROHN, J., PINKERT-LEETSCH, D., MISSBACH-GÜNTNER, J., REICHARDT, M., OSTERHOFF, M., ALVES, F. & SALDITT, T. 2020. 3D virtual histology of human pancreatic tissue by multiscale phase-contrast X-ray tomography. *Journal of Synchrotron Radiation,* 27**,** 1707-1719.

FROST, E. B. 1896. Experiments on the X-rays. *Science,* 3**,** 235-236.

FURNESS, J. B., CALLAGHAN, B. P., RIVERA, L. R. & CHO, H. J. 2014. The enteric nervous system and gastrointestinal innervation: integrated local and central control. *Adv Exp Med Biol,* 817**,** 39-71.

GALLI, S. 2016. *On magnesium-containing implants for bone applications.* Malmö University, Faculty of Odontology.

GALLI, S., HAMMEL, J. U., HERZEN, J., DAMM, T., JIMBO, R., BECKMANN, F., WENNERBERG, A. & WILLUMEIT-RÖMER, R. Evaluation of the degradation behavior of resorbable metal implants for in vivo osteosynthesis by synchrotron radiation based x-ray tomography and histology. Developments in X-Ray Tomography X, 2016 2016. International Society for Optics and Photonics.

GATOPOULOU, A., PAPANAS, N. & MALTEZOS, E. 2012. Diabetic gastrointestinal autonomic neuropathy: Current status and new achievements for everyday clinical practice. *European Journal of Internal Medicine,* 23**,** 499-505.

GONZALEZ, R. C. & WOODS, R. E. R. E. 2008. Digital image processing. 954.

GRAHAM, K. D., LÓPEZ, S. H., SENGUPTA, R., SHENOY, A., SCHNEIDER, S., WRIGHT, C. M., FELDMAN, M., FURTH, E., VALDIVIESO, F., LEMKE, A., WILKINS, B. J., NAJI, A., DOOLIN, E. J., HOWARD, M. J. & HEUCKEROTH, R. O. 2020. Robust, 3-Dimensional Visualization of Human Colon Enteric Nervous System Without Tissue Sectioning. *Gastroenterology,* 158**,** 2221-2235.e5.

GRASSI, L. & ISAKSSON, H. 2015. Extracting accurate strain measurements in bone mechanics: A critical review of current methods. *Journal of the Mechanical Behavior of Biomedical Materials,* 50**,** 43-54.

GROVER, M., BERNARD, C. E., PASRICHA, P. J., PARKMAN, H. P., ABELL, T. L., NGUYEN, L. A., SNAPE, W., SHEN, K. R., SARR, M., SWAIN, J., KENDRICK, M., GIBBONS, S., ORDOG, T. & FARRUGIA, G. 2012. Platelet-derived growth factor receptor alpha (PDGFRalpha)-expressing "fibroblast-like cells" in diabetic and idiopathic gastroparesis of humans. *Neurogastroenterol Motil,* 24**,** 844-52.

GRUNER, S. M., TATE, M. W. & EIKENBERRY, E. F. 2002. Charge-coupled device area x-ray detectors. *Review of Scientific Instruments,* 73**,** 2815-2842.

GRUNEWALD, T. A., RENNHOFER, H., HESSE, B., BURGHAMMER, M., STANZL-TSCHEGG, S. E., COTTE, M., LOFFLER, J. F., WEINBERG, A. M. & LICHTENEGGER, H. C. 2016. Magnesium from bioresorbable implants: Distribution and impact on the nano- and mineral structure of bone. *Biomaterials,* 76**,** 250-60.

GURSOY, D., DE CARLO, F., XIAO, X. & JACOBSEN, C. 2014. TomoPy: a framework for the analysis of synchrotron tomographic data. *J Synchrotron Radiat,* 21**,** 1188-93.

HORN, B. K. & SCHUNCK, B. G. 1981. Determining optical flow. *Artificial intelligence,* 17**,** 185-203.

HOUNSFIELD, G. N. 1973. Computerized transverse axial scanning (tomography): Part 1. Description of system. *The British Journal of Radiology,* 46**,** 1016-1022.

HUANG, J., LI, X. & GUO, Z. X. 2020. 3 - Biomechanical and biochemical compatibility in innovative biomaterials. *In:* BOUTRAND, J. P. (ed.) *Biocompatibility and Performance of Medical Devices (Second Edition).* Woodhead Publishing.

ISAKSSON, H., LE CANN, S., PERDIKOURI, C., TURUNEN, M. J., KAESTNER, A., TÄGIL, M., HALL, S. A. & TUDISCO, E. 2017. Neutron tomographic imaging of bone-implant interface: Comparison with X-ray tomography. *Bone,* 103**,** 295-301.

JACOT-GUILLARMOD, M., SCHMIDT-OTT, K., MANNES, D., KAESTNER, A., LEHMANN, E. & GERVAIS, C. 2019. Multi-modal tomography to assess dechlorination treatments of iron-based archaeological artifacts. *Herit Sci,* 7**,** 29.

JAHNEN-DECHENT, W. & KETTELER, M. 2012. Magnesium basics. *Clinical Kidney Journal,* 5**,** i3-i14.

KAESTNER, A. P., HOVIND, J., BOILLAT, P., MUEHLEBACH, C., CARMINATI, C., ZAREBANADKOUKI, M. & LEHMANN, E. H. 2017. Bimodal Imaging at ICON Using Neutrons and X-rays. *Physics Procedia,* 88**,** 314-321.

KAK, A. C. & SLANEY, M. 2011. Principles of Computerized Tomographic Imaging. *Principles of Computerized Tomographic Imaging***,** 327.

KARDJILOV, N., LEHMANN, E., STROBL, M., WORACEK, R. & MANKE, I. 2017. Neutron Imaging. *In:* KARDJILOV, N. & FESTA, G. (eds.) *Neutron Methods for Archaeology and Cultural Heritage.* Cham: Springer International Publishing.

KELLER, J., BASSOTTI, G., CLARKE, J., DINNING, P., FOX, M., GROVER, M., HELLSTRÖM, P. M., KE, M., LAYER, P., MALAGELADA, C., PARKMAN, H. P., SCOTT, S. M., TACK, J., SIMREN, M., TÖRNBLOM, H. & CAMILLERI, M. 2018. Advances in the diagnosis and classification of gastric and intestinal motility disorders. *Nature Reviews Gastroenterology & Hepatology,* 15**,** 291-308.

KHIMCHENKO, A., BIKIS, C., PACUREANU, A., HIEBER, S. E., THALMANN, P., DEYHLE, H., SCHWEIGHAUSER, G., HENCH, J., FRANK, S., MÜLLER-GERBL, M., SCHULZ, G., CLOETENS, P. & MÜLLER, B. 2018. Hard X-Ray Nanoholotomography: Large-Scale, Label-Free, 3D Neuroimaging beyond Optical Limit. *Advanced Science,* 5**,** 1700694.

KHIMCHENKO, A., DEYHLE, H., SCHULZ, G., SCHWEIGHAUSER, G., HENCH, J., CHICHEROVA, N., BIKIS, C., HIEBER, S. E. & MÜLLER, B. 2016. Extending two-dimensional histology into the third dimension through conventional micro computed tomography. *NeuroImage,* 139**,** 26-36.

KIKINIS, R., PIEPER, S. D. & VOSBURGH, K. G. 2014. 3D Slicer: A Platform for Subject-Specific Image Analysis, Visualization, and Clinical Support. *Intraoperative Imaging and Image-Guided Therapy.* New York, NY: Springer New York.

KIRKLAND, N. T. 2012. Magnesium biomaterials: past, present and future. *Corrosion Engineering, Science and Technology,* 47**,** 322-328.

KIRZ, J. & JACOBSEN, C. 2009. The history and future of X-ray microscopy. *Journal of Physics: Conference Series,* 186**,** 012001.

KOCH, A., RAVEN, C., SPANNE, P. & SNIGIREV, A. 1998. X-ray imaging with submicrometer resolution employing transparent luminescent screens. *Journal of the Optical Society of America A,* 15**,** 1940.

KRÜGER, D., GALLI, S., ZELLER-PLUMHOFF, B., WIELAND, D. C. F., PERUZZI, N., WIESE, B., HEUSER, P., MOOSMANN, J., WENNERBERG, A. & WILLUMEIT-RÖMER, R. 2021a. High-resolution ex vivo analysis of the degradation and osseointegration of Mg-xGd implant screws in 3D. *Bioactive Materials,* In press.

KRÜGER, D., ZELLER-PLUMHOFF, B., WIESE, B., YI, S., ZUBER, M., WIELAND, D. C. F., MOOSMANN, J. & WILLUMEIT-RÖMER, R. 2021b. Assessing the microstructure and in vitro degradation behavior of Mg-xGd screw implants using µCT. *Journal of Magnesium and Alloys*.

KUAN, A. T., PHELPS, J. S., THOMAS, L. A., NGUYEN, T. M., HAN, J., CHEN, C.-L., AZEVEDO, A. W., TUTHILL, J. C., FUNKE, J., CLOETENS, P., PACUREANU, A. & LEE, W.-C. A. 2020. Dense neuronal reconstruction through X-ray holographic nano-tomography. *Nature Neuroscience,* 23**,** 1637-1643.

LACY, B. E., MEARIN, F., CHANG, L., CHEY, W. D., LEMBO, A. J., SIMREN, M. & SPILLER, R. 2016. Bowel Disorders. *Gastroenterology,* 150**,** 1393-1407.e5.

LARSSON, D. H., LUNDSTROM, U., WESTERMARK, U. K., ARSENIAN HENRIKSSON, M., BURVALL, A. & HERTZ, H. M. 2013. First application of liquid-metal-jet sources for small-animal imaging: high-resolution CT and phase-contrast tumor demarcation. *Med Phys,* 40**,** 021909.

LEHMANN, E. H., MANNES, D., KAESTNER, A. P., HOVIND, J., TRTIK, P. & STROBL, M. 2021. The XTRA Option at the NEUTRA Facility—More Than 10 Years of Bi-Modal Neutron and X-ray Imaging at PSI. *Applied Sciences,* 11**,** 3825.

LEVIN, B. D. A., JIANG, Y., PADGETT, E., WALDON, S., QUAMMEN, C., HARRIS, C., AYACHIT, U., HANWELL, M., ERCIUS, P., MULLER, D. A. & HOVDEN, R. 2018. Tutorial on the Visualization of Volumetric Data Using tomviz. *Microscopy Today,* 26**,** 12-17.

LOHSE, L. M., ROBISCH, A.-L., TÖPPERWIEN, M., MARETZKE, S., KRENKEL, M., HAGEMANN, J. & SALDITT, T. 2020. A phase-retrieval toolbox for X-ray holography and tomography. *Journal of Synchrotron Radiation,* 27**,** 852-859.

LØSETH, S., STÅLBERG, E. V., LINDAL, S., OLSEN, E., JORDE, R. & MELLGREN, S. I. 2016. Small and large fiber neuropathy in those with type 1 and type 2 diabetes: a 5-year follow-up study. *J Peripher Nerv Syst,* 21**,** 15-21.

LOVRIC, G., VOGIATZIS OIKONOMIDIS, I., MOKSO, R., STAMPANONI, M., ROTH-KLEINER, M. & SCHITTNY, J. C. 2017. Automated computer-assisted quantitative analysis of intact murine lungs at the alveolar scale. *PLoS ONE,* 12.

LYU, S. & UNTEREKER, D. 2009. Degradability of Polymers for Implantable Biomedical Devices. *International Journal of Molecular Sciences,* 10**,** 4033-4065.

MAIER, A., STEIDL, S., CHRISTLEIN, V. & HORNEGGER, J. 2018. *Medical Imaging Systems*, Springer International Publishing.

MANNES, D., SCHMID, F., FREY, J., SCHMIDT-OTT, K. & LEHMANN, E. 2015. Combined Neutron and X-ray Imaging for Non-invasive Investigations of Cultural Heritage Objects. *Physics Procedia,* 69**,** 653-660.

MARCO, I., MYRISSA, A., MARTINELLI, E., FEYERABEND, F., WILLUMEIT-ROMER, R., WEINBERG, A. M. & VAN DER BIEST, O. 2017. In vivo and in vitro degradation comparison of pure Mg, Mg-10Gd and Mg-2Ag: a short term study. *Eur Cell Mater,* 33**,** 90-104.

MARONE, F. & STAMPANONI, M. 2012. Regridding reconstruction algorithm for real-time tomographic imaging. *J Synchrotron Radiat,* 19**,** 1029-37.

MARTIN, T. & KOCH, A. 2006. Recent developments in X-ray imaging with micrometer spatial resolution. *J Synchrotron Radiat,* 13**,** 180-94.

MAYO, S. & ENDRIZZI, M. 2019. X-Ray Phase Contrast Methods. *In:* IDA, N. & MEYENDORF, N. (eds.) *Handbook of Advanced Nondestructive Evaluation.* Cham: Springer International Publishing.

MCINNES, L., HEALY, J. & ASTELS, S. 2017. hdbscan: Hierarchical density based clustering. *The Journal of Open Source Software,* 2**,** 205.

MOOSMANN, J. 2021. GitHub - moosmann/matlab: data reconstruction and analysis tools for tomography data acquired at the Imaging Beamline (IBL) at P05 and at the High-Energy Material Science (HEMS) beamline at P07 of PETRA III at DESY, both operated by HZG. [online] Accessed: 28-Oct-2021.

MOOSMANN, J., ZELLER-PLUMHOFF, B., WIELAND, D. C. F., GALLI, S., KRÜGER, D., DOSE, T., BURMESTER, H., WILDE, F., BECH, M., PERUZZI, N., WIESE, B., HIPP, A., BECKMANN, F., HAMMEL, J. & WILLUMEIT-RÖMER, R. 2017. *Biodegradable magnesium-based implants in bone studied by synchrotron radiation microtomography*, SPIE.

MÜLLER, M., KIMM, M. A., FERSTL, S., ALLNER, S., ACHTERHOLD, K., HERZEN, J., PFEIFFER, F. & BUSSE, M. 2018. Nucleus-specific X-ray stain for 3D virtual histology. *Scientific Reports,* 8.

MYRISSA, A., BRAEUER, S., MARTINELLI, E., WILLUMEIT-ROMER, R., GOESSLER, W. & WEINBERG, A. M. 2017. Gadolinium accumulation in organs of Sprague-Dawley(R) rats after implantation of a biodegradable magnesium-gadolinium alloy. *Acta Biomater,* 48**,** 521-529.

NORVIK, C., WESTOO, C. K., PERUZZI, N., LOVRIC, G., VAN DER HAVE, O., MOKSO, R., JEREMIASEN, I., BRUNNSTROM, H., GALAMBOS, C., BECH, M. & TRAN-LUNDMARK, K. 2020. Synchrotron-based phase-contrast micro-CT as a tool for understanding pulmonary vascular pathobiology and the 3-D microanatomy of alveolar capillary dysplasia. *Am J Physiol Lung Cell Mol Physiol,* 318**,** L65-L75.

OHLSSON, B., DAHLIN, L. B., ENGLUND, E. & VERESS, B. 2020. Autonomic and peripheral neuropathy with reduced intraepidermal nerve fiber density can be observed in patients with gastrointestinal dysmotility. *Clinical Case Reports,* 8**,** 142-148.

OHLSSON, B., GUSTAFSSON, R., SWAHN, F., TOTH, E., VERESS, B. & THORLACIUS, H. 2018. Endoscopic full-thickness biopsy, a novel method in the work up of complicated abdominal symptoms. *Therapeutic advances in gastroenterology,* 11**,** 1756283X17730747.

OVERDICK, M., BÄUMER, C., ENGEL, K. J., FINK, J., HERRMANN, C., KRÜGER, H., SIMON, M., STEADMAN, R. & ZEITLER, G. 2009. Status of direct conversion detectors for medical imaging with X-rays. *IEEE Transactions on Nuclear Science.*

PAGANIN, D. 2006. *Coherent X-Ray Optics,* Oxford, Oxford University Press.

PAGANIN, D., MAYO, S. C., GUREYEV, T. E., MILLER, P. R. & WILKINS, S. W. 2002. Simultaneous phase and amplitude extraction from a single defocused image of a homogeneous object. *J Microsc,* 206**,** 33-40.

PAULUS, M. J., GLEASON, S. S., KENNEL, S. J., HUNSICKER, P. R. & JOHNSON, D. K. 2000. High resolution X-ray computed tomography: an emerging tool for small animal cancer research. *Neoplasia (New York, N.Y.),* 2**,** 62-70.

PEDREGOSA, F., VAROQUAUX, G., GRAMFORT, A., MICHEL, V., THIRION, B., GRISEL, O., BLONDEL, M., PRETTENHOFER, P., WEISS, R. & DUBOURG, V. 2011. Scikit-learn: Machine learning in Python. *the Journal of machine Learning research,* 12**,** 2825-2830.

PEÑA, F. D. L., PRESTAT, E., FAUSKE, V. T., BURDET, P., LÄHNEMANN, J., FURNIVAL, T., JOKUBAUSKAS, P., NORD, M., OSTASEVICIUS, T., MACARTHUR, K. E., JOHNSTONE, D. N., SARAHAN, M., AARHOLT, T., TAILLON, J., PQUINN, D., MIGUNOV, V., ELJARRAT, A., CARON, J., POON, T., MAZZUCCO, S., FRANCIS, C., MARTINEAU, B., ACTIONS, U., SOMNATH, S., SLATER, T., TAPPY, N., WALLS, M., CAUTAERTS, N., WINKLER, F. & DENSMERIJN 2021. hyperspy/hyperspy: Release v1.6.5.

PEÑA FERNÁNDEZ, M., CIPICCIA, S., DALL'ARA, E., BODEY, A. J., PARWANI, R., PANI, M., BLUNN, G. W., BARBER, A. H. & TOZZI, G. 2018. Effect of SR-microCT radiation on the mechanical integrity of trabecular bone using in situ mechanical testing and digital volume correlation. *Journal of the Mechanical Behavior of Biomedical Materials,* 88**,** 109-119.

PFEIFFER, F. 2018. X-ray ptychography. *Nature Photonics,* 12**,** 9-17.

PFEIFFER, F., HERZEN, J., WILLNER, M., CHABIOR, M., AUWETER, S., REISER, M. & BAMBERG, F. 2013. Grating-based X-ray phase contrast for biomedical imaging applications. *Zeitschrift für Medizinische Physik,* 23**,** 176-185.

PUSHIE, M. J., PICKERING, I. J., KORBAS, M., HACKETT, M. J. & GEORGE, G. N. 2014. Elemental and Chemically Specific X-ray Fluorescence Imaging of Biological Systems. *Chemical Reviews,* 114**,** 8499-8541.

RAJAN, E., GOSTOUT, C. J., WONG KEE SONG, L. M., SZARKA, L. A., KASHYAP, P. C., SMYRK, T. C., BINGENER, J., DETERS, J. L., KNIPSCHIELD, M. A., BERNARD, C. E. & FARRUGIA, G. 2016. Innovative gastric endoscopic muscle biopsy to identify all cell types, including myenteric neurons and interstitial cells of Cajal in patients with idiopathic gastroparesis: a feasibility study (with video). *Gastrointest Endosc,* 84**,** 512-7.

RAMALHO, M., RAMALHO, J., BURKE, L. M. & SEMELKA, R. C. 2017. Gadolinium Retention and Toxicity-An Update. *Adv Chronic Kidney Dis,* 24**,** 138-146.

RAUCH, H. & WASCHKOWSKI, W. 2003. Neutron Scattering Lengths *In:* DIANOUX, A.-J. & LANDER, G. (eds.) *ILL Neutron Data Booklet (second edition).* Philadelphia, PA: Old City Publishing.

RICHETTE, P., AYOUB, G., LAHALLE, S., VICAUT, E., BADRAN, A.-M., JOLY, F., MESSING, B. & BARDIN, T. 2007. Hypomagnesemia associated with chondrocalcinosis: A cross-sectional study. *Arthritis & Rheumatism,* 57**,** 1496-1501.

ROBERTS, B. C., PERILLI, E. & REYNOLDS, K. J. 2014. Application of the digital volume correlation technique for the measurement of displacement and strain fields in bone: A literature review. *Journal of Biomechanics,* 47**,** 923-934.

RÖNTGEN, W. C. 1895. Ueber eine neue Art von Strahlen. *Sitzungsberichten der Würzburger Physik.-medic. Gesellschaft***,** 132-141.

RÖNTGEN, W. C. 1896. On a New Kind of Rays. *Science,* 3**,** 227-31.

ROUBIN, E., ANDÒ, E. & ROUX, S. 2019. The colours of concrete as seen by X-rays and neutrons. *Cement and Concrete Composites,* 104**,** 103336.

RUDE, R. K. 1998. Magnesium Deficiency: A Cause of Heterogenous Disease in Humans. *Journal of Bone and Mineral Research,* 13**,** 749-758.

SALDITT, T., ASPELMEIER, T. & AEFFNER, S. 2017. Biomedical Imaging: Principles of Radiography, Tomography and Medical Physics.

SALDITT, T., OSTERHOFF, M., KRENKEL, M., WILKE, R. N., PRIEBE, M., BARTELS, M., KALBFLEISCH, S. & SPRUNG, M. 2015. Compound focusing mirror and X-ray waveguide optics for coherent imaging and nano-diffraction. *J Synchrotron Radiat,* 22**,** 867-78.

SALDITT, T. & TÖPPERWIEN, M. 2020. Holographic Imaging and Tomography of Biological Cells and Tissues. *In:* SALDITT, T., EGNER, A. & LUKE, D. R. (eds.) *Nanoscale Photonic Imaging.* Cham: Springer International Publishing.

SANCHEZ, A. H. M., LUTHRINGER, B. J. C., FEYERABEND, F. & WILLUMEIT, R. 2015. Mg and Mg alloys: How comparable are in vitro and in vivo corrosion rates? A review. *Acta Biomaterialia,* 13**,** 16-31.

SANYAL, S., MARCKMANN, P., SCHERER, S. & ABRAHAM, J. L. 2011. Multiorgan gadolinium (Gd) deposition and fibrosis in a patient with nephrogenic systemic fibrosis--an autopsy-based review. *Nephrol Dial Transplant,* 26**,** 3616-26.

SCHINDELIN, J., ARGANDA-CARRERAS, I., FRISE, E., KAYNIG, V., LONGAIR, M., PIETZSCH, T., PREIBISCH, S., RUEDEN, C., SAALFELD, S., SCHMID, B., TINEVEZ, J. Y., WHITE, D. J., HARTENSTEIN, V., ELICEIRI, K., TOMANCAK, P. & CARDONA, A. 2012. Fiji: an open-source platform for biological-image analysis. *Nat Methods,* 9**,** 676-82.

SCHNEIDER, C. A., RASBAND, W. S. & ELICEIRI, K. W. 2012. NIH Image to ImageJ: 25 years of image analysis. *Nat Methods,* 9**,** 671-5.

SCHULZ, G., WEITKAMP, T., ZANETTE, I., PFEIFFER, F., BECKMANN, F., DAVID, C., RUTISHAUSER, S., REZNIKOVA, E. & MÜLLER, B. 2010. High-resolution tomographic imaging of a human cerebellum: comparison of absorption and grating-based phase contrast. *Journal of The Royal Society Interface,* 7**,** 1665-1676.

SCHWARZ, F., DERKS, J., MONJE, A. & WANG, H. L. 2018. Peri-implantitis. *J Periodontol,* 89 Suppl 1**,** S267-s290.

SCIMECA, M., BISCHETTI, S., LAMSIRA, H. K., BONFIGLIO, R. & BONANNO, E. 2018. Energy Dispersive X-ray (EDX) microanalysis: A powerful tool in biomedical research and diagnosis. *European Journal of Histochemistry,* 62.

SEARS, V. F. 2006. Scattering lengths for neutrons. *In:* PRINCE, E. (ed.) *International Tables for Crystallography.* Kluwer Academic Publishers.

SOJKA, J. E. & WEAVER, C. M. 1995. Magnesium supplementation and osteoporosis. *Nutr Rev,* 53**,** 71-4.

SOLÉ, V. A., PAPILLON, E., COTTE, M., WALTER, P. & SUSINI, J. 2007. A multiplatform code for the analysis of energy-dispersive X-ray fluorescence spectra. *Spectrochimica Acta Part B: Atomic Spectroscopy,* 62**,** 63-68.

SPERBER, A. D., BANGDIWALA, S. I., DROSSMAN, D. A., GHOSHAL, U. C., SIMREN, M., TACK, J., WHITEHEAD, W. E., DUMITRASCU, D. L., FANG, X., FUKUDO, S., KELLOW, J., OKEKE, E., QUIGLEY, E. M. M., SCHMULSON, M., WHORWELL, P., ARCHAMPONG, T., ADIBI, P., ANDRESEN, V., BENNINGA, M. A., BONAZ, B., BOR, S., FERNANDEZ, L. B., CHOI, S. C., CORAZZIARI, E. S., FRANCISCONI, C., HANI, A., LAZEBNIK, L., LEE, Y. Y., MULAK, A., RAHMAN, M. M., SANTOS, J., SETSHEDI, M., SYAM, A. F., VANNER, S., WONG, R. K., LOPEZ-COLOMBO, A., COSTA, V., DICKMAN, R., KANAZAWA, M., KESHTELI, A. H., KHATUN, R., MALEKI, I., POITRAS, P., PRATAP, N., STEFANYUK, O., THOMSON, S., ZEEVENHOOVEN, J. & PALSSON, O. S. 2021. Worldwide Prevalence and Burden of Functional Gastrointestinal Disorders, Results of Rome Foundation Global Study. *Gastroenterology,* 160**,** 99-114.e3.

STAMATI, O., ANDÒ, E., ROUBIN, E., CAILLETAUD, R., WIEBICKE, M., PINZON, G., COUTURE, C., HURLEY, R., CAULK, R., CAILLERIE, D., MATSUSHIMA, T., BÉSUELLE, P., BERTONI, F., ARNAUD, T., LABORIN, A., RORATO, R., SUN, Y., TENGATTINI, A., OKUBADEJO, O., COLLIAT, J.-B., SAADATFAR, M., GARCIA, F., PAPAZOGLOU, C., VEGO, I., BRISARD, S., DIJKSTRA, J. & BIRMPILIS, G. 2020. spam: Software for Practical Analysis of Materials. *Journal of Open Source Software,* 5**,** 2286.

STAMPANONI, M., WANG, Z., THÜRING, T., DAVID, C., ROESSL, E., TRIPPEL, M., KUBIK-HUCH, R. A., SINGER, G., HOHL, M. K. & HAUSER, N. 2011. The first analysis and clinical evaluation of native breast tissue using differential phase-contrast mammography. *Investigative radiology,* 46**,** 801-806.

STAVROPOULOU, E., ANDÒ, E., ROUBIN, E., LENOIR, N., TENGATTINI, A., BRIFFAUT, M. & BÉSUELLE, P. 2020. Dynamics of Water Absorption in Callovo-Oxfordian Claystone Revealed With Multimodal X-Ray and Neutron Tomography. *Frontiers in Earth Science,* 8.

SUMNER, D. R. 2015. Long-term implant fixation and stress-shielding in total hip replacement. *Journal of Biomechanics,* 48**,** 797-800.

SUNDFELDT, M., V CARLSSON, L., B JOHANSSON, C., THOMSEN, P. & GRETZER, C. 2006. Aseptic loosening, not only a question of wear: A review of different theories. *Acta Orthopaedica,* 77**,** 177-197.

TENGATTINI, A., LENOIR, N., ANDÒ, E., GIROUD, B., ATKINS, D., BEAUCOUR, J. & VIGGIANI, G. 2020. NeXT-Grenoble, the Neutron and X-ray tomograph in Grenoble. *Nuclear Instruments and Methods in Physics Research Section A: Accelerators, Spectrometers, Detectors and Associated Equipment,* 968**,** 163939.

THOMLINSON, W., SUORTTI, P. & CHAPMAN, D. 2005. Recent advances in synchrotron radiation medical research. *Nuclear Instruments and Methods in Physics Research Section A: Accelerators, Spectrometers, Detectors and Associated Equipment,* 543**,** 288-296.

THOMSEN, N. O., ENGLUND, E., THRAINSDOTTIR, S., ROSÉN, I. & DAHLIN, L. B. 2009. Intraepidermal nerve fibre density at wrist level in diabetic and non-diabetic patients. *Diabet Med,* 26**,** 1120-6.

TOMA, H., NAKAMURA, K., KURAOKA, A., TANAKA, M. & KAWABUCHI, M. 1999. Three-dimensional structures of c-Kit-positive cellular networks in the guinea pig small intestine and colon. *Cell Tissue Res,* 295**,** 425-36.

TÖPPERWIEN, M., VAN DER MEER, F., STADELMANN, C. & SALDITT, T. 2018. Three-dimensional virtual histology of human cerebellum by X-ray phase-contrast tomography. *Proc Natl Acad Sci U S A,* 115**,** 6940-6945.

TÖRNQUIST, E., LE CANN, S., TUDISCO, E., TENGATTINI, A., ANDÒ, E., LENOIR, N., HEKTOR, J., RAINA, D. B., TÄGIL, M., HALL, S. A. & ISAKSSON, H. 2021. Dual modality neutron and x-ray tomography for enhanced image analysis of the bone-metal interface. *Physics in Medicine & Biology,* 66**,** 135016.

TÖTZKE, C., KARDJILOV, N., HILGER, A., RUDOLPH-MOHR, N., MANKE, I. & OSWALD, S. E. 2021. Three-dimensional in vivo analysis of water uptake and translocation in maize roots by fast neutron tomography. *Scientific Reports,* 11.

TUDISCO, E., ANDÒ, E., CAILLETAUD, R. & HALL, S. A. 2017. TomoWarp2: A local digital volume correlation code. *SoftwareX,* 6**,** 267-270.

TUOHIMAA, T., OTENDAL, M. & HERTZ, H. M. 2007. Phase-contrast x-ray imaging with a liquid-metal-jet-anode microfocus source. *Applied Physics Letters,* 91**,** 074104.

TURYANSKAYA, A., RAUWOLF, M., GRUNEWALD, T. A., MEISCHEL, M., STANZL-TSCHEGG, S., LOFFLER, J. F., WOBRAUSCHEK, P., WEINBERG, A. M., LICHTENEGGER, H. C. & STRELI, C. 2016. microXRF Elemental Mapping of Bioresorbable Magnesium-Based Implants in Bone. *Materials (Basel),* 9.

URUGA, T. 2017. Synchrotron-Radiation Sources, X-ray Optics and Beamlines. *In:* IWASAWA, Y., ASAKURA, K. & TADA, M. (eds.) *XAFS Techniques for Catalysts, Nanomaterials, and Surfaces.* Cham: Springer International Publishing.

VAN AARLE, W., PALENSTIJN, W. J., CANT, J., JANSSENS, E., BLEICHRODT, F., DABRAVOLSKI, A., DE BEENHOUWER, J., JOOST BATENBURG, K. & SIJBERS, J. 2016. Fast and flexible X-ray tomography using the ASTRA toolbox. *Opt Express,* 24**,** 25129-25147.

VAN AARLE, W., PALENSTIJN, W. J., DE BEENHOUWER, J., ALTANTZIS, T., BALS, S., BATENBURG, K. J. & SIJBERS, J. 2015. The ASTRA Toolbox: A platform for advanced algorithm development in electron tomography. *Ultramicroscopy,* 157**,** 35-47.

VAN DER WALT, S., SCHONBERGER, J. L., NUNEZ-IGLESIAS, J., BOULOGNE, F., WARNER, J. D., YAGER, N., GOUILLART, E., YU, T. & SCIKIT-IMAGE, C. 2014. scikit-image: image processing in Python. *PeerJ,* 2**,** e453.

VANDERWINDEN, J. M., RUMESSEN, J. J., DE LAET, M. H., VANDERHAEGHEN, J. J. & SCHIFFMANN, S. N. 2000. CD34 immunoreactivity and interstitial cells of Cajal in the human and mouse gastrointestinal tract. *Cell Tissue Res,* 302**,** 145-53.

VANDEWEGHE, S., COELHO, P. G., VANHOVE, C., WENNERBERG, A. & JIMBO, R. 2013. Utilizing micro-computed tomography to evaluate bone structure surrounding dental implants: A comparison with histomorphometry. *Journal of Biomedical Materials Research Part B: Applied Biomaterials,* 101**,** 1259-1266.

VASCONCELOS, D. M., SANTOS, S. G., LAMGHARI, M. & BARBOSA, M. A. 2016. The two faces of metal ions: From implants rejection to tissue repair/regeneration. *Biomaterials,* 84**,** 262-275.

VERESS, B. & OHLSSON, B. 2020. Spatial relationship between telocytes, interstitial cells of Cajal and the enteric nervous system in the human ileum and colon. *J Cell Mol Med.*

VIRTANEN, S. 2011. Biodegradable Mg and Mg alloys: Corrosion and biocompatibility. *Materials Science and Engineering: B,* 176**,** 1600-1608.

WALTHER, C., JEREMIASEN, M., RISSLER, P., JOHANSSON, J. L., LARSSON, M. S. & WALTHER, B. S. 2016. A New Method for Endoscopic Sampling of Submucosal Tissue in the Gastrointestinal Tract: A Comparison of the Biopsy Forceps and a New Drill Instrument. *Surg Innov,* 23**,** 572-580.

WANG, N. & GIBBONS, C. H. 2013. Chapter 30 - Skin biopsies in the assessment of the autonomic nervous system. *In:* BUIJS, R. M. & SWAAB, D. F. (eds.) *Handbook of Clinical Neurology.* Elsevier.

WEBB, S. 1990. *From the watching of shadows: the origins of radiological tomography*, CRC Press.

WEBB, S. A brief history of tomography and CT. PROCEEDINGS 7th ASIAN & OCEANIAN CONGRESS OF RADIOLOGY, 1995. 429-431.

WEINMANN, H., BRASCH, R., PRESS, W. & WESBEY, G. 1984. Characteristics of gadolinium-DTPA complex: a potential NMR contrast agent. *American Journal of Roentgenology,* 142**,** 619-624.

WEITKAMP, T. 2004. *XWFP: an x-ray wavefront propagation software package for the IDL computer language*, SPIE.

WENG, W., BIESIEKIERSKI, A., LI, Y., DARGUSCH, M. & WEN, C. 2021. A review of the physiological impact of rare earth elements and their uses in biomedical Mg alloys. *Acta Biomater*.

WESTOO, C., NORVIK, C., PERUZZI, N., VAN DER HAVE, O., LOVRIC, G., JEREMIASEN, I., TRAN, P. K., MOKSO, R., DE JESUS PEREZ, V., BRUNNSTROM, H., BECH, M., GALAMBOS, C. & TRAN-LUNDMARK, K. 2021. Distinct types of plexiform lesions identified by synchrotron-based phase-contrast micro-CT. *Am J Physiol Lung Cell Mol Physiol,* 321**,** L17-L28.

WILDE, F., OGURRECK, M., GREVING, I., HAMMEL, J. U., BECKMANN, F., HIPP, A., LOTTERMOSER, L., KHOKHRIAKOV, I., LYTAEV, P., DOSE, T., BURMESTER, H., MÜLLER, M. & SCHREYER, A. Micro-CT at the imaging beamline P05 at PETRA III. AIP conference Proceedings, 2016 2016. AIP Publishing LLC, 030-035.

WILKINS, S. W., NESTERETS, Y. I., GUREYEV, T. E., MAYO, S. C., POGANY, A. & STEVENSON, A. W. 2014. On the evolution and relative merits of hard X-ray phase-contrast imaging methods. *Philosophical Transactions of the Royal Society A: Mathematical, Physical and Engineering Sciences,* 372**,** 20130021.

WILLIAMS, D. 2012. 1 - Concepts in biocompatibility: new biomaterials, new paradigms and new testing regimes. *In:* BOUTRAND, J.-P. (ed.) *Biocompatibility and Performance of Medical Devices.* Woodhead Publishing.

WILLMOTT, P. 2011. An introduction to synchrotron radiation: Techniques and applications. *An Introduction to Synchrotron Radiation: Techniques and Applications***,** 1-352.

WITTE, F. 2015. Reprint of: The history of biodegradable magnesium implants: A review. *Acta Biomaterialia,* 23**,** S28-S40.

WITTE, F., FISCHER, J., NELLESEN, J. & BECKMANN, F. 2006. *Microtomography of magnesium implants in bone and their degradation*, SPIE.

WORACEK, R., SANTISTEBAN, J., FEDRIGO, A. & STROBL, M. 2018. Diffraction in neutron imaging—A review. *Nuclear Instruments and Methods in Physics Research Section A: Accelerators, Spectrometers, Detectors and Associated Equipment,* 878**,** 141-158.

YUSHKEVICH, P. A., PIVEN, J., HAZLETT, H. C., SMITH, R. G., HO, S., GEE, J. C. & GERIG, G. 2006. User-guided 3D active contour segmentation of anatomical structures: significantly improved efficiency and reliability. *Neuroimage,* 31**,** 1116-28.

ZANETTE, I., ZHOU, T., BURVALL, A., LUNDSTRÖM, U., LARSSON, D. H., ZDORA, M., THIBAULT, P., PFEIFFER, F. & HERTZ, H. M. 2014. Speckle-Based X-Ray Phase-Contrast and Dark-Field Imaging with a Laboratory Source. *Physical Review Letters,* 112**,** 253903.

ZELLER-PLUMHOFF, B., GILE, M., PRIEBE, M., SLOMINSKA, H., BOLL, B., WIESE, B., WÜRGER, T., WILLUMEIT-RÖMER, R. & MEIßNER, R. H. 2021a. Exploring key ionic interactions for magnesium degradation in simulated body fluid – A data-driven approach. *Corrosion Science,* 182.

ZELLER-PLUMHOFF, B., HELMHOLZ, H., FEYERABEND, F., DOSE, T., WILDE, F., HIPP, A., BECKMANN, F., WILLUMEIT-RÖMER, R. & HAMMEL, J. U. 2018. Quantitative characterization of degradation processes in situ by means of a bioreactor coupled flow chamber under physiological conditions using time-lapse SRµCT. *Materials and Corrosion,* 69**,** 298-306.

ZELLER-PLUMHOFF, B., MALICH, C., KRUGER, D., CAMPBELL, G., WIESE, B., GALLI, S., WENNERBERG, A., WILLUMEIT-ROMER, R. & WIELAND, D. C. F. 2020. Analysis of the bone ultrastructure around biodegradable Mg-xGd implants using small angle X-ray scattering and X-ray diffraction. *Acta Biomater,* 101**,** 637-645.

ZELLER-PLUMHOFF, B., TOLNAI, D., WOLFF, M., GREVING, I., HORT, N. & WILLUMEIT-RÖMER, R. 2021b. Utilizing Synchrotron Radiation for the Characterization of Biodegradable Magnesium Alloys—From Alloy Development to the Application as Implant Material. *Advanced Engineering Materials***,** 2100197.

ZHANG, L.-N., HOU, Z.-T., YE, X., XU, Z.-B., BAI, X.-L. & SHANG, P. 2013. The effect of selected alloying element additions on properties of Mg-based alloy as bioimplants: A literature review. *Frontiers of Materials Science,* 7**,** 227-236.

ZHAO, Y., BRUN, E., COAN, P., HUANG, Z., SZTROKAY, A., DIEMOZ, P. C., LIEBHARDT, S., MITTONE, A., GASILOV, S., MIAO, J. & BRAVIN, A. 2012. High-resolution, low-dose phase contrast X-ray tomography for 3D diagnosis of human breast cancers. *Proceedings of the National Academy of Sciences,* 109**,** 18290-18294.

ZIESCHE, R. F., ROBINSON, J. B., MARKÖTTER, H., BRADBURY, R., TENGATTINI, A., LENOIR, N., HELFEN, L., KOCKELMANN, W., KARDJILOV, N., MANKE, I., BRETT, D. J. L. & SHEARING, P. R. 2020. Editors' Choice—4D Neutron and X-ray Tomography Studies of High Energy Density Primary Batteries: Part II. Multi-Modal Microscopy of LiSOCl2 Cells. *Journal of The Electrochemical Society,* 167**,** 140509.